PRE-CHAMBER IGNITION SYSTEM DEVELOPMENT FOR LEAN-BURN GASOLINE DIRECT INJECTION ENGINE

MUHAMMED FAYAZ PALAKUNNUMMAL

A thesis submitted in partial fulfillment of the requirements of London South Bank University for the degree of Doctor of Philosophy

June 2020
School of Engineering
London South Bank University

Acknowledgements

First and foremost, I acknowledge the confidence shown by Dr Mark Ellis to take me as his PhD student. This dissertation would not have been possible without his guidance, help and encouragement. I would like to thank Dr Mark also for giving the opportunity to work part-time with Advanced Engine Research Ltd and contribute to a few exciting motor-sport engine projects. I acknowledge equally the help and guidance Prof Marouan Nazha has provided during the research project.

This research programme was sponsored by and carried out in collaboration with Advanced Engine Research Ltd. I would like to express my sincere gratitude to all members of Advanced Engine Research for the wonderful support and enriching experience AER provided all throughout. I would like to acknowledge the contributions of Declan Ward, Cesare Parolini, Shane Veenendal, Will Pedley, Nick Treen, Aaron South, Keith Lane, Sonny Dawson and Nick Jordan from AER to this project. Thanks a lot to my colleague Priyadarshi Sahu, for being a friend and for his valuable contributions to this thesis. Thanks to my amazing office mates Dr Ertan Maqbool Siddiqui, Dr Tara Singh Ghatauray and Dr Zoe De Grussa for being good friends.

I am very much indebted to my parents who were an everlasting source of encouragement and support all throughout. My utmost gratitude to my brother Dr Muhammed Fasil for being a mentor and for the supports during my stay in the United Kingdom. Last but not the least, my wife Jaseela, without whom this thesis would not have materialized.

Abstract

Recent regulation changes to restricted fuel usage in motor-sport events resulted in motor-sport engine manufacturers focusing on improving thermal efficiency and often claim thermal efficiency figures well above equivalent road car engines. With limited fuel usage, motor-sport engines are operated with a lean mixture to benefit from higher cycle efficiency, requiring an ignition system that is suitable for the lean mixture. Pre-chamber ignition is identified as a promising method to improve lean limit and has the potential to reduce end gas auto-ignition.

A pre-chamber ignition system is developed for a lean-burn gasoline direct injection engine with the objective of reducing BSFC. Initial part of the project focused on developing a multi-dimensional engine model, representing single cylinder version of a lean-burn turbo-charged Gasoline Direct Injection engine, achieving correlation to the available test data. The same CFD model is later updated to include a pre-chamber and studied the influence of various design features on the performance of pre-chamber ignited combustion. Pre-chamber fuel enrichment was observed to be influential in achieving combustion stability and was key factor in deciding final pre-chamber design along with burn duration. Two pre-chamber designs proposed for the testing based on this study, both produced compromised results for combustion duration and pre-chamber equivalence ratio.

For experimental validation of the pre-chamber design, a single cylinder engine was developed along with a two-stage supercharger rig. Engine performance with base spark ignition and two pre-chamber designs were compared and one pre-chamber design was proposed for final implementation. Heat transfer from the pre-chamber observed to be a critical factor in avoiding pre-ignition and achieving performance. Also, conventional transducer based knock detection strategy found not working with pre-chamber combustion and a novel knock detection strategy based on cylinder pressure trace is proposed for pre-chamber based combustion.

This research work delivered a pre-chamber design for higher BMEP (>25 Bar) gasoline engines and identified a novel knock detection strategy for pre-chamber ignited combustion.

Contents

List of Figures

List of Tables

Abbreviations and Symbols

Abbreviations

Abbreviations	Description
3D	Three-dimensional
AFR	Air fuel ratio
AMR	Adaptive Mesh Refinement
BEV	Battery electric vehicle.
BSFC	Brake specific fuel consumption.
CA	Crank angle in degrees.
CAD	Computer aided design.
CCV	Cycle to cycle variations.
CFD	Computational fluid dynamics.
CR	Compression ratio.
DKI	Dimensionless knock indicator.
FCEV	Fuel cell electric vehicle.
GDI	Gasoline direct injection.
HCCI	homogenous charge compression ignition.
HTC	Heat transfer coefficient.
IMEP	Indicated mean effective pressure.
IMEPg	Gross indicated mean effective pressure.
IMPO	Integral of modulus of pressure oscillations.
KLSA	Knock limited spark advance.
LKI	Logarithmic knock index.
MAPO	Maximum amplitude of pressure oscillations.
MFB	Mass fraction burned.
MBT	Minimum advance for best torque.
ONR	Octane number.
PC	Pre chamber.
PFI	Port fuel injection.
PHEV	Plug-in hybrid electric vehicle.
LES	Large eddy simulation.
RANS	Reynolds averaged Navier Stokes.

RPM	Revolutions per minute.
SCRE	Single cylinder research engine.
SI	Spark ignition.
WOT	Wide open throttle.

Symbols

Symbol	Units	Description
λ		Relative air fuel ratio
P_{Cyl}	Bar	In-cylinder pressure
P_{hp}	Bar	High pass filtered cylinder pressure
CuBe		Copper Beryllium

Chapter 1

Introduction

Contents

1.1 Context and motivation

Internal combustion engines are still by far the most used prime movers for the automotive applications. In 2017, Green House Gas (GHG) emissions from road transport made up around a fifth of the UK's total GHG emissions and has been experiencing a steady rise over past three decades [1]. Though emissions of many pollutants that are particularly damaging to health (carbon monoxide, particulate matter and nitrogen oxides) have reduced substantially during the same time, the UK government has announced a 'Road to Zero CO_2' strategy: a long term plan that will ultimately end the sale of new conventional petrol and Diesel cars and vans by 2040 [2]. In a recently released report [2], Institution of Mechanical Engineers (IMechE) argue that this zero emission target is only considering emissions at the point of use or tank to wheel (TTW) and a life cycle analysis of a passenger vehicle gives a different picture as shown in Fig. 1.1. With 100% renewable fuels, the carbon footprint of an internal combustion engine powered vehicle is even less than an electric counterpart which takes electricity from 100% renewable source and IMechE proposes that research on improving internal combustion engine technology and low-carbon fuel development must continue. The same report also forecasts that internal combustion engine is likely to be in use in significant share at least till 2040 and relying only on electric vehicles is not sufficient to make any meaningful impact in reducing GHG emissions. In a different study by US Energy Information Administration [3], the sales projections for light duty vehicles in the US market shows that gasoline vehicles will hold the major market share until 2050 (Fig. 1.2). So improving efficiency of IC engines is also crucial in bringing down total emissions.

		Production	Fuel Provision (WTT)	Use (TTW)	Baseline (current)	Total
GASOLINE	Conventional	26	19	87		171
	e-Gasoline with 100% renewables*	26	19			
DIESEL	Conventional	29	9	75		140
	e-Diesel with 100% renewables*	29	17			
NATURAL GAS	Conventional	29	18	66		149
	e-Gas with 100% renewables*	29	19			
PHEV	EU mix	41	33	20		136
	Green electricity & PtX 100% renewables*	41	5			
BEV	EU mix	57	37			117
	Green electricity*	57	1			
FCEV	Steam reforming	47	82			159
	e-Hydrogen with 100% renewables*	41	5			

*Carbon footprint for production will also be reduced

CO_2(g/km$_e$)

Figure 1.1: Life-cycle analysis of typical C-segment passenger vehicle in 2030 (sum of coloured bars) compared to current (grey bars) for different conventional and renewable fuels by life-cycle phase [2].

During the last decade, downsized spark ignition engines running under high loads have become more and more attractive for automotive manufacturers. A downsized engine benefits from reduced friction and heat transfer losses due to lesser number of moving components and reduced surface area compared to a larger capacity engine with more number of cylinders. Another key factor in achieving higher efficiency is down-speeding or run the engine at a lower engine speed to benefit from reduced frictional losses at lower engine speeds. One of the competent engine architecture currently being used is the turbocharged Gasoline Direct Injection (GDI). Turbo-charging allows engine to breathe more air at a lower engine speed, avoiding the need for running at higher speeds to produce the target torque. The fuel vaporisation inside the cylinder lowers the mixture temperature and hence, GDI engines can operate at high load with reduced auto-ignition. A GDI engine can also operate at overall lean mode through fuel stratification with a better control in mixture formation. Lean combustion benefits in higher cycle efficiency and also results in lower heat transfer losses with reduced peak combustion temperature. These advantages resulted in increased efficiency leading to the reduction of CO_2 emissions. Though GDI improved thermal efficiency and CO_2 levels, with upcoming stringent emission rules for IC engine powered vehicles, there require increased efforts in improving a spark ignition engine design to achieve higher efficiency and reduced emissions targets.
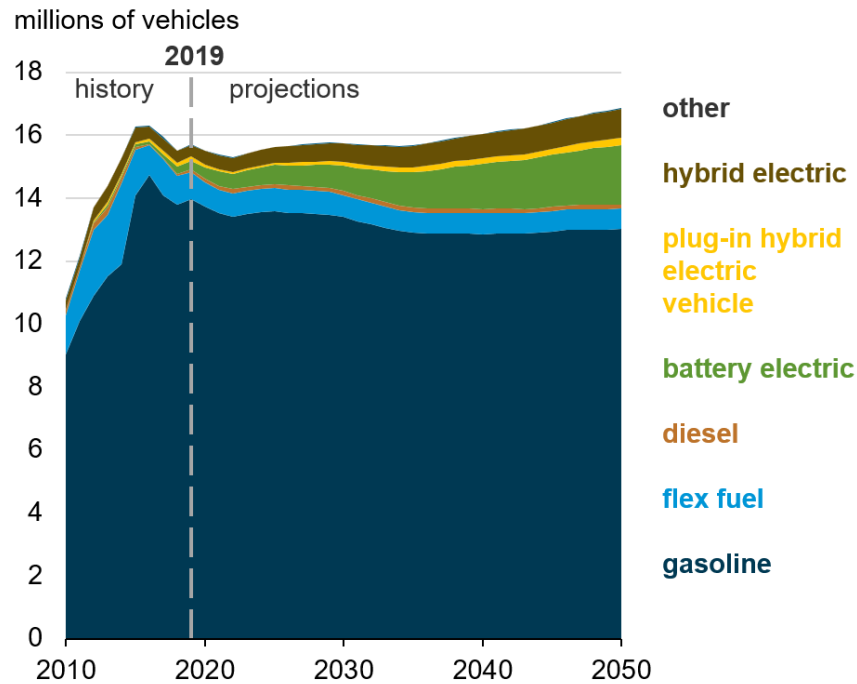
Figure 1.2: Light-duty vehicle sales forecast for the US market by fuel type [3].

Motor-sport engines can show a direction for how gasoline engines can be designed for achieving higher thermal efficiency. To make motor-sports road relevant and to attract automotive manufactures, motor-sports regulatory authorities including International Auto-mobile Federation (FIA) started focusing on fuel efficiency since last decade. This was done by restricting the maximum fuel flow rate to the engine and also by limiting total fuel quantity for a race or per stint for longer running endurance races [4]. Such a restriction has resulted in motor-sport engine manufacturers focusing on reducing the brake specific fuel consumption (BSFC). As per Formula One engine regulations, cylinder geometry including the compression ratio is defined and restricted [4]. One development which has been implemented is to increase the dilution. Higher dilution can deteriorate combustion performance and often require novel ignition systems like pre-chamber ignition. The 1.6 Litre V6 Formula One engine introduced in 2014 is permitted to use a maximum fuel flow rate of 100 kg-hr. Formula One engine manufactures often claim thermal efficiency figures well above an equivalent road car engine. Though major efforts went into developing these highly efficient engines, research findings are not available in the public domain or published literature. Motor-sport engines operate mostly at full load and in a narrow engine speed range, where it is possible to design an engine for higher efficiency compared to a wider load and speed range automotive engine. Such an engine with a narrow operating range can also find its use in hybrid vehicles where electric assist allows the engine to operate only at efficient operating points. A research project on motor-sports engine thus can bring out useful information that can carry forward to road car engines.

1.2   Thesis structure

The thesis is organised as follows:

Chapter 2 explains thermodynamic principles and combustion process in a gasoline engine and basic approaches to improve thermal efficiency. This chapter also discusses significance of burning lean mixture and performance limiting factors for lean mixture burning.

Chapter 3 is a review of pre-chamber ignition system reported in previous research works, listing the merits and drawbacks of pre-chamber ignition system so as to improve upon them in the proposed work. This chapter also set the research objectives, based on identified gap in the research on pre-chamber combustion.

Chapter 4 details the multi-dimensional engine model developed for studying cylinder flow, spray and combustion for a GDI engine.

Chapter 5 discusses the development of pre-chamber design with the help of multi-dimensional engine model. This chapter also details significance of various pre-chamber design parameters on combustion performance and stability.

Chapter 6 describes the engine test facility including single cylinder research engine and boost rig used to evaluate the performance of a fuel flow limited motorsport engine.

Chapter 7 discusses results of performance comparison of base spark ignition system and pre-chamber ignition system including combustion analysis.

Chapter 8 details the difficulty of using a conventional knock detection system with pre-chamber ignition and development of a cylinder pressure based knock detection strategy.

Chapter 9 summarises main conclusions of the present work and directions for further development.

Chapter 2

Combustion in SI Engines

Contents

2.1   Introduction

This chapter describes the thermodynamic principles and turbulent combustion in a gasoline engine and also discusses the main factors that limit the performance of a gasoline engine. An ideal constant volume combustion cycle is shown on the left of Fig. 2.1 and has the following processes:

- 1-2 Reversible adiabatic compression of air-fuel mixture.

- 2-3 Constant volume combustion.

- 3-4 Reversible adiabatic expansion of the burned gases.

- 4-1 Ideal adiabatic exhaust blow-down.

- 1-0 Ideal displacement of burned gases.

- 0-1 Ideal intake process of fresh air-fuel mixture.

The same processes on a real air-fuel cycle, based on a four-stroke gasoline engine works and is shown on the right of Fig. 2.1. The corresponding processes are substantially different from the ideal cycle. An ideal cycle assumes constant volume combustion. On the contrary, an SI engine has a definite burn duration and is usually observed between 30 to 90 crank angle degrees [5]. It is evident that shorter
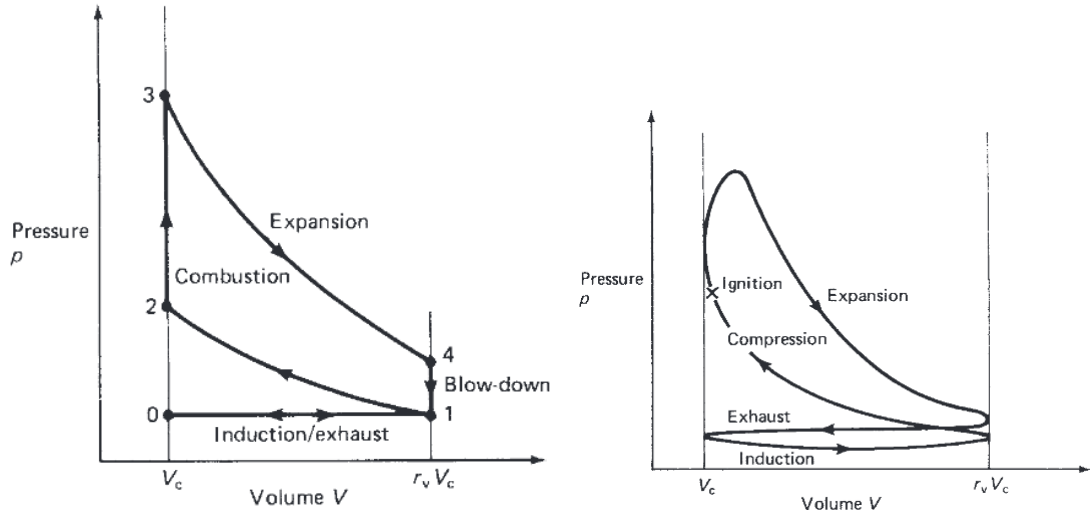
Figure 2.1: Ideal indicator diagram (left) and real indicator diagram for four-stroke engine (right) [7].

burn duration helps in bringing peak pressure point close towards the TDC, also resulting in higher pressure magnitudes and net work transfer to the piston. In real engines, reduced burn duration and resultant higher peak pressure has a diminishing effect on thermal efficiency as instantaneous combustion can raise the temperature, which in turn increases losses from heat transfer and dissociation [8].

The reaction of a hydrocarbon fuel and air is represented by a general equation 2.1. Even if stoichiometric mixture is used, CO, H_2, O_2 and NO_x are present in combustion products due to dissociation. Also, even for lean burn and stoichiometric combustion, unburned hydrocarbons could be present in the combustion products due to various factors including slow combustion with lean mixture and the difficulty of burning charge present in the crevice area.

$$C_xH_y+\frac{a}{\phi}(O_2+\frac{79}{21}N_2) \rightarrow b\ CO_2+c\ H_2O+d\ N_2+e\ O_2+f\ CO+g\ H_2+h\ NO_x+i\ C_xH_y$$

(2.1)
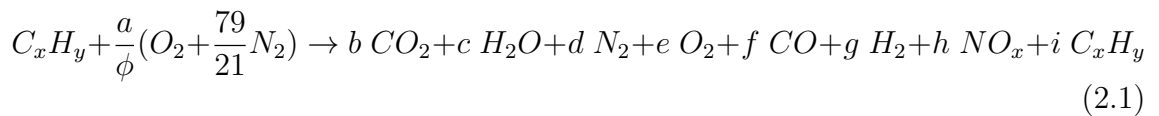
In spark ignition engines, air and fuel is pre-mixed either inside the cylinder or before entering the cylinder. The pre-mixed charge is compressed and a flame is initiated at the tip of the spark plug by an electric discharge. A flame is the result of a self-sustaining chemical reaction occurring within a region of space called the flame front where the unburned mixture is heated and converted into products [5]. Flame is initiated as a spherical kernel at the spark plug tip and propagates into unburned gas. The very early period after the spark is observed to be repeatable, especially for easily ignitable mixture and does not depend on spark gap, mixture composition, ambient turbulence and bulk flow. Subsequent to early flame development, flame kernel may be convected differently in different cycles by the bulk motion of the gas around the spark plug and could cause cyclic combustion variations [6].

Laminar burning velocity is defined as the velocity, relative to and normal to the flame front, with which unburned gas moves into the front and is transformed to products under laminar flow conditions [5]. Laminar flame speed is a property of mixture composition and that depends on fuel, air and presence of burned gas in the mixture. Laminar flame speed is in the order of 1 m/s [7]. With this laminar flame speed and for an engine with bore diameter 90 mm and at 6000 rpm engine speed, a simple calculation for the time required for the flame to reach radial end of the combustion chamber wall from a centrally mounted spark plug, results in around 270º CA, and hence is not realistic to function the engine only with laminar flame speed. For real engines, the combustion process takes place in a turbulent flow field and turbulent flame speed is higher by at least an order of magnitude compared to laminar flame speed [7]. This flow field is produced by high shear flows set up during the intake stroke and modified during the compression stroke. Increased turbulence increases the flame front area through flame wrinkling and accelerates the propagation of the laminar flame. The early burn period starts with laminar combustion and then changes to fully turbulent combustion as the flame size become comparable to the smallest turbulent scales (Kolmogorov scales). The process of turbulent interaction leads to irregular distribution of the burned and unburned gases which are separated by reaction sheet as shown in the Fig. 2.2. With increased
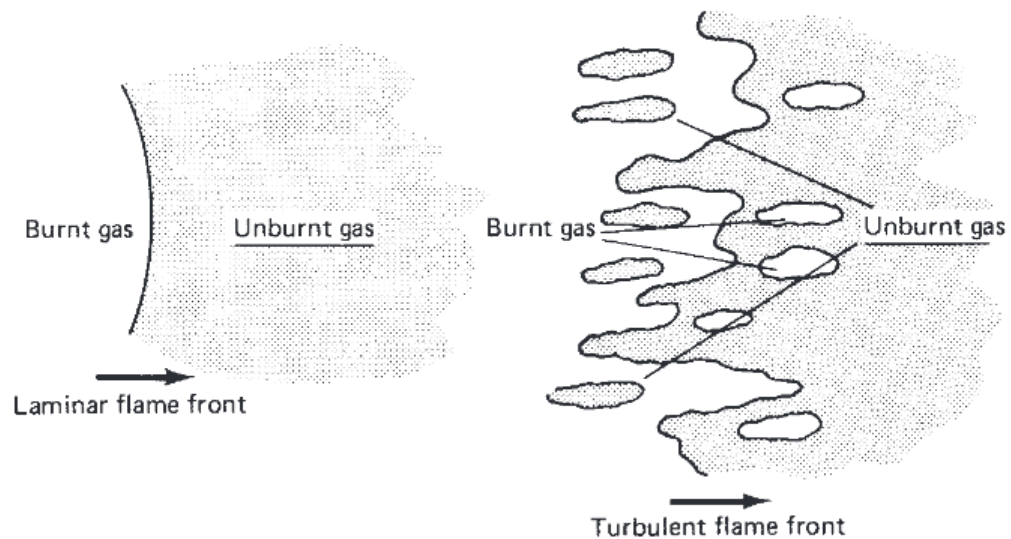
Figure 2.2: Laminar and turbulent flame fronts for pre-mixed combustion[7].

turbulence, there can be more pockets of burned gas in the unburned gas and vice versa, combustion still happens in a thin-reaction sheet regime [6]. The large-scale, low frequency flow structures which vary from cycle to cycle inside the cylinder influence mean flow but do not affect the local structure of the flame. This is due to characteristic time associated with local flame process is small compared to turn over time associated with the large flow structures inside the cylinder.

Combustion starts towards the end of compression stroke with spark ignition, continues through the early part of the expansion stroke, and ends after the point in the cycle at which the peak cylinder pressure occurs. If the spark ignition is advanced well before TDC, the compression work from the piston to the gases increases. If the end of the combustion process is much delayed by retarding the spark timing, the peak cylinder pressure occurs later in the expansion stroke and is reduced in magnitude. This reduced pressure magnitude decreases the expansion work transfer from the cylinder gases to the piston. So combustion event must be properly placed relative to the top dead centre to achieve maximum torque or power. The optimum ignition timing which gives the maximum brake torque or MBT (minimum ignition advance for best torque) timing occurs when the magnitudes of these two opposing trends just offset each other. In few operating points, it is difficult to achieve this optimum timing as auto-ignition of end gas restricts ignition timing advance.

The mass fraction burned profile as a function of crank angle has a characteristic S-shape, as shown in Fig. 2.3. The rate at which fuel-air mixture burns increases
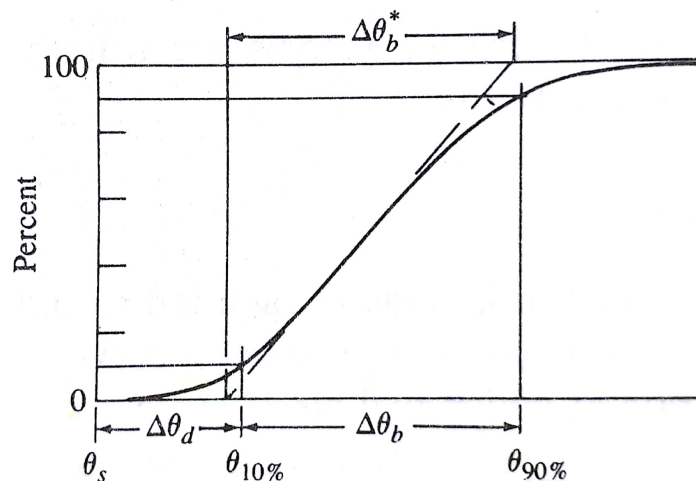
Figure 2.3: Mass fraction burned versus crank angle, flame development angle, $\Delta\theta_d$ and rapid burning angle, $\Delta\theta_b$ [5]

from a low value immediately following the spark discharge to a maximum about halfway through the burning process and then decreases to close to zero as the combustion process ends. The flame development process is identified by a point where a small but measurable fraction of the charge has burned. It is influenced mainly by the equivalence ratio, composition and flow field near the spark plug. The rapid burning stage, during which the major portion of the charge burns as the flame propagates to the chamber wall, is influenced by the conditions throughout the combustion chamber. The final stage, where the remainder of the charge burns to completion, cannot as easily be quantified because energy release rates are com-

parable to other energy transfer processes that are occurring [5].

Burning rate is also strongly influenced by engine speed. The duration of combustion in crank angle degrees only increases slowly with increasing engine speed. Hires et al. observed that the interval between spark and 90 percent mass burned fraction increases by a factor of 1.6 for a factor of 4 increase in engine speed [9].

Equivalence ratio is defined as the ratio of actual fuel-air ratio by mass to stoichiometric fuel-air ratio (Eq:2.2). Relative Air Fuel Ratio (λ), which is the inverse of equivalence ratio, is also a commonly used to represent the mixture composition (Eq:2.3).

$$\phi = \frac{(F/A)_{actual}}{(F/A)_{stoichiometric}} \tag{2.2}$$

$$\lambda = \phi^{-1} = \frac{(F/A)_{stoichiometric}}{(F/A)_{actual}} \tag{2.3}$$

Unburned mixture composition and state influence the burning rate. The burning duration is observed to be minimum for slightly rich mixture (λ=0.83) and increases substantially for leaner mixture [9]. The burned gas fraction in the unburned mixture, due to residual gas fraction or from recycled exhaust gases, increases burn duration significantly. Fuel composition can also influence the burn duration.

Based on ideal air standard Otto cycle thermal efficiency, Eq:2.4, thermal efficiency of gasoline engine can be increased by increasing compression ratio and by operating with lean mixture ($\gamma > 1$).

$$\eta_{therm} = 1 - \frac{1}{r_c^{\gamma-1}} \tag{2.4}$$

Where r_c is the compression ratio and γ is the ratio of specific heats. The variation of γ with respect to temperature and equivalence ratio is shown in Fig. 2.4. So, working with lean mixture and at a lower temperature results in higher γ and hence achieves higher thermal efficiency. The variation in thermal efficiency for a constant volume fuel-air cycle is shown in the Fig. 2.5. Though for a real engine, there is a limit for highest compression ratio and lean limit that can be achieved. Higher compression ratio increases heat transfer and also causes end gas auto ignition. Whereas, operating at higher lean limit can result in high cyclic variations and resulting driveability issues. Both these limiting factors will be discussed in detail in the following sections.
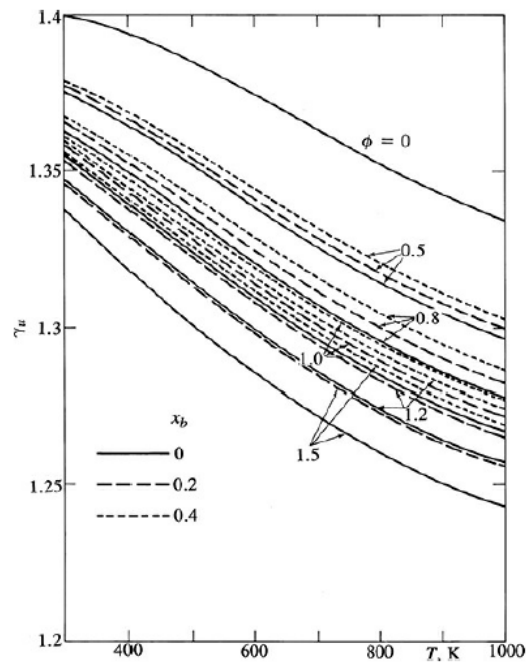
Figure 2.4: Ratio of specific heats, γ, of unburned gasoline, air and burned gas mixtures as function of temperature, equivalence ratio and burned gas fraction (x_b)[5].
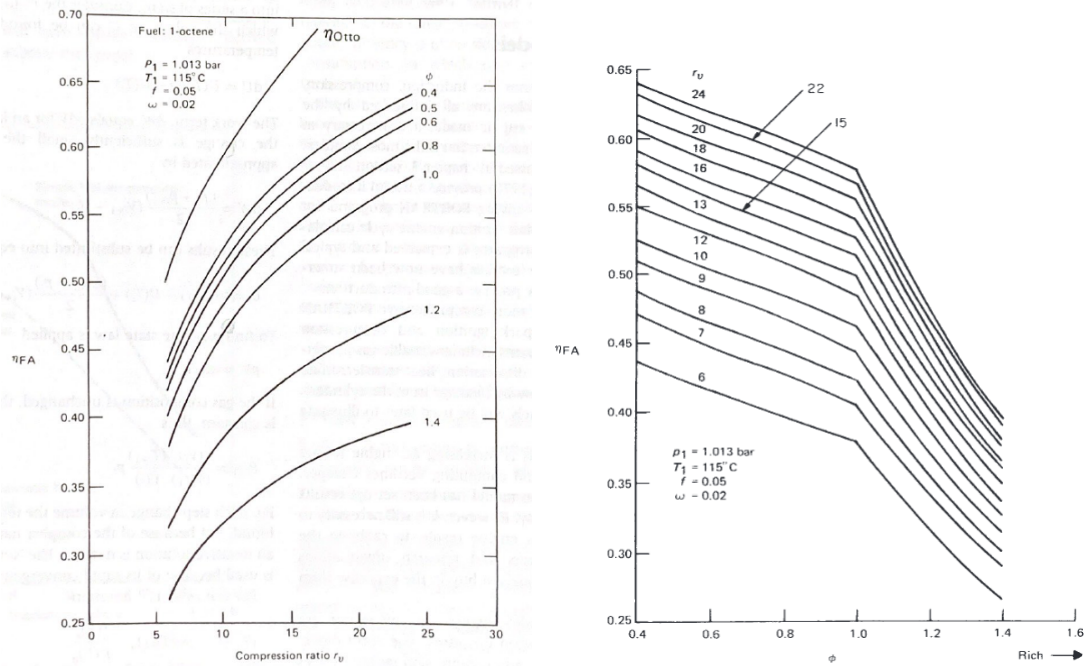
Figure 2.5: Variation of thermal efficiency with compression ratio and equivalence ratio for a constant-volume fuel/air cycle with 1-octene fuel [7].

2.2   Lean burn combustion

An IC engine based on constant-volume fuel/air cycle achieves higher thermodynamic cycle efficiency when it operates at equivalence ratio below unity. For lean mixture, the burned gas temperature after combustion decreases, decreasing the burned gas specific heats and thereby increasing the effective value of γ over the expansion stroke. The efficiency increases because, for a given volume expansion

ratio, the burned gases expand through a larger temperature ratio prior to exhaust and hence, for a unit mass of fuel, the expansion stroke work is increased [5]. Lean combustion reduces peak cylinder temperature as heat is utilised to heat up excess air and hence reduces dissociation losses and net heat transfer to the cylinder wall, further contributes to higher efficiency.

A lean burn engine generally requires high ignition energy, long duration of spark ignition and a wide dispersion of ignition sources in order to achieve fast burn rates [5]. Also the narrow flammability limits of most fuels make it difficult to run lean while maintaining adequate combustion stability with low misfire rates [10]. The lean limit depends on flammability of the fuel-air mixture. The flammability limit is a property of the fuel and should be independent of the ignition source and combustion chamber design. In engines, however, the effects of the ignition source, chamber geometry, and mixture motion cannot be ignored. A conventional spark ignition engine does not allow higher lean level as it fails to initiate the combustion and results in a high cycle to cycle variation and subsequent drivability issues. To ensure burning in lean mode, an alternative high energy ignition system is required. With a suitable ignition system in place, a higher lean limit towards the flammability threshold can be targeted until the pumping loss for increased air flow outdoes the thermal efficiency gain.

The flame propagation speed inside a combustion chamber is dependant on both laminar burning velocity and turbulence level. As explained earlier in this chapter, laminar burning velocity is a property of mixture. For lean mixtures, laminar burning velocity reduces substantially as shown in the Fig. 2.6. Higher turbulence level can increase the net flame speed (turbulent flame speed) as shown in the Fig. 2.6 which could negate the reduction in laminar flame speed with lean mixture. But there are additional issues associated with increasing turbulence level, for example: volumetric efficiency is affected due to increased masking required for high tumble generation and can results in higher pumping losses to achieve the same equivalence ratio. Also, excessive turbulence can leads to increased heat transfer as turbulence promotes convective heat transfer to the combustion chamber walls.

2.3   Cyclic variations

One important measure of cyclic variability, derived from in-cylinder pressure data, is the coefficient of variation in indicated mean effective pressure. It is the standard
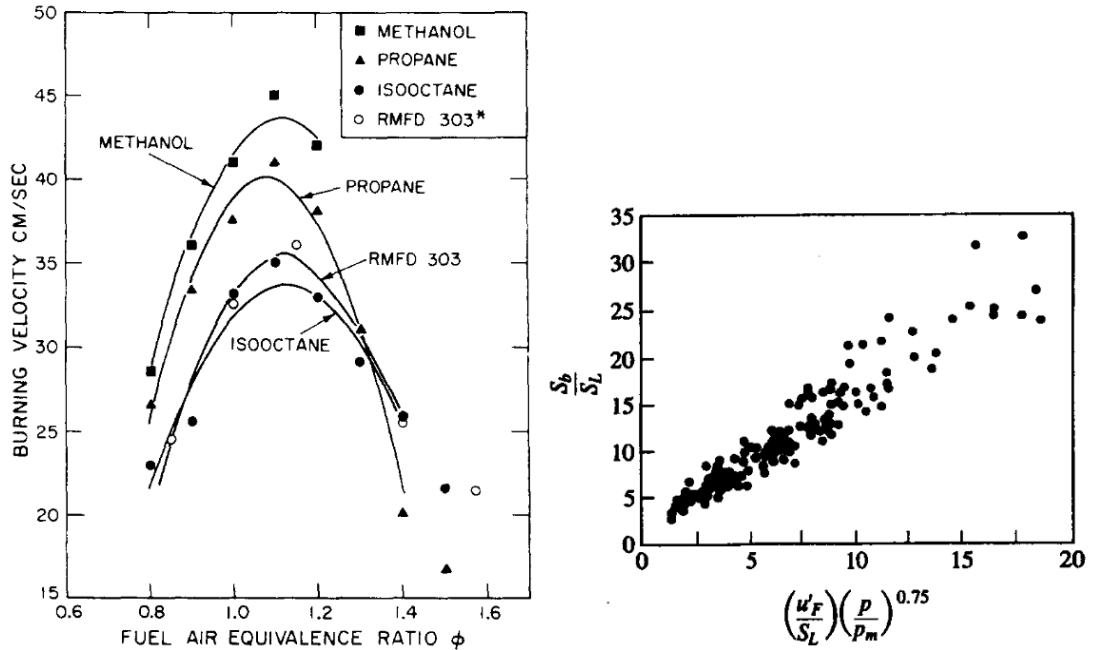
Figure 2.6: Left: Dependence of the burning velocity of mixtures of methanol, propane, iso-octane, and blended fuel indolene (RMFD303) with air on the fuel-air equivalence ratio [11]. Indolene closely represents gasoline fuel. Right: Dependence of ratio of turbulent burning velocity to the laminar flame velocity on the turbulence intensity [12].

deviation of imep divided by the mean imep, and is usually expressed in percent [5].

$$COV_{imep} = \frac{\sigma_{imep}}{imep} X100 \tag{2.5}$$

During combustion, the rate of change of pressure is substantially affected by the rate of change of cylinder volume, the rate of burning and changes in the phasing of combustion process relative to TDC. Fig. 2.7 illustrates how the magnitude of the maximum cylinder pressure and the crank angle at which it occurs vary with respect to combustion start angle. For fast burning heat release, maximum pressure decreases and crank angle at which maximum pressure occurs increases as the combustion start is delayed. For slow-burning heat release, peak pressure approaches motored pressure at TDC as combustion is delayed. For fast burning mixture, most of the heat release happens when the piston is near TDC and rate of change of volume is less. Thus pressure variations are mainly due to combustion variations. With a slow burning mixture, substantial heat release happens when the change in volume is also significant, resulting in amplifying the effect of combustion variations on the peak pressure values. Thus, fast burning combustion process significantly reduces the impact of cyclic combustion variations on engine performance [14].

Hansel [15] observed cyclic variation in combustion is mainly due to three factors:

1. The variation in gas motion in the cylinder during combustion, cycle by cycle
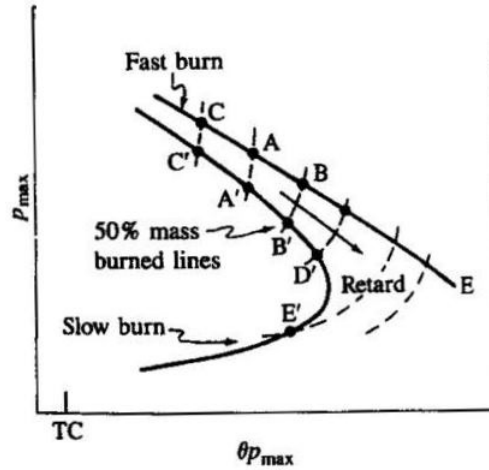
Figure 2.7: Schematic of variation in maximum cylinder pressure and crank angle at which it occurs, in individual cycles. $CABE$ typical of fast heat release process,$C'A'B'E'$ typical of slow heat release process. A corresponds to MBT timing, B represents retarded timing and C represents advanced timing with respect to MBT [13].

2. The variation in the amounts of fuel, air, and recycled exhaust gas supplied to a given cylinder each cycle

3. Variations in mixture composition within the cylinder each cycle, especially near the spark plug, due to variations in mixing between air, fuel, recycled exhaust gas and residual gas

In an earlier literature study, Ozdor reviewed previous research works done on identifying various factors contributing to cyclic variability [16]. This detailed review analysed various factors including air-fuel ratio, fraction of diluents, mixture spatial inhomogeneity, variations in trapped mass, variation in mean flow vector, variation in spark discharge characteristics, spark gap, electrode shape, number of spark plugs, spark plug orientation with respect to mean velocity vector and overall in-cylinder flow pattern. This study summarises that all these factors influence the duration of either or both: the initial flame kernel development stage and the main combustion propagation stage. Author found it difficult to make a quantitative estimate of contribution from each factor, but states that the shorter are the combustion stages, especially, the initial flame development, the less are the CCV in combustion. This review identified elimination of cyclic variation could lead to a 10% decrease in BSFC for same fuel consumption.

From a Large Eddy Simulation (LES) based numerical study of a pre-mixed gaseous fuel engine, Vermorel et al. [17] observed significant variations in the aerodynamic field, resulting in varying flow and turbulence level near the spark plug on different cycles and influence flame development and propagation. A number of factors identified for cyclic variability of flow field. First, the variations of overall

Sources = variation of:	Effect on combustion start		
	Unstab lean	Unstab dil	Ozdor et al.
Global A/F ratio	++	N.A	++
Global dilution	++	++	++
Spatial inhomogeneities	+	-	+ to +++
Flow convection	+++	++	+++
Sources = variation of:	Effect on the main propagation phase		
	Unstab lean	Unstab dil	Ozdor et al.
In-cylinder mass	++	++	+++
Global A/F ratio	++	N.A	++
Global dilution	++	++	++
Global flow motion	-	+	++

Table 2.1: Qualitative impact of different sources of CCV, The meaning of the symbols is as follows: +++: very strong correlation, ++:moderate correlation, +: weak correlation, -: no measurable impact and N.A.: not applicable [20].

combustion rate lead to small variations in the thermodynamic conditions of the residual gases remaining in the cylinder, which lead to small variations in the in-cylinder conditions upon intake valve opening. Second, turbulent flow naturally leads to cyclic variations, as its non-linear behaviour can amplify slight cyclic differences that would otherwise have a negligible effect. The cyclic variations do not affect integral quantities like overall mass flow, but lead to local differences in flow structure that find an important amplification via tumble breakdown and combustion.

Adomeit et al. [18] observed that interaction of fluctuating flow and direct fuel injection leads to substantial increase in cyclic differences in cylinder flow, which affects spray penetration and mixture formation. Goryntsev et al. [19] also reported similar observation that flow field variations and its interaction with GDI spray resulting in air-fuel mixing process varying from cycle to cycle, and causing changes in fuel vapour cloud near the spark plug.

Truffin et al. [20] studied cyclic combustion variation using LES of a stable (low CCV) and two unstable (high CCV) operating points, of an SI engine fuelled with premixed gaseous propane. This study made a quantitative assessment of each factors causing cyclic variation. The results are compared with the findings by Ozdor et al., discussed in this section before. The results are reproduced in Table 2.1.

The discussed works here highlight that changes in flow convection near the spark plug as the most influential factor in cyclic variation of combustion start. Also, changes in large-scale flow structures and its interaction with spray can influence both combustion start and flame propagation. Based on these findings, it is evident that a GDI engine has higher chances of cyclic variations compared to

a port fuel injected gasoline engine and requires special attention to minimise the cyclic variations.

Cyclic combustion variation affects engine performance at full-load in two ways. Under knock limited speed and load operating points, a fastest burning cycle within the variations, produces highest cylinder pressure and results in end gas expose to favourable knocking conditions. A fastest burning cycle is characterised by shortest ignition delay and burn duration. Thus, the fastest burning cycle is expected to knock and restrict the ignition angle and compression ratio. The slowest burning cycle is either due to delayed burning or misfires and restricts the lean limit. So, cyclic variation limits both compression ratio and lean limit an engine can operate and in turn restricts the thermal efficiency. Cyclic variation reflects in engine brake torque delivery as well and can affect vehicle driveability [5].

2.4 Abnormal combustion

IC engine load is expressed with Brake Mean Effective Pressure (BMEP). Average BMEP in all engines has been increasing over the last three decades and in turbocharged engines, BMEP is increasing significantly [21]. This higher BMEP is achieved by increasing the compression ratio and rising inlet pressure by means of pressure charging. But, this increased BMEP level promotes abnormal combustions and hence prevents aggressive engine downsizing.

The discussion here is focused on spark knock as it is the main factor restricts compression ratio and inlet pressure. Other abnormal combustion phenomena like surface ignition are not discussed here for brevity. It is generally agreed that spark knock originates with the extremely rapid release of much of the energy contained in the end-gas ahead of the propagating turbulent flame [5]. This rapid release of energy results in a non-uniform pressure distribution inside the combustion chamber, causing pressure waves or shock waves to propagate across the chamber. These shock waves destroy thermal boundary layer and accelerate heat transfer from the cylinder and continues exposure to engine knock can result in component failure due to surface erosion from high temperature. The widely accepted auto-ignition theory states that when the fuel-air mixture in the end gas is compressed to sufficiently high pressures and temperatures, results in fuel oxidation process, starting with the pre-flame chemistry and ending with rapid energy release [5]. Auto-ignition of the gaseous fuel-air mixture occurs when the energy released by the reactions as heat is larger than the heat lost to the surroundings, as a result the temperature of the mixture increases, thereby rapidly accelerating, due to their exponential temperature

dependence to the rates of reactions involved. The end gas temperature gives a good indication for predicting auto ignition and is expected to observe at the regions in close proximity to exhaust valve and piston, which has a higher surface temperature than other water cooled combustion chamber surfaces.

In general, the rate of chemical reactions increases with temperature and higher gas temperature accelerates chain branching reactions that form the intermediate species that lead to auto-ignition [22]. An increase in the charge temperature prior to combustion reduces the time required for these reactions to complete, and make it more likely that required conditions for autoignition can exist in the unburned mixture before the normal flame front can progress to consume it. With this understanding, any measure that reduces the temperature of the remaining unburned mixture can reduce the tendency to knock. In a knock limited engine operation, not all cycles produce auto-ignition and hence, cyclic variation has an influence on engine knock resistance [7]. So any measure that can reduce cyclic variation can also benefit in achieving optimum combustion phasing.

For a given engine hardware, auto-ignition is usually avoided by spark retard for engine durability. This delaying of ignition angle from the optimum MBT timing leads to non-optimal combustion phasing with reduced thermal efficiency. Engine efficiency is said to be compromised once the 50% MFB point is retarded more than 12° ATDC [23]. To avoid this efficiency loss, combustion must be fast enough to consume all charge well before air-fuel mixture auto ignites at the farther end of the combustion chamber. As a knock mitigation strategy, in-cylinder turbulence level is increased to achieve higher turbulent flame velocity [5]. Once combustion is started, increased turbulence leads to fast combustion and decreases the tendency to knock [24].

Some of the other knock mitigation strategies successfully used by researches are briefly discussed here. Using a two-stage injection strategy on a GDI engine, Bai et al. [25] demonstrated stratified stoichiometric mixture could suppress knocking effectively compared with a homogeneous stoichiometric mixture case. Investigation of a two-stage strategy indicated that locally slightly rich mixtures due to a late injection help to suppress auto-ignition by providing a local cooling effect and by enhancing the local flame propagation speed [26]. In a literature study, Wang et al [27] concluded that two-stage injection is an effective method for suppressing knock under high load operating conditions. However, the injection strategies and combustion system need to be optimised to avoid soot emissions. Cooled EGR admission along with air-fuel charge has the potential in knock mitigation without loss of output power [28]. This is because cooled EGR lowers the charge air temper-

ature due to its higher heat capacity, and more fuel is consumed before reaching the knock temperature limit. Su et al. [29] reported 6-9% fuel economy improvement from an SI engine with compression ratio 10.9 and with 18-25% cooled EGR compared to a base engine specification of CR 9.3 and no EGR. This study pointed out that primary reason for higher thermal efficiency is from higher gas constant of cooled EGR and reduced heat transfer loss due to lower combustion temperature. On the contrary, high temperature internal EGR has a negative influence on knock suppression because of its heating effect, and must be avoided in gasoline engines. Mazda Motor Corporation used a 4-2-1 exhaust manifold timing sequence to reduce internal EGR and to decrease the temperature at TDC for suppressing knock [30].

For GDI engines, injecting excess fuel could increase charge cooling effect and decrease the temperature of the mixture, which could extend the time to end gas auto ignition and finally suppress knock [27]. However, the fuel enrichment is at the cost of reduced thermal efficiency and increased HC and CO emissions.

Surface temperature around the combustion chamber, especially on the exhaust side can be controlled to improve the knock resistance. Takahashi et al. [31] achieved higher knock resistance by increasing coolant flow near the exhaust valve and on the upper part of the cylinder liner aiming localised cooling of the combustion chamber. Paul et al. [23] developed a split system cooling circuits, one for the cylinder block and one for the cylinder head. The coolant was fed into the cylinder head below the exhaust ports first and then allowed a cross flow around the exhaust valve seats and guides, and then combustion chamber skull, ensuring good flow velocities in these areas.

Matsura et al. [32] observed that cylinder flow formed in the second half of the compression stroke is closely related to combustion and knock. In this study, knock onset position was first identified using an AVL Visio Knock optical sensor. The piston top shape was modified to increase flow velocity and turbulent intensity near the knock site with the aid of CFD study. During experimental validation, a heat flux sensor was used to measure local heat flux at the cylinder head, near where knock is expected. Improved local heat transfer enhanced knock resistance and achieved spark advance of 2.2^o over the base design with an increase in indicated thermal efficiency of 0.7%. This study shows that localised flow changes can be used to improve knock resistance by increasing local heat transfer in the end gas. This strategy is more beneficial than overall flow increase because of reduced heat transfer losses.

Through a literature review, Attard [33] compiled different factors influencing

auto-ignition with a corresponding octane number change, and same is reproduced in the Table 2.2.

Parameters	Octane Number Requirement	Range Tested
Spark advance	Increase 1 ONR/ 1° knock limited spark advance	$0 - 30^o$ CA
Intake air temperature	Increase 1 ONR /7^oC	$20 - 90^o$ C
Air-fuel ratio	Peaks around 5% rich of stoichiometric, Decreases 2 ONR/0.1 λ	0.8 - 1.6 λ
Dilution: cooled EGR	Decrease 3-4 ONR/10 % mass diluent	0-20% mass diluent
Manifold absolute pressure	Increase 3-4 ONR/10 kPa	85-135 kPa
Compression ratio	Increase 5 ONR/CR	5-12 CR
Exhaust back pressure	Increase 1 ONR/30 kPa	0-65 kPa
Coolant temperature	Increase 1 ONR/10^oC	$70 - 110^oC$
Altitude	Decrease 1.4 ONR/300m, Decrease 2.5 ONR/300m	0-1800 m, 1800-3600 m
Humidity	Decrease 1 ONR when increasing relative humidity from 40% to 50% at 30^oC	-
Engine deposits	Increase 6-9 ONR over life of engine	0-250000 km
Excessive oil consumption	Increase up to 12 ONR depending on driving cycle	-
Type of fuel injection	Decrease 4 ONR when DI used over PFI	-
Increasing squish	Decrease up to 5 ONR as squish areas increases	0-67 % squish area
Combustion chamber shape	Decrease up to 15 ONR from cylindrical to modern type chamber	7.8-11 CR
Hydrogen (H2) addition	Decrease 1 ONR / 1% H_2 added	0- 12 % H_2 added

Table 2.2: Effect of various parameters on the octane number requirement (ONR) of a spark ignition engine [33].

2.5 Emissions

The UK and French governments are considering a total ban of internal combustion engines by 2040 due to harmful emissions and the resultant impact on public health

[34]. CO_2 is a greenhouse gas and a major contributor to global warming. The main motive behind engine downsizing is to reduce CO_2 by generating same power of a larger capacity engine efficiently from a lower displacement engine. NOx emissions are a threat to public health. One crucial development in reducing NOx emission would be low-temperature combustion, through which dissociation and nearly 100% NOx emissions can be eliminated [35]. Eliminating dissociation losses is an added benefit to thermal efficiency. To achieve low-temperature combustion, the lean operating limit has to be increased.

It is observed that GDI engines typically emit between 10 to 40 times more particulates (by mass) than PFI engines [36]. As of now, over 90% of the EU population is estimated to be exposed to levels of particulate pollution that represent a risk to health [37]. The major reason for particulate emissions is poor mixture formation inside the cylinder due to reduced mixing time compared to PFI engines. GDI permits lesser time for spray atomisation and vaporisation before combustion starts. Different spray parameters can be optimised to improve mixing. An accurate numerical modelling capability helps in evaluating strategies to improve mixture formation inside the cylinder.

This thesis is concerned with implementation of pre-chamber combustion system for reducing engine fuel consumption and BFSC, and not focused on reducing harmful engine emissions, further efforts are not put in to understanding engine emissions and the methods to reduce emissions. Nevertheless, improving thermal efficiency generally has a positive effect on emission reduction.

Chapter 3

Pre-chamber ignition systems

Contents

3.1   Novel ignition systems

This section discusses previous works done on combustion improvement using advanced ignition systems. Ignition enhancement involves increasing the ignition energy in order to improve the burning characteristics of the fuel. Despite many decades of research, the spark plug based combustion system remains almost the same even today. This single source combustion initiation leading to smooth flame propagation results in a definite combustion duration angle against the constant volume combustion of ideal cycle. Researchers tested various alternative ignition methods to replace spark based ignition, notably HCCI, laser and plasma ignition systems [10]. In homogeneous charge compression ignition (HCCI), a homogeneous mixture of fuel and air at uniform pressure and temperature at all locations in the combustion chamber is prepared. The heat release is chemically controlled and occurs at all points due to auto-ignition, resulting in very short burn duration. This short burn duration has been found to be a significant limitation at higher loads, because either combustion phasing or heat release cannot be controlled, as in spark ignition engines and compression ignition engines [38]. So these methods are yet to achieve their wider implementation, either due to complex hardware requirements or combustion improvements limited to a narrow speed and load range. Pre-chamber ignition system is identified as a novel ignition system which is relatively easier to implement, compared to the other methods discussed in this section.

3.1.1 Pre-chamber ignition systems

In pre-chamber ignition system, multiple turbulent flame jets from a pre-chamber burn air-fuel charge inside the main combustion chamber in much shorter duration compared to a conventional spark ignition system. The shorter burn duration reduces end gas residence time at elevated pressure and temperature. Hence, the pre-chamber system reduces the engine knock and can aim for higher compression ratio and inlet boost pressure. Also, the multiple ignition sources from a pre-chamber ignition ensure combustion in lean mode and can extend the higher lean limit [39]. Pre-chamber ignition systems attracted researcher's interest mainly due to relatively simple hardware requirement over other novel ignition systems. Researchers worked on various pre-chamber design concepts, and these divided chamber systems are characterised by having either

- large or small pre-chamber volumes

- auxiliary pre-chamber fuelling

- large or small orifice(s) connecting pre-chamber to the main chamber [39]

Initial pre-chamber designs were characterised by a large pre-chamber volume and large orifices. Honda [40] implemented Compound Vortex Controlled Combustion (CVCC) system in 1975, which operates by rich mixture introduced into an auxiliary combustion chamber, where the spark plug is located, via a separate intake valve. The auxiliary combustion chamber is connected to the main combustion chamber where lean mixture is present, via a torch opening. The aim of this design is to reduce three pollutants (CO, HC and NO_X) according to emission regulations through lean operation and this objective was achieved without an after-treatment system.

Robinet et al. introduced APIR ignition concept [41]: APIR is the French acronym for "Self-ignition triggered by radical injection", is a pre-chamber concept with pre-chamber volume of about 1% of the clearance volume. The hole diameters used in the experiment ranged from 0.5 to 0.8 mm and such a small diameter helped in quenching the flame and reappearing at a farther end of the combustion chamber. Up to 10 number of smaller holes used, spreading intermediate combustion products across the main combustion chamber, initiating self-ignition at several sites. The main chamber was fed with a lean mixture and rich mixture close to upper flammability limit was fed into the pre-chamber via a feed line at spark timing. Cyclic variation in P_{max} and crank angle at P_{max} is divided by a factor of 5 and substantial reduction in ignition delay and burn duration is achieved. For same operating conditions and combustion phasing, the reported IMEP is lower by 3% due to increased heat transfer losses. At full load with APIR pre-chamber, the engine could

operate at its MBT spark timing without knock occurrence, which was not possible with the base spark ignition. With this less knock occurrence, a 4% reduction in fuel consumption was reported and author estimates further reduction of 10% fuel consumption by increasing compression ratio by 2 units.

Couet et al. studied [42] the influence of in-cylinder aerodynamics and knock sensitivity with APIR ignition system. This study reported that influence of tumble and swirl on combustion is weaker when using with APIR device. A drop in efficiency was reported with increased tumble and swirl level, due to increased heat transfer losses. This study also reported better knock resistance with APIR ignition.

Toulson [10] reviewed previous research works done on pre-chamber ignition system and also detailed how jet ignition improves the burning rate. The pre-chamber jet ignition concept involves the use of a chemically active, turbulent jets to initiate the combustion in lean fuel mixtures. The hot reacting jet produced by a turbulent jet ignition has two effects on the combustion in the main chamber. First, the generation of turbulence produced by the shear of the jet flow increases the flame propagation speed. Second, the jet distributes hot gases over a wide region in the main chamber which generates distributed ignition throughout the chamber where the jet has passed. A large number of distributed ignition sites ensure that the flame travel distances are relatively small enabling short combustion durations, even in slow-burning lean mixtures. Similar to HCCI, chemical kinetics plays a much larger role in determining combustion characteristics in the turbulent jet ignition. Both HCCI and jet ignition rely to some extent on chemical kinetics to initiate combustion. With HCCI, combustion is dominated by the kinetics of intermediate temperature hydrocarbon ignition, which occurs in the cylinder mixture during compression, with ignition occurring when the temperature of the core fuel-air charge reaches the H_2O_2 decomposition temperature [43]. With the jet ignition, the active radicals present in the partially combusted products ejected from the pre-chamber aid in initiating main chamber combustion by producing multiple, distributed ignition sites, which rapidly consume the main chamber charge. The smaller orifice size causes the burning mixture to travel quickly through the orifice, which extinguishes the flame and seeds the main chamber with reacting active radical species that reignite some distance away from the pre-chamber. In addition, the smaller orifice creates a flame jet that penetrates deeper into the main charge. However, to avoid impinging on the combustion chamber wall, the pre-chamber volume has to be kept relatively small.

Evaluation of pre-chamber design and performance is a challenging task, mainly due to the smaller volume of the pre-chamber and resultant difficulty in instrumen-

tation. A drilled tunnel used for pre-chamber pressure measurement acted as a knock site as reported by Chinnathambi et al. [44]. So a CFD model is a useful tool for evaluating pre-chamber design.

Thelan et al. [45] studied the influence of orifice size in a pre-chamber using a numerical model of Rapid Compression Machine (RCM). A homogeneous lean mixture of propane and air was used with relative AFR (λ), 1.27. The volume of pre-chamber is approximately 1 cm^3, which is 2% of main combustion chamber volume. Four simulations with orifice diameters of 1.0 mm, 1.5 mm, 2.0 mm and 3.0 mm respectively examined in CONVERGE CFD code. The focus of this study was the combustion induced in the main chamber by turbulent jets from the pre-chamber. It was observed that orifices with smaller diameter up to a limit produce faster burn rates, mainly attributed to the increased amount of turbulence generated by higher velocity jets. The optimum diameter for the experiment observed to be 1.5 mm and a smaller diameter of 1.0 mm tested, failed to show reduction in burn duration. Author explains reduced hot jet flow and higher heat losses with a very small diameter could be the causes, despite it produces higher turbulence. In this study, author identified five distinct phases as compression phase, pre-chamber combustion initiation phase, the cold jet phase, the hot jet phase and flow reversal phase. The change in behaviour of these five phases with respect to orifice diameter helped to explain the detailed mechanism relating orifice diameter to burn rate.

Thelen et al. [46] continued the study using same numerical model for identifying an optimum spark plug location inside the pre-chamber. This study suggested that the spark plug location must be far away from the orifice, so that mixture inside the pre-chamber was burnt maximum prior to ejecting hot gases outside. Conversely, if the spark location is close to the orifice, the delay between spark and production of a hot jet in the main chamber is reduced, but jet from later burning inside the pre-chamber is essentially wasted as it just ends up emitting hot gases into a core region in the main chamber that has already been burned. One crucial design challenge of pre-chamber ignition system is to remove burned gas products from the pre-chamber after completion of combustion and fill it with combustible fresh air-fuel mixture, or simply described as scavenging process in this thesis. Thelen et al. [46] identified that a farther located spark plug design option has the difficulty in scavenging the exhaust gas near the spark plug electrodes. Hence, ignition source needs to be located as far away from the orifice as possible in a place that provides a consistently ignitable mixture.

If the main objective is to develop lean burn combustion, it is necessary to have combustible mixture near the spark plug. This requirement is even valid for a pre-

chamber ignition system where pre-chamber ignition is initiated by a spark plug. So a higher lean limit mixture necessitates an arrangement to achieve rich mixture near the spark plug. This can be done either by making a stratified mixture by spray or wall guided injection or using an additional injector inside the pre-chamber. In an earlier study by Gussak [47], it was identified that availability of active radicals in the pre-chamber jets increased as the mixture in the pre-chamber was made richer, up to a certain limit. This work also identified that jets of hotter, but complete combustion products are generated when a stoichiometric or slightly leaner mixture is burned inside the pre-chamber. These jets had significantly lower combustion performance compared to the jets generated by burning a richer mixture due to higher concentration of active radicals.

Kettner et al. [48] developed a Bowl Pre-chamber Ignition concept with a bowl shape was made on the piston to guide fuel towards the pre-chamber. This study used multi-stage injection having a second stage injection with a small quantity of fuel (about 3 % of the total fuel mass) is directed towards the piston bowl, injected towards the end of compression stroke. The enriched air-fuel mixture in the piston bowl is transported by the piston motion towards the pre-chamber spark plug. With the pressure difference between the main chamber and pre-chamber during compression stroke, the mixture is transported with a highly turbulent flow into the pre-chamber. The first injection during intake stroke leads to a homogeneous mixture with an air-fuel ratio of λ =1.4 to 1.7. The reported benefits are a reduction in fuel consumption, higher knock resistance and reduced CCV over the base engine. A loss in IMEP was reported for same operating conditions.

An alternative method to ensure rich mixture inside the pre-chamber is to have a separate fuel injection inside the pre-chamber. Using a liquid fuel in the pre-chamber is a challenging task due to less space available for vaporisation and homogeneous mixture formation. Some of the initial experiments conducted with the help of gaseous fuel inside the pre-chamber and gasoline in the main chamber. William Attard did extensive studies on turbulent jet ignition with pre-chamber injection ([49],[33],[50],[51],[52]). Initial studies conducted on a gaseous pre-chamber fuel and later managed to do tests with gasoline in pre-chamber. Test results proved that turbulent jet ignition significantly extends the excess air dilution rates when compared to conventional spark ignition combustion. A lean limit of lambda, 1.94 was achieved against 1.4 of the base PFI engine at a combustion stability of 5% CCV in IMEP$_{\text{gross}}$. Thermal efficiency of 40.3% was achieved against 34.2% of the base stoichiometric PFI engine.

Chinnathambi et al [44] conducted a numerical study using CONVERGE CFD

code to understand pre-chamber combustion and studied three pre-chamber designs and discussed the correlation to already available experimental data. Each design tested with different compression ratio and intake pressure. In this study, the pre-chamber peak pressure is observed to be a function of pre-chamber volume, combustion conditions and the nozzle diameter. In one design option with the boosted condition, despite the use of pre-chamber injector, lean mixture was observed near the spark plug at the combustion start. This is due to dilution of pre-chamber charge with ultra-lean main chamber charge. So, earlier pre-chamber injection may aid in vaporisation by providing additional time but there is a possibility of over mixing due to constant inflow of ultra-lean charge from the main chamber. Conversely, late injection benefits in achieving rich mixture stratification at the time of spark but at the cost of less vaporisation of pre-chamber injected fuel. The highest jet velocity was observed in a case with lowest compression ratio, showing a dependence of jet penetration length on the main chamber pressure. This study also reported that a richer than stoichiometric overall lambda in the pre-chamber produced more active radicals than slightly leaner mixture even if the mass flow from the pre-chamber is doubled, emphasising the importance of mixture state than total mass inside the pre-chamber. The jet penetration was asymmetrical due to the nature of flame development inside the pre-chamber.

A pre-chamber ignition system has a potential drawback in scavenging pre-chamber, especially at part load operating points [5]. Ravi et al. [53] included a high pressure air injector inside the pre-chamber to aid scavenging and to achieve better control of pre-chamber equivalence ratio. This single cylinder engine has a compression ratio of 12.0 and experiments conducted at wide open throttle using both lean air/fuel mixture ($\lambda \approx 1.8$) and nitrogen diluted (30 %) near stoichiometric mixture. This engine exhibited high combustion stability in both cases with COV in IMEP less than 2%. Without intake dilution, reported thermal efficiency is 46.8% at 1500 rpm and 6.0 bar IMEP. With intake dilution, observed thermal efficiency is 46 % and author reported a thermal efficiency penalty of 0.5% for pumping work to get high pressure pre-chamber air injection. In this experiment, main chamber was fuelled by a port injection system and for a typical GDI engine, placement of two gasoline injector, spark plug and an air injector around the combustion chamber would be a challenging design task.

A pre-chamber based ignition system has good potential in knock limit extension, by virtue of multiple ignition sites. Attard et al. [33] compared knock limit of conventional spark ignition and pre-chamber jet ignition by reducing fuel quality on a PFI base engine. Different PRF (Primary Reference Fuel) with varying Octane Number ((Research Octane Number+Motor Octane Number)/2) was tested on a

stoichiometric normally aspirated engine at 1500 rpm and at Wide Open Throttle (WOT). The initial study was conducted without auxiliary fuel injection inside the pre-chamber. At MBT combustion timing, a 10 Octane Number improvement was reported. With delayed spark timing, this engine could operate on 65 Octane fuel, producing combustion stability of 3% CoV in IMEP, which is more than 15 Octane Number difference from the base engine. These benefits in Octane Number reduction correspond to compression ratio increase of 3 points over the base engine compression ratio of 10.4. Later studies performed with auxiliary fuel injection enabled, helps in further burn rate enhancement and further 3 ONR improvement over the passive pre-chamber system. The reported reduction in 10-90% MFB duration is around 50%. However, for a given anchor angle (MFB50%), jet ignition produces less IMEP and author reasons it with higher heat losses from additional pre-chamber surface area and higher heat release rates. So higher compression ratio or spark advance is necessary to get a higher load from the jet ignition system.

In another study, Attard et al. [39] studied flame kernel development inside the pre-chamber with variations in spark plug type, orientation, location and electrode gap for an auxiliary fuelled pre-chamber combustion system. Experimental results highlighted that the pre-chamber system is quite robust and largely unaffected by spark plug design changes, unlike conventional spark ignition combustion [54]. This study also recommends a flush mounted spark plug assembly inside the pre-chamber to avoid high residual gas trapped near the spark plug. Attard et al. [35] also observed that ignition energy required for jet ignition combustion can be significantly reduced to very low levels (5-10 mJ) while maintaining good combustion stability.

A swirl pre-chamber design is used by Geiger et al. [54] to extend lean limit operation of a base naturally aspirated PFI SI engine. The pre-chamber volume is about 2% of clearance volume and swirl is created by tangential entry orifices. At stoichiometric operation, the only improvement reported was reduced flame development duration. Higher ISFC and higher standard deviation in IMEP were observed. Even the lean limit achieved was less compared to base spark plug design and author explains higher residual fraction inside the pre-chamber causing unstable combustion at a higher lean limit. This study continued with a modification in the pre-chamber design by providing a scavenging circuit, initially by air and later by methane. Scavenging with air could extend lean limit comparable to spark plug design and with methane scavenging, the lean limit could extend up to $\lambda \approx 1.96$ and is higher over the base spark plug design ($\lambda \approx 1.57$). This study reiterates the difficulty of pre-chamber functioning at part load and naturally aspirated condition where fraction of residuals is higher.

Pre-chamber operation limitations

Pre-chamber ignition concept has a few drawbacks mentioned in the literatures, some of which already discussed in the previous section. The reported observations are summarised here.

- Poor scavenging at part load and resultant combustion instability due to increased percentage of residuals inside the pre-chamber.

- Although jet ignition systems provide additional ignition energy, there are higher heat losses than conventional systems due to the additional surface area of the pre-chamber. This increased heat transfer can reduce thermal efficiency gain.

- At higher engine speed, heat transfer from the pre-chamber could be a concern for component durability and can hence limit spark advance or BMEP. Attard et al. [33] reported pre-ignition events inside the pre-chamber at higher engine speeds (5500 rpm) when operated with a stoichiometric mixture. Hamori [55] observed that Aluminium is not a suitable pre-chamber nozzle material because of orifice erosion. Anderson et al. [56] reported that high temperature resistant stainless steel is also not a suitable for pre-chamber construction, due to low thermal conductivity of the material which leads to high surface temperatures and resultant pre-ignition. The same study by Anderson recommended a mild steel nozzle as a compromised solution between mechanical strength and heat transfer.

- While studying knock resistance with APIR system: a study discussed here before, Couet et al. [42] observed pressure oscillations inside the main chamber from the start of combustion. Whereas in a spark ignition case, pressure oscillations reported from the peak of the pressure curve. The oscillation fundamental frequency is the same as that generated by knock and hence, it becomes difficult to differentiate knock from pre-chamber induced oscillations. To differentiate both knock events, heat release is computed without wall heat transfer and a criteria was devised as: when the heat release peak is higher than maximum heat release rate without knock, there is knock and when the heat release isn't higher than the maximum heat release rate without knock, knock can occur, but it has a very low intensity.

- Attard et al. [33] also reported jet knock from pre-chamber even when the engine operated at heavily retarded spark timing where there is no chance of auto-ignition in an SI engine. Author explains jet knock is characterised by small pressure oscillations similar to conventional end-gas knock, only significantly smaller in magnitude and initiated just after the start of ignition instead

of towards the end of combustion. These jet knocks caused pre-chamber based engines always operate at some knock level, which may not be as damaging as spark knock. Other than what discussed here, there is no literature available on pre-chamber jet knocks.

- Attard et al. [51] also observed that pre-chamber distributed ignition can result in high pressure rise rates, beyond the acceptable limit of spark ignition engines, placing increased loading on components. Nevertheless, this pressure rise rate cane be controlled through different ways, for example: delaying ignition timing. This implies that achieving shortest burn duration must not be the sole criteria, but pressure rise rate must be controlled to a tolerable limit.

- The separate injector inside the pre-chamber is with added complexity. To improve mixing inside the pre-chamber, vaporised gasoline directly injected inside the pre-chamber [50]. This is in addition to different fuel delivery systems required for main injection and pre-chamber injection.

3.2   Summary of literature review

This section summarises findings from the literature study on gasoline engine combustion and pre-chamber ignition systems.

- A gasoline engine performance at full load is restricted by cyclic variations and spark knock.

- For a GDI engine, variation in mean flow field and its interaction with direct injected spray formation are the most influential factors for cyclic variations.

- A pre-chamber based combustion system can reduce burn duration by around 50% over a spark plug ignition system.

- Pre-chamber ignition system can increase knock resistance over a base SI engine. But with a pre-chamber system, additional jet knocks are observed from the start of the combustion.

- With the same operating conditions of ignition timing and cylinder loading, pre-chamber based combustion produces less IMEP, due to increased heat transfer losses. Thermal efficiency from the pre-chamber based engine can be increased by extending the lean limit, combustion phasing advance or increasing the compression ratio.

- A pre-chamber based combustion can reduce cyclic variations based on:

  - Short burn duration or fast combustion reduces cyclic variation.
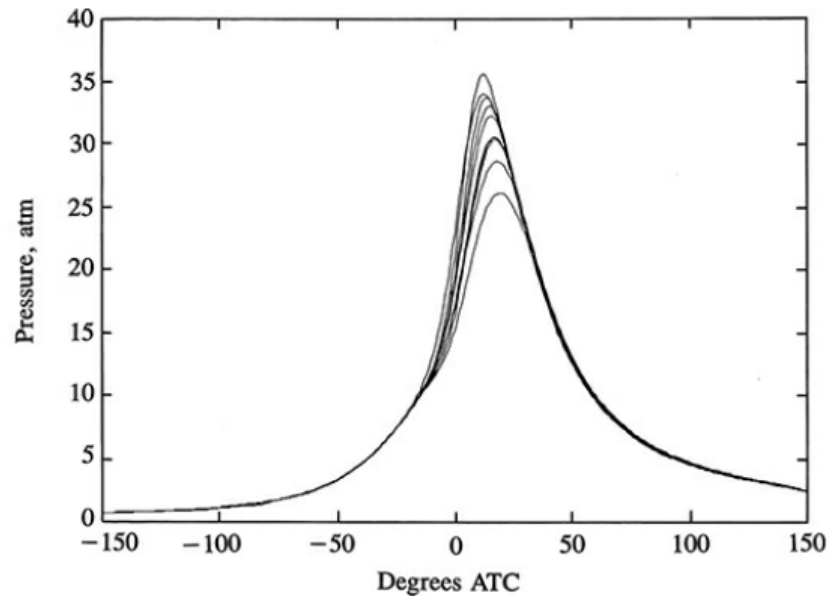
Figure 3.1: Measured cylinder pressure for 10 cycles in a single-cylinder spark-ignition engine operating at 1500 rpm, $\lambda=1$, MBT ignition timing=25° [5]

.

- With a pre-chamber ignition system, flow field inside the pre-chamber is decided by the reverse jet flow from the main chamber to the pre-chamber during the compression stroke and variation in large flow structures outside the pre-chamber is not passed inside the pre-chamber. For a typical gasoline engine, compression pressure curves are repetitive as shown in Fig. 3.1, ensuring constant pressure difference across the chambers for all cycles. Thus, a pre-chamber ignition system has the potential to reduce or eliminate cycle to cycle flow variations near the spark plug, which is located inside the pre-chamber.

- Pre-chamber performance is highly dependant on equivalence ratio inside the pre-chamber. A rich mixture inside the pre-chamber is much desirable, increasing active radicals in the turbulent jets.

3.3   Objectives of research

- The primary objective of this research is to reduce BSFC of a motor-sports engine by reducing cyclic variation and by increasing knock resistance of the engine, using a pre-chamber ignition system. The measured cylinder pressure data for the base engine is shown in Fig. 3.2 and it shows the level of cyclic variation present in this engine. The higher pressure curve represents a knocking cycle and is detected by a knock sensor and limits the combustion phasing advance. The lower pressure curve represents a mis-fire cycle or much delayed combustion, and decides the lean limit an engine can operate. The declared

(a) 100 continues cycles data

(b) Maximum, minimum and average data
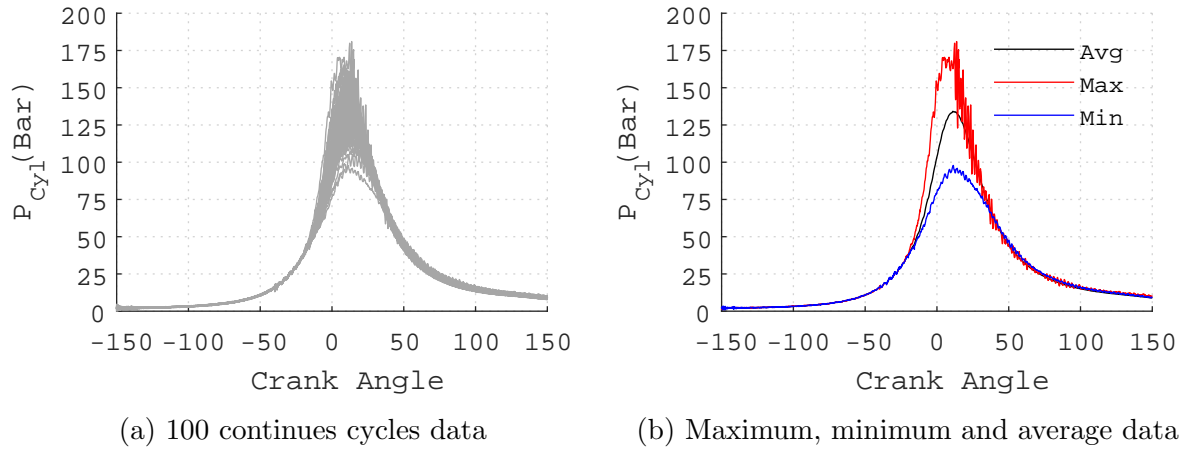
Figure 3.2: Cylinder pressure data for the base engine, 100 continues cycles, 7500 rpm and 13.32 kg-hr fuel flow rate.

performance and BSFC figures are decided by the average pressure curve. So a reduction in cyclic variation can increase the average pressure profile for a given knock limit. Alternatively, extending the lean limit for a given CCV value can also raise the average pressure profile and can declare lower BSFC.

- There is a limited literature available on pre-chamber ignition systems, especially on turbocharged GDI engines producing IMEP more than 20 Bar. Also, maximum engine speed researchers evaluated pre-chamber so far is 5500 rpm [51]. The motor-sport engine, based on a single cylinder engine is developed for this research, mostly operates between 6000 to 8000 rpm and produces around 30 bar IMEP. This research aims to study the impact of pre-chamber on a turbocharged motor-sport gasoline engine in improving thermal efficiency.

- In an SI engine, transducer type sensors are often used to detect knock and adjust spark timing to achieve optimum performance and durability [5]. With a pre-chamber system in place, jet knocks can influence the knock sensor reading. This research aims to study the corrections required in engine calibration to differentiate excitations from spark knock and jet knock.

- This research also aims to do a parametric study, using a CFD model to identify the limited number of pre-chamber designs for experimental testing.

Chapter 4

Engine CFD Model

Contents

4.1   Introduction

This chapter discusses the development of a multi-dimensional engine model for a pressure-charged GDI single cylinder engine and the various modelling approaches used to capture flow, combustion and fuel spray. This engine model represents single cylinder version of the base turbo-charged V6 engine.

Engine modelling can be classified based on, in what detail thermodynamic and fluid dynamic aspects are addressed. Stone [7] briefed different engine modelling methods as follows:

1. Zero-dimensional models (or phenomenological models). These models use empirical heat release models like Wiebe model to define heat release, which is only a function of time.

2. Quasi-dimensional models. These models consider burned and unburned zones and use a sub model to define heat release.

3. Multi-dimensional models. These models solve equations for mass, momentum, energy and species conservation to predict the flame propagation.

Even though Multi-dimensional models are most accurate, they are computationally intensive. Engine combustion performance is also influenced by other auxiliary engine systems including intake system, exhaust system and turbo-charger. Modelling complete engine with all auxiliary systems, even for a single cylinder engine, is computationally prohibitive. A better approach would be to model the complete engine with a one-dimensional engine modelling tool with simplified combustion models like zero-dimensional models and quasi-dimensional models. Overall dynamic behaviour of intake and exhaust flows can be studied with one-dimensional unsteady fluid dynamic based tools. Flow within the cylinder is highly unsteady and three dimensional. A detailed multi-dimensional computational fluid dynamics (CFD) solver can be used to study flow, spray and combustion inside the cylinder using boundary conditions generated from the one-dimensional model.

The CFD codes solve the partial differential equations for conservation of mass, momentum, energy and species concentrations. To solve these equations, continuum domain is discretized in to finite volume cells. For in-cylinder transient simulations, solutions are marched in time with solutions at time t_{n+1} is calculated from the known solution at time t_n. The main components of these multidimensional engine flow models are the following [5]:

- The partial differential equations (Navier-Stokes equations) and models which describe the flow process.

- The discretisation procedures used to convert the differential equations to algebraic expressions which relates between discrete values of velocity, pressure, temperature etc. located on a mesh which conforms to the geometry of the combustion chamber.

- A solution algorithm to solve the algebraic equations.

- The computer codes to translate the algorithm into computer language and also provide interfaces for the input and output of information.

4.2   CFD Solver

In this study, in-cylinder analysis is performed using CONVERGE CFD software package [57]. CONVERGE is a general purpose CFD code for the calculation of
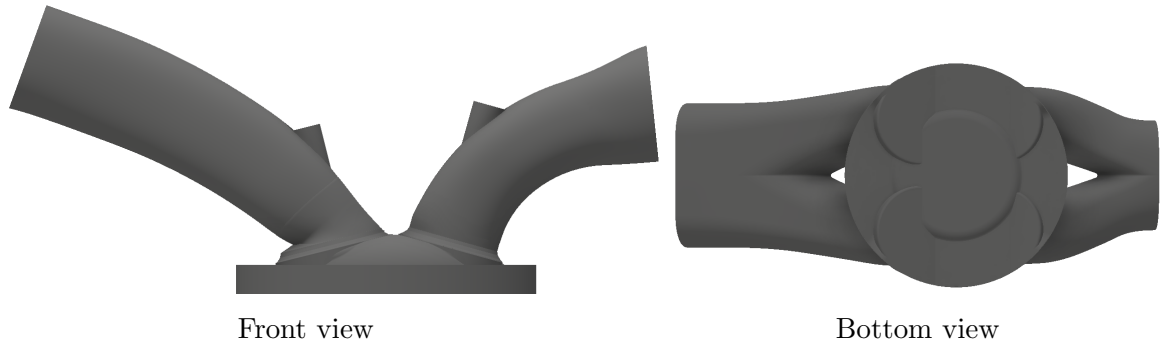
Figure 4.1: Geometry used for numerical engine modelling with piston at TDC.

three-dimensional, compressible, chemically reacting fluid flows in complex geometries with stationary or moving boundaries. This solver can handle an arbitrary number of species and chemical reactions, as well as transient liquid sprays and laminar or turbulent flows. A modified cut-cell Cartesian method is used that eliminates the need for the body fitted computational cells with the geometry of interest. This method allows for the use of simple orthogonal grids and completely automates the mesh generation process [58]. The geometry used for the calculation is shown in Fig. 4.1.

4.3 Governing equations

The Navier-stokes compressible equations for mass and momentum are follows:

Conservation of mass:

$$\frac{\partial \rho}{\partial t} + \frac{\partial \rho u_i}{\partial x_i} = S \tag{4.1}$$

Conservation of momentum:

$$\frac{\partial \rho u_i}{\partial t} + \frac{\partial \rho u_i u_j}{\partial x_j} = -\frac{\partial P}{\partial x_i} + \frac{\partial \sigma_{ij}}{\partial x_j} + S_i \tag{4.2}$$

In the above equations, u is the velocity, ρ is the density, S is the source term, P is pressure and σ_{ij} is the viscous stress tensor.

The viscous stress tensor, σ_{ij} is given by

$$\sigma_{ij} = \mu \left(\frac{\partial u_i}{\partial x_j} + \frac{\partial u_j}{\partial x_i} \right) - \frac{2}{3}\mu \left(\frac{\partial u_k}{\partial x_k}\delta_{ij} \right)$$

where μ is the dynamic viscosity, δ_{ij} is the Kronecker delta and takes a value of 1 if $i = j$ and 0 if $i \neq j$.

IC engine in-cylinder flows are compressible flows and an equation of state is required to couple density, pressure and temperature.

Equation of state:

$$\frac{P}{\rho} = \left(\frac{R}{M}\right) T \tag{4.3}$$

where R is the universal gas constant and M is the molecular weight.

To account for energy transfer inside the cylinder, compressible form of the energy equation is also to be solved.

Conservation of energy:

$$\frac{\partial \rho e}{\partial t} + \frac{\partial \rho e u_j}{\partial x_j} = -P\frac{\partial u_j}{\partial x_j} + \sigma_{ij}\frac{\partial u_i}{\partial x_j} + \frac{\partial}{\partial x_j}\left(K\frac{\partial T}{\partial x_j}\right) + \frac{\partial}{\partial x_j}\left(\rho D \Sigma_m h_m \frac{\partial Y_m}{\partial x_j}\right) + S \tag{4.4}$$

where Y_m is the mass fraction of species m, D is the mass diffusion coefficient, e is the specific internal energy, K is the conductivity and h_m is the species enthalpy. Molecular mass diffusion coefficient D is given by

$$D = \frac{\nu}{Sc} \tag{4.5}$$

where Sc is the Schmidt number. The pressure work term, $-P\frac{\partial u_j}{\partial x_j}$ in the Equation 4.4 accounts for compression and expansion work. The viscous dissipation term, $\sigma_{ij}\frac{\partial u_i}{\partial x_j}$, accounts for kinetic energy dissipating into heat.

The species diffusion term, $\frac{\partial}{\partial x_j}\left(\rho D \Sigma_m h_m \frac{\partial Y_m}{\partial x_j}\right)$, accounts for energy transport due to species diffusion. The term S accounts for user specified energy source like spark ignition.

To account for combustion chemistry, species transport equation is also required to be solved. The species transport equation solves for the mass fraction of all the species in the domain.

Conservation of species:

$$\frac{\partial \rho_m}{\partial t} + \frac{\partial \rho_m u_j}{\partial x_j} = \frac{\partial}{\partial x_j}\left(\rho D \frac{\partial Y_m}{\partial x_j}\right) + S_m \tag{4.6}$$

where S_m is the source term accounts for evaporation and combustion chemical reactions.

4.4 Turbulence modelling

Turbulence substantially increases the rate of mixing of momentum, energy and species. Turbulent flows show spatial and temporal variations over a range of scales with largest scale is decided by the combustion chamber dimensions and the lowest scale is decided by the viscous dissipative process. Most commonly used approach in engine flow simulation is Reynolds Averaged Navier Stokes (RANS) based turbulence models to account for the additional mixing from the unresolved length scales. Ideally, a CFD solver must contain a discretized domain that can resolve the smallest eddy length scales to capture enhanced mixing effects of turbulence in the simulation, this approach is known as Direct Numerical Solution (DNS). But it is computationally prohibitive to resolve all the length scales in an engine CFD simulation having high Reynolds number. Large Eddy Simulation (LES) is an intermediate approach where sufficiently refined grid is used to resolve energy containing large flow structures and only sub grid turbulence is modelled. LES is used more often now to study the cyclic variation as RANS based models are dissipative and fail to capture random perturbations associated with a turbulent flow field [59]. But all LES studies reported higher calculation time and expensive computing resources are required to do a multi-cycle simulation [60], [20]. LES can give good insight in to cylinder flow behaviour, but is computationally very expensive and is not a practical tool to evaluate a large number of design iterations. Due to these limitations, a RANS based linear eddy viscosity model is widely used to include turbulence effects in engine modelling.

4.4.1 RANS models

In Reynolds Averaged Navier Stokes equations, all variables including velocity field and thermodynamic state variables in the equations from 4.1 to 4.6 are replaced by suitably averaged quantities. For cyclic engine flows, time averaging is replaced by ensemble averaging as follows:

$$\underbrace{u_i}_{\text{instantaneous velocity}} = \underbrace{\overline{u_i}}_{\text{ensemble mean}} + \underbrace{u_i'}_{\text{fluctuating}} \tag{4.7}$$

As flow is compressed and expanded during engine cycle, mass-weighted averaging (Favre averaging) is used to make the averaged compressible flow equations look almost like the averaged equations for incompressible flows [5]. Favre average is defined for velocity as

$$\widetilde{u_i} = \frac{\overline{\rho u_i}}{\overline{\rho}} \tag{4.8}$$

On applying ensemble averaging, conservation of mass and momentum equations (4.1 and 4.2) changes to

$$\frac{\partial \overline{\rho}}{\partial t} + \frac{\partial \overline{\rho}\widetilde{u}_i}{\partial x_j} = 0 \tag{4.9}$$

$$\frac{\partial \overline{\rho}\widetilde{u}_i}{\partial t} + \frac{\partial \overline{\rho}\widetilde{u}_i\widetilde{u}_j}{\partial x_j} = -\frac{\partial \overline{P}}{\partial x_i} + \frac{\partial}{\partial x_j}\left[\mu\left(\frac{\partial \widetilde{u}_i}{\partial x_j} + \frac{\partial \widetilde{u}_j}{\partial x_i}\right) - \frac{2}{3}\mu\frac{\partial \widetilde{u}_k}{\partial x_k}\delta_{ij}\right] + \frac{\partial}{\partial x_j}(-\overline{\rho\widetilde{u'_i u'_j}}) \tag{4.10}$$

It is worth to mention that while eliminating the fluctuations in the transport equations by doing averaging, contributions from cyclic flow variations present in an engine flow field also get minimised. The momentum equation 4.10 has an additional term, $-\overline{\rho\widetilde{u'_i u'_j}}$ called the Reynolds stresses (τ_{ij}) that accounts for the effects of turbulence. The Reynolds stress term must be modelled with additional equations and solved along with other transport equations. The most widely used turbulence model is the $k-\varepsilon$ model [61].

$k-\varepsilon$ model

The $k-\varepsilon$ model assumes a Newtonian relationship between the turbulent stresses and mean strain rates and calculates artificial turbulent viscosity using local turbulent kinetic energy, k and dissipation rate, ε. Different formulations of $k-\varepsilon$ turbulence model are developed by researchers to suit different flow conditions [61]. Based on previous numerical studies on IC engine simulation, renormalization group (RNG) $k-\varepsilon$ model is used for this study [62],[44].

For RNG $k-\varepsilon$ model, the modelled Reynolds stress is given by

$$\tau_{ij} = -\overline{\rho\widetilde{u'_i u'_j}} = 2\mu_t S_{ij} - \frac{2}{3}\delta_{ij}\left(\rho k + \mu_t\frac{\partial \widetilde{u}_i}{\partial x_i}\right) \tag{4.11}$$

The turbulent kinetic energy, k is defined as

$$k = \overline{u'_i u'_i}/2 \tag{4.12}$$

The turbulent viscosity, μ_t is defined as

$$\mu_t = C_\mu \rho \frac{k^2}{\varepsilon} \tag{4.13}$$

where C_μ is a constant and can be tuned for a particular flow. The mean strain rate tensor, S_{ij} is given by

$$S_{ij} = \frac{1}{2}\left(\frac{\partial \widetilde{u}_i}{\partial x_j} + \frac{\partial \widetilde{u}_j}{\partial x_i}\right) \tag{4.14}$$

$k-\varepsilon$ models require two additional transport equations to solve in order to obtain turbulent viscosity as per Eq: 4.13. One equation is for turbulent kinetic energy,

k and the other one is for dissipation of turbulent kinetic energy, ε. The turbulent kinetic energy transport equation is derived by manipulation of RANS Navier-stokes momentum equation and is given by

$$\frac{\partial \rho k}{\partial t} + \frac{\partial \rho u_i k}{\partial x_i} = \tau_{ij}\frac{\partial u_i}{\partial x_j} + \frac{\partial}{\partial x_j}\frac{\mu + \mu_t}{Pr_k}\frac{\partial k}{\partial x_j} - \rho\varepsilon + \frac{C_s}{1.5}S_s \tag{4.15}$$

A modelled transport equation for the dissipation of turbulent kinetic energy, ε is usually devised by via an empirical approach [63]. The ε transport equation used by CONVERGE CFD solver is given by

$$\frac{\partial \rho \epsilon}{\partial t} + \frac{\partial (\rho u_i \varepsilon)}{\partial x_i} = \frac{\partial}{\partial x_j}\left(\frac{\mu + \mu_t}{Pr_\varepsilon}\frac{\partial \varepsilon}{\partial x_j}\right) + C_{\varepsilon 3}\rho\varepsilon\frac{\partial u_i}{\partial x_i} + \left(C_{\varepsilon 1}\frac{\partial u_i}{\partial x_j}\tau_{ij} - C_{\varepsilon 2}\rho\varepsilon + C_s S_s\right)\frac{\varepsilon}{k} + S - \rho R \tag{4.16}$$

where S is the user defined source term and S_s is the source term to account for interactions with spray discrete phase. The $C_{\varepsilon 1}$, $C_{\varepsilon 2}$ and $C_{\varepsilon 3}$ are model constants that account for compression and expansion [58]. For RNG $k-\varepsilon$ model, The term R is given by

$$R = \frac{C_\mu \eta^3(1 - \eta/\eta_0)\varepsilon^2}{(1 + \beta\eta^3)k} \tag{4.17}$$

and the expression for η is

$$\eta = \frac{k}{\varepsilon}|S_{ij}| = \frac{k}{\varepsilon}\sqrt{2S_{ij}S_{ij}} \tag{4.18}$$

When a turbulence model is used, the conductivity K in the Eq:4.4 is replaced by the turbulent conductivity, K_t

$$K_t = K + c_p\frac{\mu_t}{Pr_t}$$

where Pr_t is the turbulent Prandtl number and μ_t is the turbulent viscosity. The expression for the turbulent Prandtl number used in the solver is

$$Pr_t = \frac{c_p\mu_t}{K_t}$$

where c_p is the specific heat.

Also, molecular diffusion coefficient D in the Eq:4.4 and Eq:4.6 is replaced by turbulent mass diffusion coefficient, D_t and is defined as

$$D_t = \frac{\nu_t}{Sc_t}$$

where Sc_t is the turbulent Schmidt number.

4.4.2 Near wall modelling

With a turbulent flow field, the velocity and temperature boundary layers inside the cylinder is too thin to be resolved with an adequately refined mesh. However, the boundary layers are significant to determine wall shear stress and heat transfer to the cylinder walls, which are essential boundary conditions for the numerical simulation and also are of practical importance, especially for predicting the influence of piston shape on tumble level and heat rejection [5].

As it is difficult to refine the boundary layer, near wall flow behaviour is modelled using wall functions which helps in placing first computational cell centre outside the viscous sub layer and in fully turbulent region, where velocity variation satisfies the log-law [64]:

$$U^+ = \frac{1}{k}log(Ey^+) \tag{4.19}$$

where k and E are usually taken as 0.41 and 9 respectively, and

$$U^+ = U/(\tau_\omega/\rho)^{1/2} \tag{4.20}$$

$$y^+ = y(\tau_\omega/\rho)^{1/2}/\nu \tag{4.21}$$

τ_ω is the wall shear stress. Near wall cell size is chosen ensuring non dimensional wall distance, y^+ is greater than 30, which ensures the first cell centre is in fully turbulent boundary layer. Temperature also shows similar variation across the boundary layer due its dependency on flow field and a similar law-of-the-wall expression developed by O'Rourke and Amsden [65] is used to calculate temperature variation near the boundary.

The calculated flow filed is shown in the Fig. 4.2. The influence of valve seat masking on tumble generation and active tumble flow field at combustion start is clearly visible on predicted flow results.

4.5 Combustion modelling

CONVERGE provides an option of detailed chemistry solver called SAGE detailed chemical kinetics solver [66] to calculate combustion. The SAGE solver models detailed chemical kinetics via a set of CHEMKIN [67] formatted chemical reaction mechanism files. A chemical reaction mechanism is a set of elementary reactions that construct an overall chemical reaction. The skeletal mechanism used for this study is built by merging mechanism of toluene reference fuels by Liu et al. [68] and an ethanol mechanism by Marinov et al.[69] and the mechanism is given in
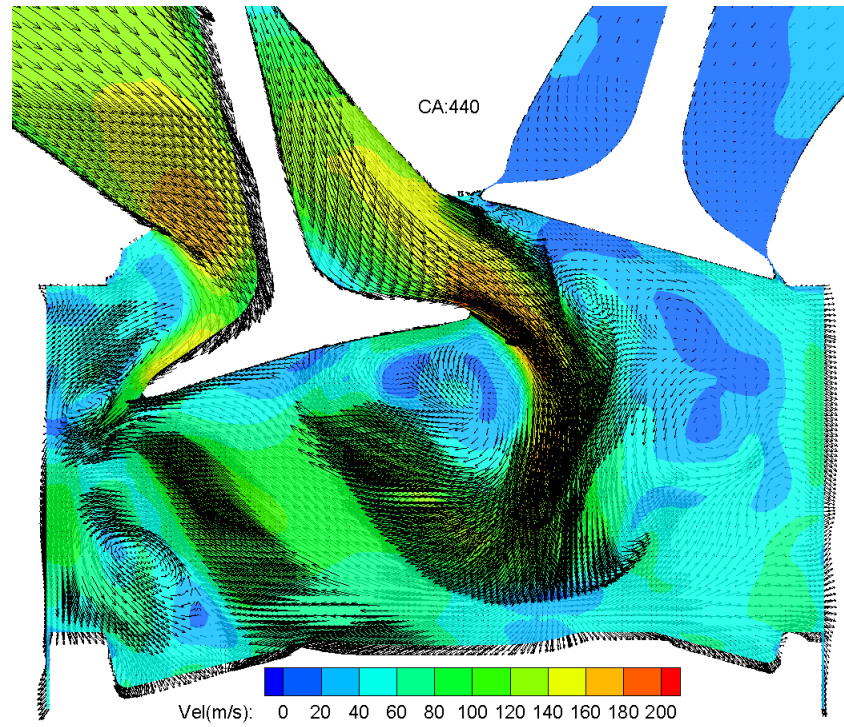
(a) At maximum intake valve lift.
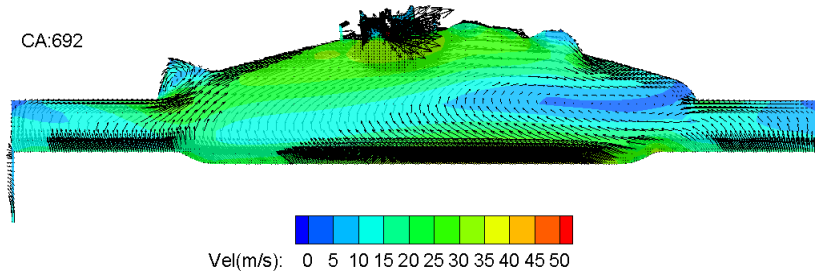
(b) At the combustion start on mid cylinder plane

Figure 4.2: Velocity field at 7000 rpm.

Appendix:A. SAGE solver calculates the reaction rates for each elementary reaction while the CFD solver solves the transport equations. The steps through which SAGE solver calculates combustion are explained below [58].

A multi-step chemical reaction can be represented in the following form [70]:

$$\sum_{m=1}^{M} \nu'_{m,r} \chi_m \Leftrightarrow \sum_{m=1}^{M} \nu''_{m,r} \chi_m \quad \text{for r=1,2,....R} \tag{4.22}$$

where $\nu'_{m,r}$ and $\nu''_{m,r}$ are the stoichiometric coefficients for the reactants and products for species m and reaction r. R is the total number of reactions and χ_m is the chemical symbol for species m.

The net production rate of species m is given by

$$\dot{\omega}_m = \sum_{r=1}^{R} \nu_{m,r} q_r \quad \text{for m=1,2,...M} \tag{4.23}$$

where M is the total number of species and

$$\nu_{m,r} = \nu''_{m,r} - \nu'_{m,r} \tag{4.24}$$

The rate of progress of parameter q_r for the rth reaction is

$$q_r = k_{fr} \prod_{m=1}^{M} [X_m]^{\nu'_{m,r}} - k_{rr} \prod_{m=1}^{M} [X_m]^{\nu''_{m,r}} \tag{4.25}$$

where $[X_m]$ is the molar concentration of species m, and k_{fr} and k_{rr} are the forward and reverse rate coefficients for reaction r. In SAGE solver, forward rate coefficient is expressed by the Arrhenius form as

$$k_{fr} = A_r T^{b_r} e^{(-E_r/R_u T)} \tag{4.26}$$

Where A_r is the pre exponential factor, b_r is the temperature exponent and E_r is the activation energy. These three values for each reactions are provided in the skeletal mechanism file discussed above. R_u is the universal gas constant.

The reverse rate coefficient is calculated as

$$k_{rr} = \frac{k_{fr}}{K_{cr}} \tag{4.27}$$

The equilibrium coefficient K_{cr} is given by

$$K_{cr} = K_{pr} \left(\frac{P_{atm}}{RT} \right)^{\sum_{m=1}^{M} \nu_{mr}} \tag{4.28}$$

where P_{atm} is the atmospheric pressure, R is the gas constant, and T is the temperature. the equilibrium constant K_{pr} is given by

$$K_{pr} = exp \left(\frac{\Delta S_r^0}{R} - \frac{\Delta H_r^0}{RT} \right) \tag{4.29}$$

The Δ refers to the change that occurs when reactants completely converts to products in the rth reaction, where

$$\frac{\Delta S_r^0}{R} = \sum_{m=1}^{M} \nu_{m,r} \frac{S_m^0}{R} \tag{4.30}$$

and

$$\frac{\Delta H_r^0}{RT} = \sum_{m=1}^{M} \nu_{m,r} \frac{H_m^0}{RT} \qquad (4.31)$$

where S and H denote entropy and enthalpy respectively.

With the above information, the governing equations for mass and energy is solved for each computational cell,

Conservation of mass:

$$\frac{d[X_m]}{dt} = \dot{\omega}_m \qquad (4.32)$$

Conservation of momentum for constant volume combustion:

$$\frac{dT}{dt} = \frac{V\frac{dP}{dt} - \sum_m \left(\bar{h}_m \dot{\omega}_m \right)}{\sum_m \left([X_m] \bar{c}_{p,m} \right)} \qquad (4.33)$$

where V is volume, T is temperature and $\bar{h}_m$ and $\bar{c}_{p,m}$ are the molar specific enthalpy and molar constant pressure specific heat of species m, respectively.

The SAGE solver equations are solved at each time step and the species updated appropriately. The temperature obtained from the Eq:4.33 is used only to update the rate coefficients as SAGE solver is solving the system of rate equations and is not used to update the cell temperature. Once, the detailed chemistry calculation has converged, the cell temperature is updated for solving other transport equations. Fig. 4.3 and Fig. 4.4 shows predicted flame development for the base spark ignition engine.

(a) 12º before TDC   (b) 2º before TDC   (c) 10º After TDC
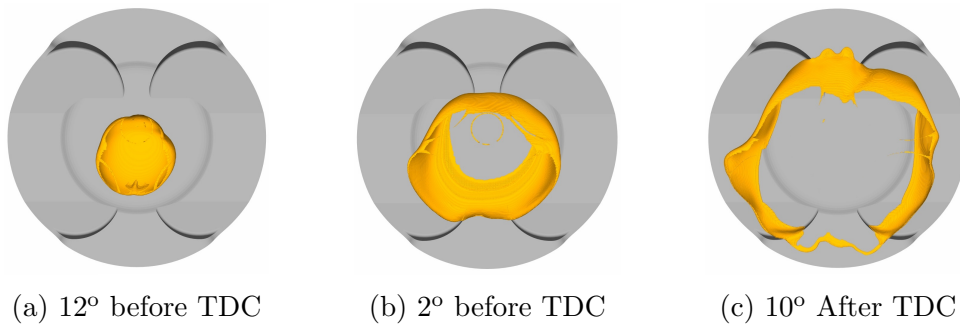
Figure 4.3: Progress of flame development at 7000 RPM. Temperature iso-surface of 1700 K

(a) 12º before TDC (b) 2º before TDC (c) 10º After TDC
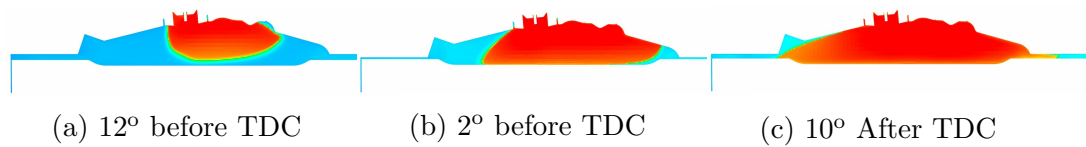
Figure 4.4: Temperature variation during combustion at 7000 rpm.

4.6 Fuel spray modelling

To calculate spray, solver introduces drop parcels into the domain at the injector location as shown in Fig. 4.5. These parcels are entered in to the fluid domain at a
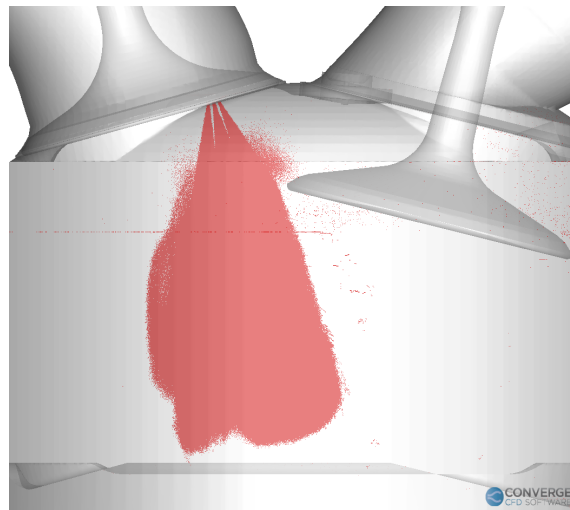
Figure 4.5: Spray parcels

rate matching to injection duration, injected mass and injection pressure, measured in the engine test. Parcels represent a group of identical drops with same physical properties including radius, velocity and temperature, and are used to statistically represent the entire spray field. With this parcel assumption, solver avoids the need of solving all drops in the field and significantly reduces the computational time of simulation involving spray. The gasoline fuel used for the experiment is represented by iso-octane with 20.4% ethanol by volume in simulation.

Spray droplets or parcels are subject to several processes from the time of injection until the time of vaporisation. The Table.4.1 lists different processes involved in spray formation and corresponding modelling options used with the CFD solver [58]. Separate validation was not done for spray study due to the absence of an experimental set-up and basic models with minimum tuning coefficients are used in this study. The CFD model predicted fuel stratification at the start of combustion as shown in Fig. 4.6.

Spray model process	Modelling option used
Liquid injection	Blob injection model
Spray breakup	modified KH-RT models
Drop drag	Dynamic drag model
Collision model	O'Rourke model
Collision outcomes model	O'Rourke model
Drop turbulent dispersion	O'Rourke
Drop-wall interaction	Rebound/slide model
Evaporation model	Multi-component vaporisation

Table 4.1: Spray processes and modelling options considered in the solver.
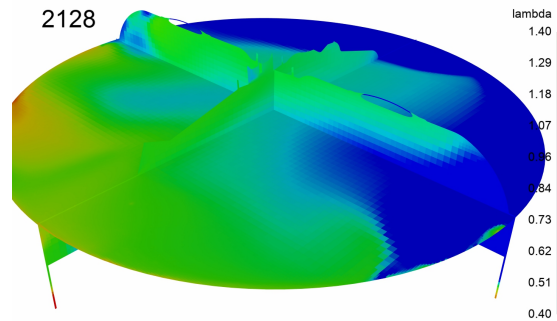
Figure 4.6: Lambda variation across the combustion chamber at the combustion start

4.7 Other solver settings

The single cylinder geometry shown in Fig. 4.1 was discretized with a base grid size of 2 mm in all directions and grid refinements are made on the top of that. Fixed grid refinements are done on regions of interest such as valve seats, spark plug tip, piston surface and spray cone. Also, for regions where sharp gradient exists and cannot be determined before hand, such as flame front, an Adaptive Mesh Refinement (AMR) strategy was used. AMR increases grid resolution in places where the flow is under resolved, determined based on the gradients in velocity and temperature. The smallest cell size used for the calculation was 0.125 mm, which is near the spark plug during combustion start. For a typical engine simulation with a RANS based turbulence model, it was identified that increasing mesh resolution beyond 0.1 mm would not improve the accuracy as there are no more scales to resolve [62]. Various mesh refinement methods used are visible in Fig. 4.7. Maximum number of cells reached 2.5 million during combustion, when high velocity and temperature gradients present inside the combustion chamber. Second order central difference schemes are used for spatial discretization of both convection and diffusion terms in all transport equations.

One crucial problem in solving Navier Stokes equation is that continuity equation does not explicitly contain pressure term and an iterative procedure was used

Figure 4.7: Mesh refinement during flame progress. fixed mesh refinement near the spark plug and near combustion chamber surface. Adaptive mesh refinement is present along the flame front.

to adjust the pressure field in order to ensure that the resulting velocity field does satisfy continuity. Such schemes are referred as Pressure Correction schemes and a modified Pressure Implicit with Spli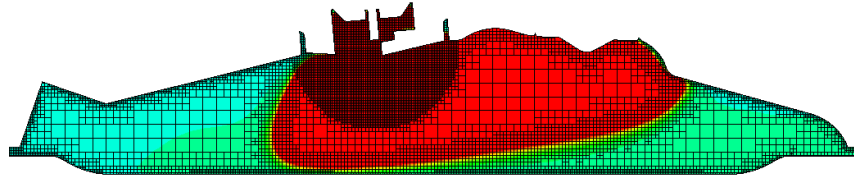tting of Operator (PISO) method [71] was used for this study. CONVERGE CFD uses collocated grids with all transported quantities are stored at the cell centre. A collocated grid arrangement can result in decoupling of pressure and velocity terms, produces fluctuations in the pressure and velocity solution that appear in a checkerboard pattern. Rhie-Chaw interpolation scheme was implemented to prevent this undesirable checkerboarding [58].

The first order implicit Euler scheme was used for temporal discretization as it helps in using a larger time-step, compared to explicit Euler scheme. Dynamic time step was employed with the value was chosen based on Courant–Friedrichs–Lewy (CFL) condition, given as

$$CFL = u\frac{\Delta t}{\Delta x} \tag{4.34}$$

Δt is time step and Δx is the cell size. CFL value was limited to 1 for accuracy. with this criteria, depending on AMR or fixed periodic grid refinement, time step varies during the calculation.

4.8   Boundary conditions and initial conditions

The accuracy of boundary condition is significant in predicting correct in-cylinder flow, mixing and combustion performance. Both inlet and outlet pressure and temperature boundary conditions are obtained from a correlated 1D engine performance model, developed in GT-Power software[1]. Inlet total pressure and outlet static pressure used for the CFD model are shown in Fig. 4.8. Pressure pulsations in intake and exhaust ports are included in pressure boundary condition, which helps in predicting accurate cylinder trapped mass. Same approach is also used for defining temperature boundary conditions.

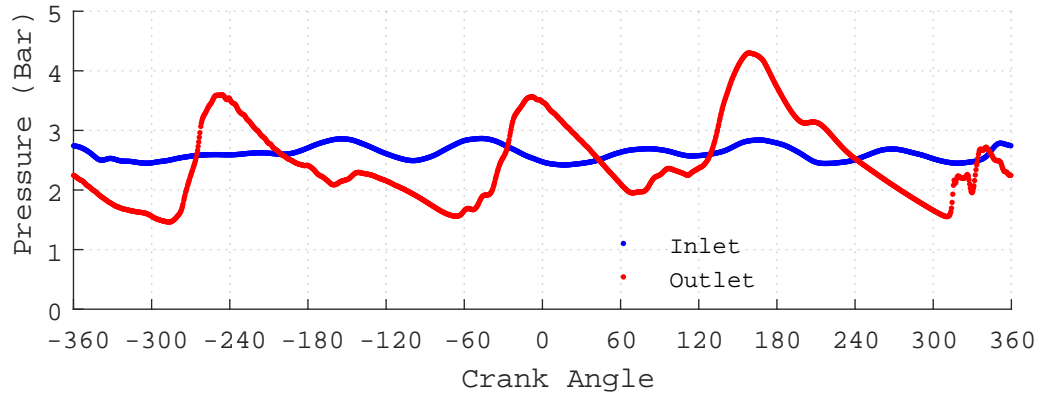[1]Work by research colleague, Priyadarshi Sahu

Figure 4.8: Inlet (total) and outlet (static) pressure boundary conditions taken from 1D engine model, 7000 rpm and fuel flow rate of 17.5 kg-hr

Initial conditions are also taken from 1D engine model. But 1D engine model provides a single value for solver variables in a flow domain and it results in defining a uniform value of solver variable in a domain, for example: velocity inside the cylinder. This assumption is far from the reality and hence result from first cycle is highly influenced by this uniform initial conditions assumption. So first cycle result is neglected and result from second cycle onwards used for the analysis.

4.9   Engine model validation

The engine CFD model was developed for 7000 rpm and for a fuel flow rate of 17.5 kg/hr. Other key engine design specifications are provided in Table. 6.1 on Chapter 6. The base engine mostly runs at full load from 6000 to 8000 rpm and hence 7000 rpm was chosen as the speed to develop the numerical model and to do further design iterations. The fuel flow rate was decided based on the maximum fuel flow rate of the base V6 engine. A well correlated CFD model is expected to show the exact behaviour of pressure curves as observed in the test data (Fig. 4.9), reproducing all individual measured pressure cycles. Previous studies identified that LES based simulations can quantitatively predict the cyclic variation [60], [20]. A RANS based CFD model tends to be more diffusive and does not achieve a quantitative correlation to cyclic variation and pressure curves stay close to the average pressure curve. However, previous studies have shown that cyclic variation is visible in engine combustion with RANS turbulence model if the scales of the flow that are causing the cyclic variation are not small enough to be destroyed by the RANS turbulence viscosity [72], [73]. Scarcelli et al. concluded that with a well refined mesh, low numerical viscosity can be achieved and RANS based engine model can show cyclic variability which comes from the variability of large flow structures from cycle to cycle [74]. As discussed in §2.3, changes in mean flow field and its interaction
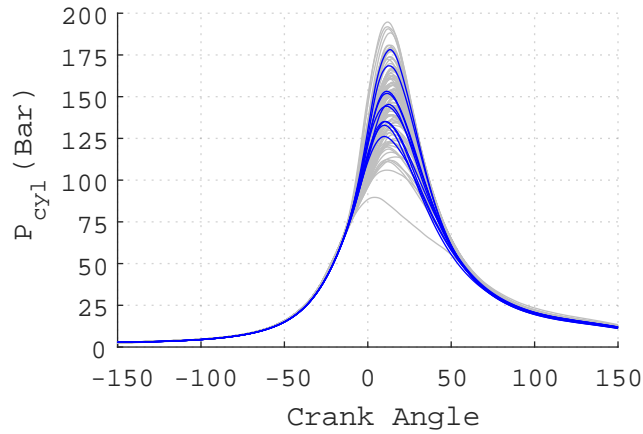
Figure 4.9: Multi cycle CFD results and correlation to test data. Test data is shown in light grey colour. 7000 rpm and fuel flow rate of 17.5 kg-hr

with spray are the most influential factors causing cyclic variations in a GDI engine. The base motor-sport engine was developed with high intake valve seat masking to produce tumble motion during intake to aid turbulent combustion. Also, the base engine operates at higher speeds, causing high flow velocities inside the cylinder during the intake and compression strokes. Thus, any changes inside the cylinder during intake valve opening, contributed from the previous cycle combustion event can be amplified and results in different flow field, from cycle to cycle. So despite using a RANS model, it is not necessary to get an ensemble averaged result after a few cycles. 10 continuous cycles of simulated cylinder pressure data for the base spark ignition engine was compared with 100 continues measured cycles, as shown in Fig. 4.9.

First cycle simulated data was not considered to avoid the influence of initialization variables used. It can be seen that pressure curves up to the combustion start is repetitive, but they start to deviate from the average pressure curve from the combustion start, with reduced peak pressure variation compared to the measurement data. The factors causing these variations in simulated pressure curves were identified as varying mean flow field and mixture state near the spark plug tip, resulting in different ignition delay and burn duration, from cycle to cycle. Comparison of average pressure curve for the same 10 simulated cycles with the measured average data is shown in Fig. 4.10.

The results show good correlation and numerical model is predictive enough for studying various design iterations that influence combustion. Small discrepancies between measured and predicted data could be due to mismatch of combustion phasing as test ignition timing was used in the simulation and there could be mismatch between start of ignition inside the cylinder and ignition signal input by the ECU. Also, iso-octane with 20.4% ethanol by volume was used as the fuel composites,
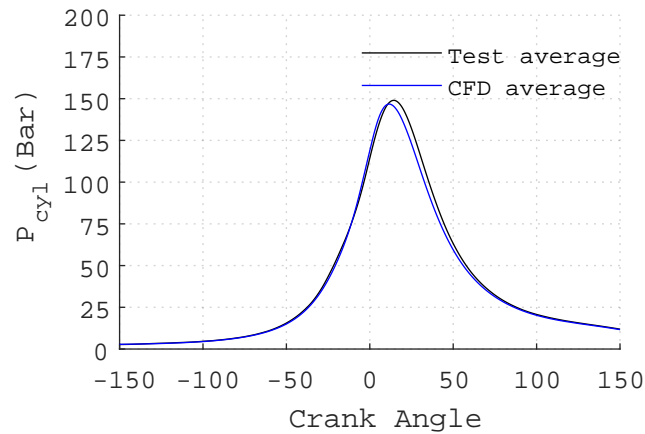
Figure 4.10: Correlation of test and CFD results: Average of 10 simulated cycles and 100 test cycles. 7000 rpm and fuel flow rate of 17.5 kg-hr

based on the data provided by the fuel supplier. But there are differences in actual properties including flame speed and calorific value between fuel surrogate used in the simulation and gasoline tested. The measured lower calorific value of the fuel is 39.85 MJ/Kg and fuel surrogate used for the calculation has lower calorific value of 40.33 MJ/kg. There are more refined approaches where more complex fuel blends can be used to match the fuel properties including calorific value and octane number to the test fuel [75], but increases computational time. It is key to note that lower calorific value is not a direct input to the simulation when the detailed chemistry solver is used.

With the SAGE detailed chemistry approach, there is no need of separate knock modelling as solver is able to predict knocking combustion when favourable conditions exist inside the combustion chamber. The solver was able to predict the exact location of the knock as shown in Fig. 4.11. For the base SI engine, as the en-
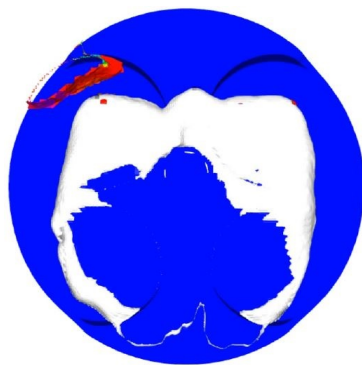
(a) Spark flame (white) and knock flame (red)   (b) Melted section of valve pockets

Figure 4.11: Knock prediction correlation

gine mostly operates at full-load and knock limited operating points, knock resulted damages are often visible on the pistons. The knock caused piston damage was

observed on the intake valve pockets on the piston and the CFD model shows the exact location as the knock initiation site. The simulation was run with advanced ignition phasing compared to the test data, to generate a knocking cycle. Due to active tumble flow field exists during combustion start, flame development is shifted towards the exhaust side as shown in Fig. 4.3, and results in intake side charge burns towards the end and hence, knocking initiates on the intake side.

With the developed CFD model, a simulation study was conducted to investigate knock events observed in a transient engine operating condition. During this transient engine running, both intake and exhaust back pressure was momentarily increased by closing exhaust waste-gate valve and ignition angle was advanced to improve the engine response. The simulation was conducted for 20 continues cycles with measured inlet and exhaust pressure boundary conditions and actual ignition angle for the whole duration of transient operation. The CFD model was able to predict the knocking cycle and also predicted the knock onset at the same crank angle as shown in Fig. 4.12. Pressure oscillations are not visible in CFD prediction
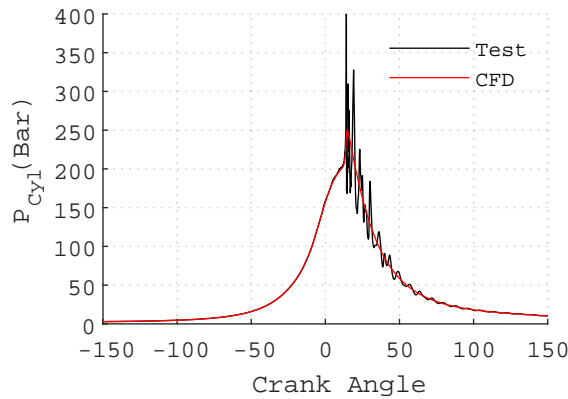
Figure 4.12: Test correlation: CFD (total volume average) vs measured single knock cycle

as total volume averaged value is used for the CFD data, where as a pressure sensor measure local pressure value. Pressure sensor was placed on the squish land on the intake side and sufficient cells are not available on squish-land in the CFD model when the piston is near TDC and makes it difficult to show local pressure values.

Chapter 5

Pre-chamber Design

Contents

5.1 Introduction

This chapter explains how the pre-chamber design was developed with the objective of reducing burn duration. As the pre-chamber is mounted on the cylinder head, design iterations were restricted to keep the modifications required on the cylinder head minimum. As cylinder head water jacket is a part of cast feature, any design changes that affect water jacket design were expensive to implement and would require separate validation due to its influence on heat rejection and knock resistance of the given cylinder. Moreover, the base spark plug location later identified as the suitable location for the pre-chamber mounting, also helped in keeping the cylinder head design the same. Thus, as a first step, it was decided to use the same spark plug mounting feature, which is an M12 thread as the mounting feature for the pre-chamber and other pre-chamber design parameters were finalised with this consideration. The different pre-chamber designs were made using the CAD software,

AUTODESK INVENTOR and then exported to CONVERGE CFD for numerical evaluation.

5.2   Parametric study for pre-chamber design optimisation

The base engine CFD model was modified to include a pre-chamber design and a parametric study was conducted to decide the design features of the pre-chamber including position of the pre-chamber within the combustion chamber, pre-chamber volume, number of nozzles, nozzle diameter, nozzle entry angle and nozzle orientation. Simulations were conducted for designs with different combinations of all above variables. For each design, simulation were performed for three consecutive cycles. First cycle result was omitted to eliminate the influence of initialization variables used in the CFD case set up and the average of the last two cycles was considered for the discussion to account for cycle to cycle variation, discussed in §4.9. The grid size of 0.125 mm was used inside the pre-chamber as well as in the areas within the combustion chamber where the jet pass through before diffusion. The grid size inside the combustion chamber during the jet ejection from the pre-chamber is shown in Fig. 5.1. The grid size of 0.125 mm was decided because it
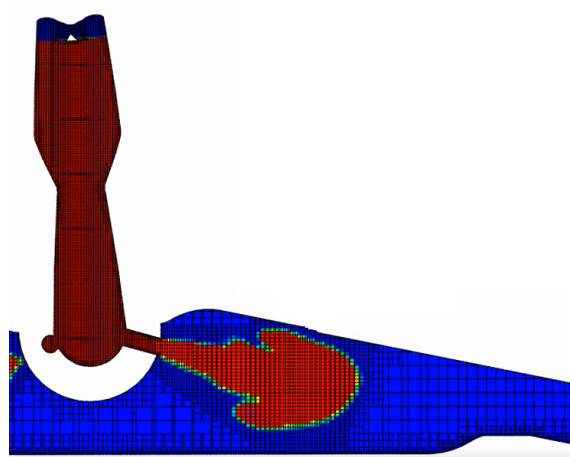
Figure 5.1: Mesh distribution during pre-chamber jet ejection from the pre-chamber.

is the smallest grid possible with an acceptable computation time and it may be possible to use a coarser mesh and require a separate study on grid sensitivity. It is worth to mention that there was no pre-chamber test results available to check the correlation. The maximum number of cells increased from 2.5 million of the base engine model to 3.5 million with this additional grid refinement for the pre-chamber and calculation time doubled compared to base engine model, reaching 80 hours for one four-stroke cycle. The finalised pre-chamber design is shown at the end of this chapter in Fig. 5.21 and following sections will discuss how all design variables are

decided with the help of this CFD model.

Most of the pre-chamber designs evaluated show a substantial reduction in ignition delay (Ignition time to MFB10%) and burn duration (MFB10-90%) over the base spark plug ignited combustion. As the base spark plug engine was already operating at knock limited points, any reduction in ignition delay could see very high cylinder pressure due to combustion phasing advance and resultant heavy knocking. So, this much reduced ignition delay and burn duration results in heavy knocking if the ignition angle of the base spark plug model was used. Hence, all the pre-chamber simulations were done with a 10 deg CA ignition retard from the base ignition angle. The flame development inside the pre-chamber and progress in the combustion chamber are shown in Fig. 5.2. The multiple jets from the pre-chamber are acting as multiple ignition sources inside the main combustion chamber, thus reducing the burn duration compared to spark ignited combustion. Some cases discussed in the following sections show burn duration angle less than 25°, as a result of knocking combustion from a shorter ignition delay and much reduced burn duration. These pre-chamber designs require further ignition retard for actual implementation. Following sections discuss the influence of each design variable in detail.

5.2.1 Pre-chamber position

The base motor-sport sport engine operates at higher engine speeds ($> 6000\,RPM$) and thus time available for fuel injection and mixture formation is less. The direct injection starts at 300 deg CA before TDC$_{\text{firing}}$ and lasts for 133 deg CA, largely overlapping with intake valve opening window. Higher injection pressure (325 Bar) is utilized to complete fuel injection in less time available and also to improve mixing, but still results in a stratified mixture state as shown in Fig. 5.3. Mixture distribution at ignition time (18° CA BTDC$_{\text{firing}}$) with pre-chamber is shown in Fig. 5.4. For the base SI engine, the spark plug is positioned on the intake side of the combustion chamber to benefit from the presence of rich mixture on the intake side. Placing the spark plug on the intake side can increase the knock occurrence as the exhaust side of the combustion chamber tends to be at a higher temperature and flame front from the spark plug could reach the exhaust side late with the cylinder pressure raised substantially from the combustion already completed. But with the base SI engine, the presence of active tumble flow field during the combustion start (Fig. 5.5) helps in convecting flame towards the exhaust side, which allows the air-fuel charge on the exhaust side burns first, as shown in Fig. 5.6. To benefit from the rich mixture on the intake side, the pre-chamber was also placed on the base spark plug location. Since the pre-chamber ignited flame development inside the main chamber is uniform from the pre-chamber, the flame development was found to be shifted towards
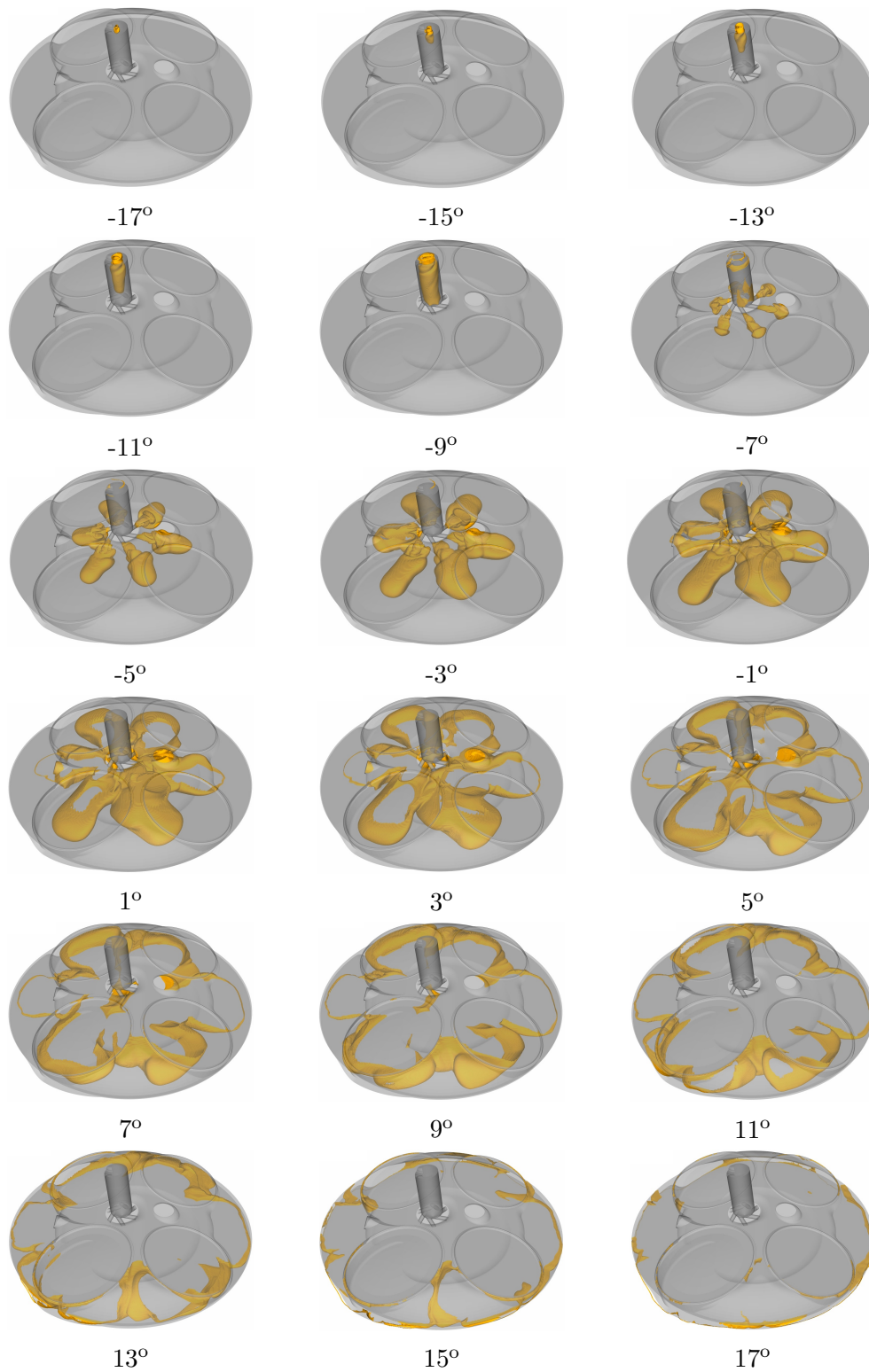
Figure 5.2: Pre-chamber initiated flame development inside the combustion chamber. CA with respect to $\text{TDC}_{\text{firing}}$ is given.

the intake side because of the pre-chamber location (Fig. 5.7). Pre-chamber ignited flame was less convected by the main combustion chamber flow field. Such a flame development results in the mixture present on the exhaust side burn towards the end and has higher chance for knock, as shown in Fig. 5.8.
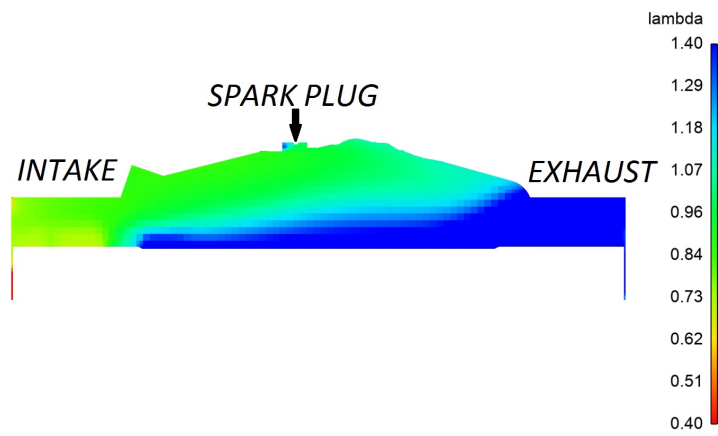
Figure 5.3: Relative AFR on a mid cylinder plane normal to crank axis at combustion start with spark ignition (28º CA BTDC$_{\text{firing}}$).
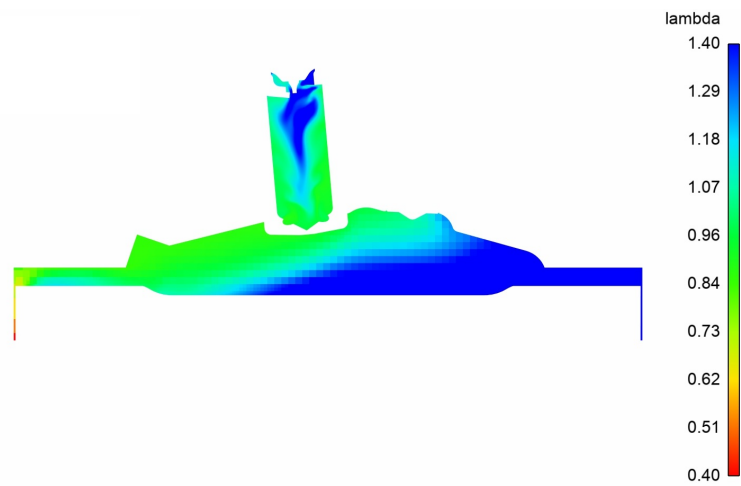
Figure 5.4: Relative AFR on a mid cylinder plane normal to crank axis at combustion start with pre-chamber (18º CA BTDC$_{\text{firing}}$).
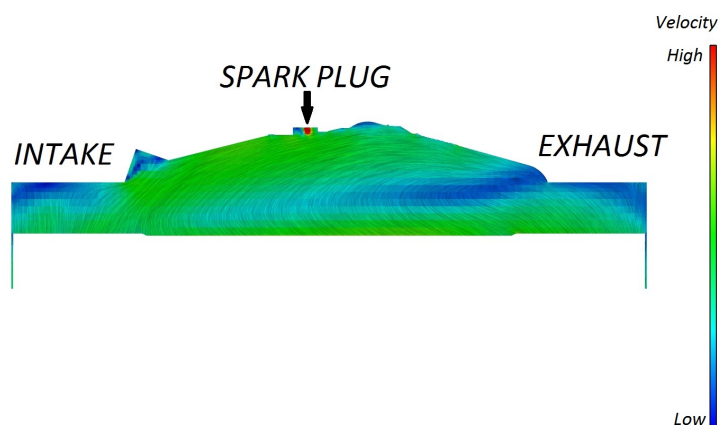
Figure 5.5: Line Integral Convolution (LIC) visualisation of flow field on a mid cylinder plane normal to crank axis at combustion start.
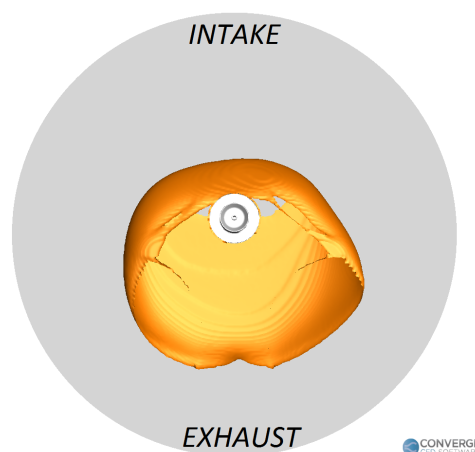
Figure 5.6: Spark plug ignited flame development at TDC (Temperature iso-surface = 1700K).
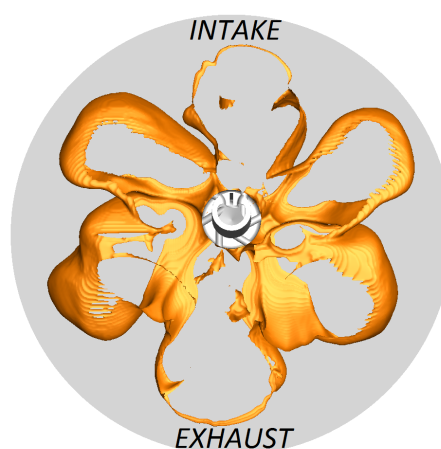
Figure 5.7: Pre-chamber ignited flame development at TDC (Temperature iso-surface = 1700K).
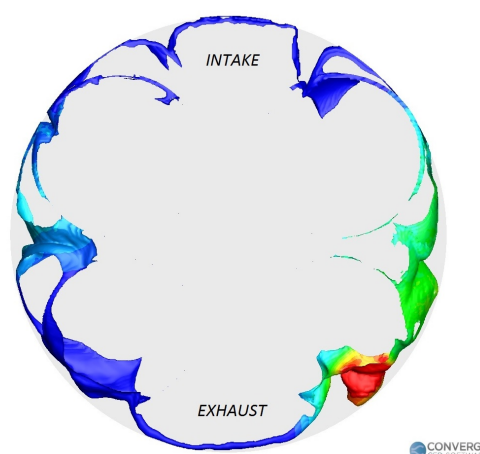
Figure 5.8: Flame state at knock onset (Temperature iso-surface of 1700K, coloured by the pressure difference between mean cylinder pressure and local pressure values). Red coloured area indicates knock initiation site.

5.2.2 Pre-chamber volume

Pre-chamber volume from 0.5 cc to 1.5 cc was evaluated and it was observed that with the increasing pre-chamber volume, burn duration was reduced (Fig. 5.9). This
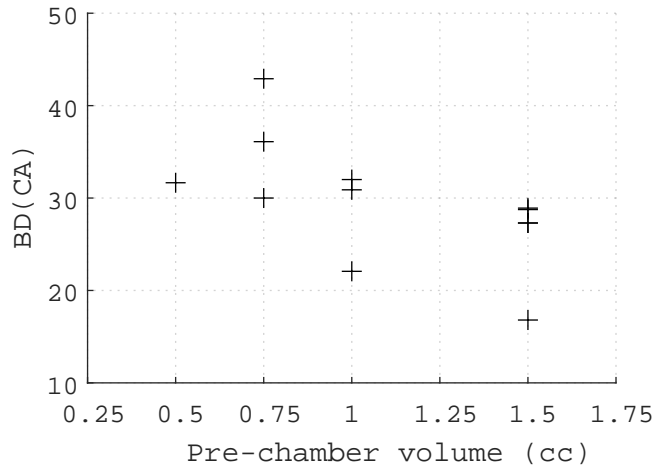
Figure 5.9: Burn duration (MFB10-90%) vs pre-chamber volume

was caused by higher charge mass inside the pre-chamber volume, resulting in higher pre-chamber pressure and resultant increased jet penetration inside the main chamber. But as the pre-chamber volume was increased, the mixture state was observed to be leaner and also have higher variations from case to case (Fig. 5.10) and also cycle to cycle. After combustion completion and during exhaust stroke, pre-chamber
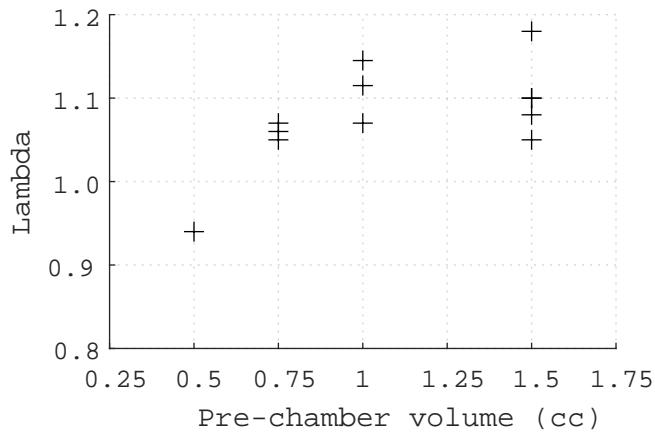
Figure 5.10: Relative AFR (lambda) vs pre-chamber volume

is filled with burned gases and scavenging of this residual gases only happens when the main chamber pressure is higher than pre-chamber pressure. Main chamber and pre-chamber pressure comparison during compression stage is shown in Fig. 5.11. Pre-chamber pressure is lower than main chamber pressure from 75 to 15 deg CA BTDC, during which fresh air-fuel charge enters the pre-chamber. Within this limited time, it is easier to fill a small volume pre-chamber with fresh charge than a large volume pre-chamber. Lean mixture state inside the pre-chamber is not ideal for the pre-chamber performance as observed by other researchers discussed in the Chapter 3. Simulation results also show that pre-chamber has around 5% exhaust residuals compared to 2% inside the main chamber, showing difficulty in scavenging and significance of maintaining rich mixture inside the pre-chamber. The variation
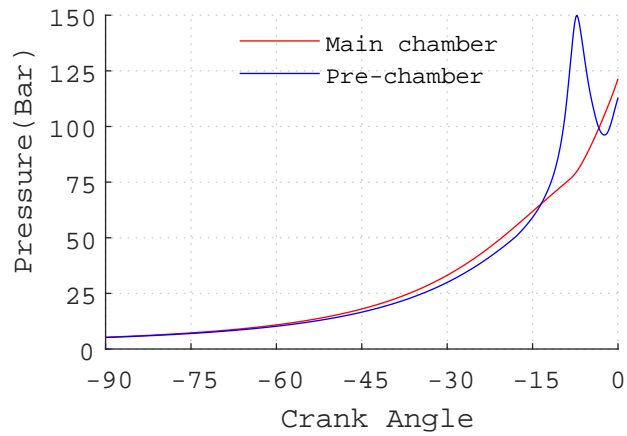
Figure 5.11: Comparison of main chamber and pre-chamber pressure

in combustion start angle for the main combustion chamber with respect to pre-chamber volume is shown in Fig. 5.12.
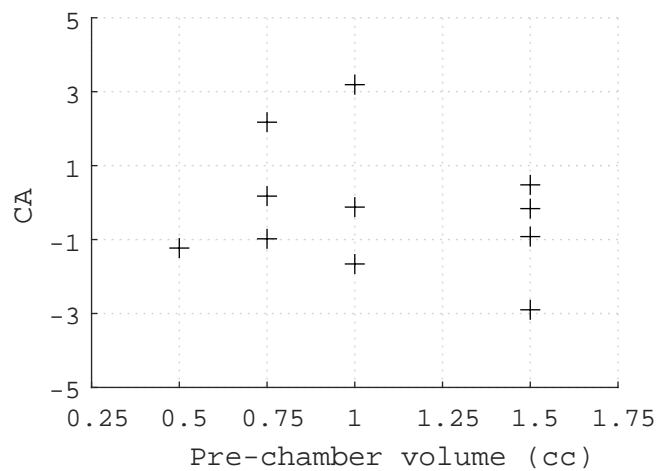
Figure 5.12: Combustion start angle (MFB10%) vs pre-chamber volume with respect to TDC$_{\text{firing}}$

5.2.3 Number of nozzles

The influence of number of nozzles on burn duration was observed to be a function of pre-chamber volume as well. A design with less number of nozzles was found to be effective with a smaller pre-chamber volume and vice versa (Fig. 5.13). A design with higher number of nozzles and a smaller volume doesn't allow pressure to build up inside the pre-chamber. The trend has shown that the number of nozzles can be increased with increasing the pre-chamber volume.
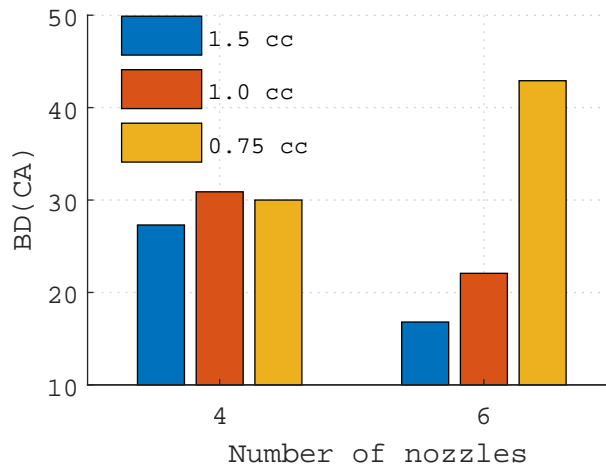
Figure 5.13: Burn duration (MFB10-90%) vs number of nozzles and pre-chamber volume

5.2.4 Nozzle diameter

For the range of the pre-chamber volumes considered, 1.5 mm diameter was observed to be the optimum diameter (Fig. 5.14). A smaller diameter nozzle with a
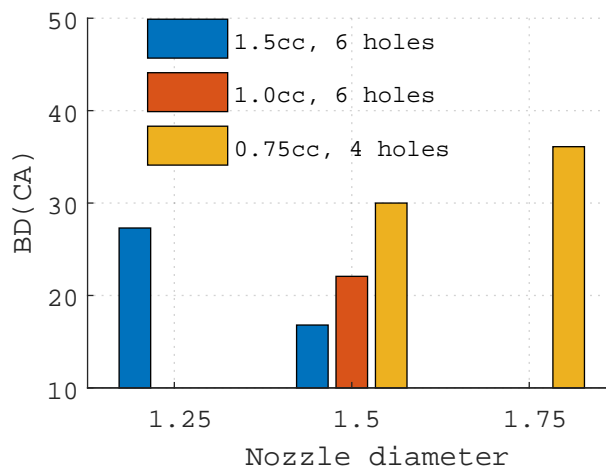
Figure 5.14: Burn duration (MFB10-90%) vs nozzle diameter (1.25, 1.5 and 1.75mm) and pre-chamber volume

large volume pre-chamber was found to limit jet penetration despite having higher pressure inside the pre-chamber, as shown in Fig. 5.15. The same plot also shows reduced pressure inside the pre-chamber with a smaller diameter during compression and increased pressure after combustion, due to higher restriction of nozzles, both can be attributed to increased pressure drop across the smaller diameter nozzles.
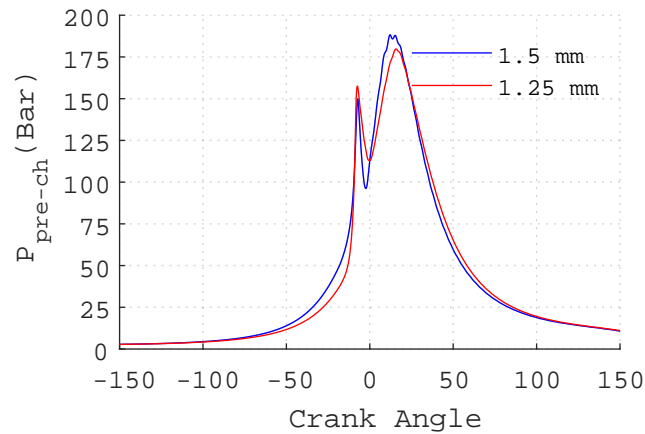
Figure 5.15: Pre-chamber pressure for 1.5 mm and 1.25 mm diameter nozzles

5.2.5 Nozzle entry angle

Tangential nozzle entry was observed to improve the mixing inside the pre-chamber and helped in symmetrical jet ejection from the pre-chamber as shown in Fig. 5.16. For asymmetrical jet ejection, the late ejecting jets have reduced penetration length
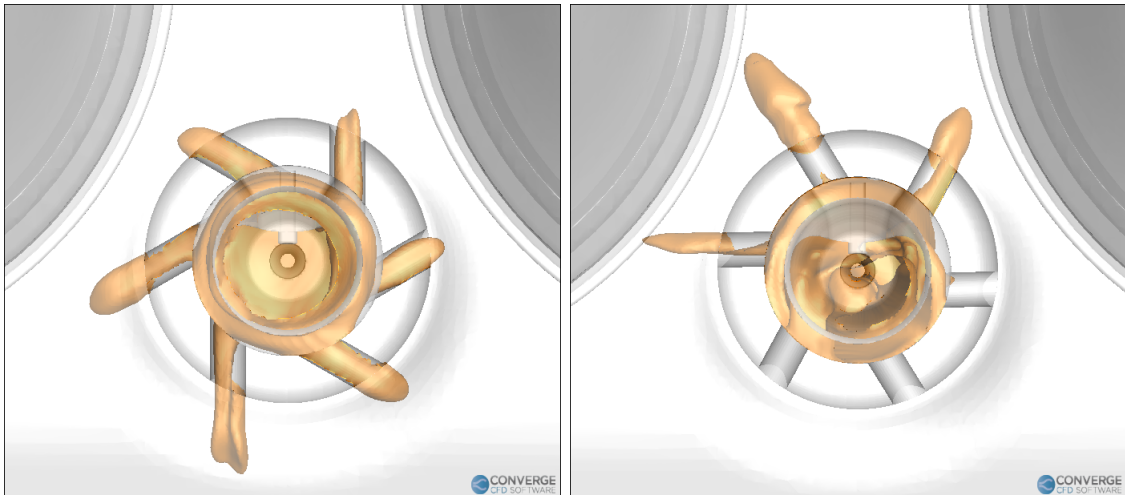
Figure 5.16: Impact of nozzle entry angle on jet flame development.
Left: Tangential entry nozzles, right: Reduced entry angle or radially aligned nozzles.

due to decreased pressure inside the pre-chamber from the earlier ejected jets. The end gas in the main chamber, on side of late ejecting jets, could be exposed to higher pressure for a longer duration, thus increasing the probability of auto-ignition.

5.2.6 Nozzle orientation

Pre-chamber nozzle orientation with respect to combustion chamber was decided such that air-fuel mixture close knock initiation sites burn first. With the base SI combustion, it was observed that knock is initiated inside the valve pockets.

The CAD representation of nozzle orientation is shown in Fig. 5.17. So, the nozzle
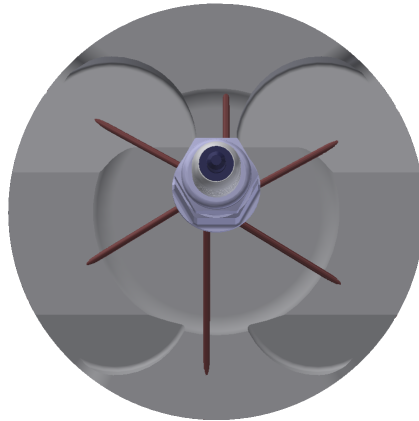
Figure 5.17: CAD representation of nozzle orientation for 6 hole design

orientation is decided such that air-fuel mixture near the valve pockets burns first. The simulation iteration conducted with one pair of nozzles pointed along crank shaft axis, as shown in 5.18, resulted in earlier combustion start, but ended up as knocking cycle. For a pent-roof combustion chamber and bowl piston, air-fuel
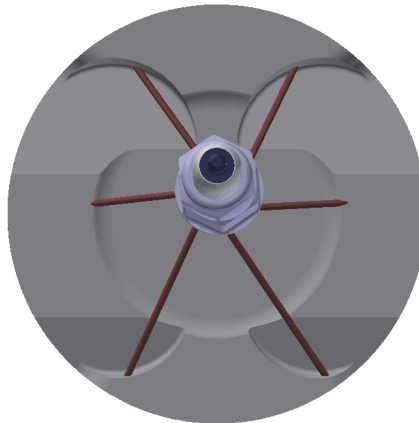
Figure 5.18: Nozzle orientation with reduced ignition delay, but with increased knock probability

mass is more placed near the roof along a mid-cylinder plane, passing through both crank shaft axis and cylinder axis. Two section views of combustion chamber on two perpendicular planes are shown in Fig. 5.19. Thus when the pre-chamber jet

Figure 5.19: Section views of combustion chamber. Left: plane passing through both cylinder and crank-shaft axes. Right: perpendicular to the first plane, passing through squish land.

pass through this area, jet initiated flame front can burn more charge before the

flame front reaching the wall, which is a good thing for shorter ignition delay, but regions where high chances of knocking including valve pockets, burn towards the later part of the combustion process and can hence result in knocking. For the 4 nozzle pre-chamber design, same strategy was carry forwarded and nozzles were directed towards the valve pockets as shown in Fig. 5.20.
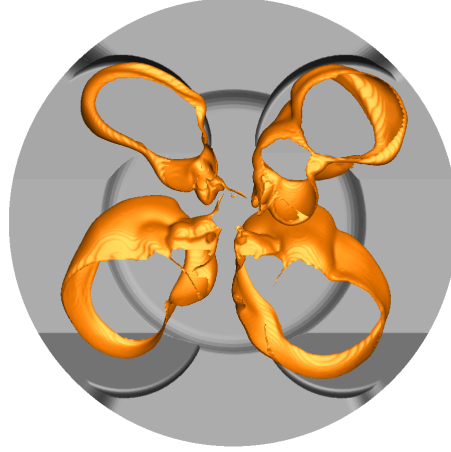
Figure 5.20: Flame front at 4° CA ATDC$_{\text{firing}}$ for 4 nozzle pre-chamber design (Temperature iso-surface = 1700K)

As the pre-chamber is thread mounted on the cylinder head with torque value of 22 Nm, the exact orientation of the nozzle was achieved with different thickness spacers and it required multiple attempts with different spacers to get the right nozzle orientation.

5.2.7   Final design

The parametric study revealed that a larger volume pre-chamber has the ability to reduce the burn duration substantially, but results in a lean mixture inside the pre-chamber which is not ideal for combustion stability. Very short burn duration with varying combustion start is not desirable for an engine which always operates close to knock limit. Based on this understanding, the following two pre-chamber designs were finalised for test validation.

- Pre-chamber 1 (PC1): 1.2 cc pre-chamber volume, 6 nozzles, 1.5 mm nozzle diameter with tangential nozzle entry.

- Pre-chamber 2 (PC2): 0.8 cc pre-chamber volume, 4 nozzles, 1.5 mm nozzle diameter with tangential nozzle entry.

The option 1 was predicted to give shorter burn duration with high cyclic variation. With the second option, moderate burn duration and reduced cyclic variation was
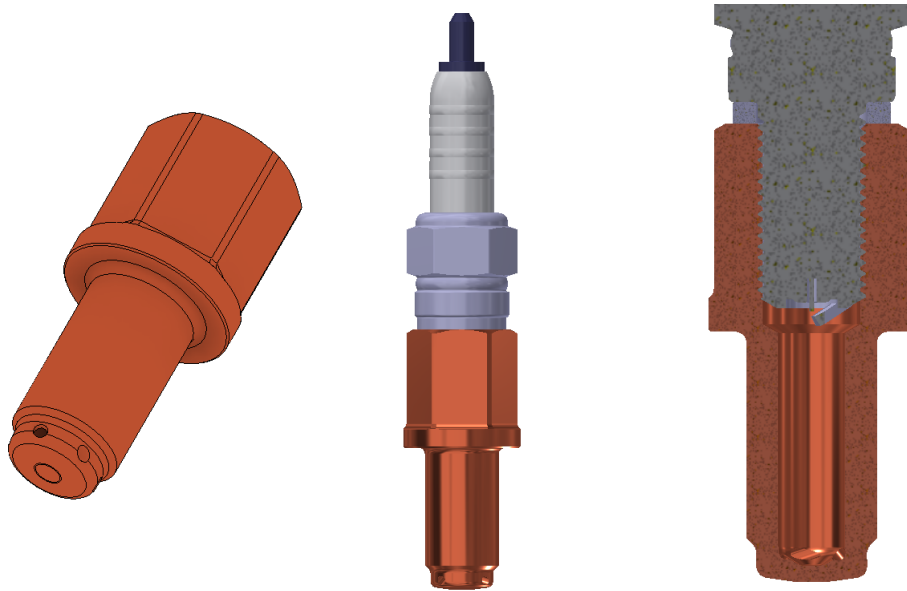
Figure 5.21: Pre-chamber design.

expected. The pre-chamber design with spark plug is shown in Fig. 5.21. Due to additional pe-chamber volume, the compression ratio was reduced by 0.5 and 0.3 units for PC1 and PC2 respectively, from the base specification of 14.0. An M10 spark plug of NGK make with heat range 11 (part number: R0373A-11) was used along with the pre-chamber.

As discussed in the introduction section of this chapter, the pre-chamber design was developed without changing the pre-chamber mounting feature, which is an M12 thread. If the mounting provision can be changed, different pre-chamber internal diameter and length can be studied for a given volume. A design with shorter length and larger diameter helps in better scavenging near the spark plug. These design iterations are proposed as future work as it requires modifications of cylinder head and these modifications may require changes in nearby design features including injector mounting and water jacket.

All nozzles were placed symmetrically around the pre-chamber axis to keep the design simple for manufacturing and assembly, but it is not a necessary or preferred condition. There is a possibility to direct the nozzles exactly towards the valve pockets, which could be beneficial for improved knock resistance, especially on the exhaust side of the combustion chamber, where the nozzles are not pointed towards the exhaust valve pockets, as it can be seen in Fig. 5.17.

5.3 Conjugate heat transfer analysis for material selection

A CFD based Conjugate Heat Transfer (CHT) analysis was conducted to find out the maximum operating temperature of the pre-chamber solid material. This CHT model was developed by including the cylinder head solid geometry to the fluid only model, discussed in the previous section. Cylinder head solid geometry used for the simulation is shown in Fig. 5.22. This study captured heat transfer from the com-
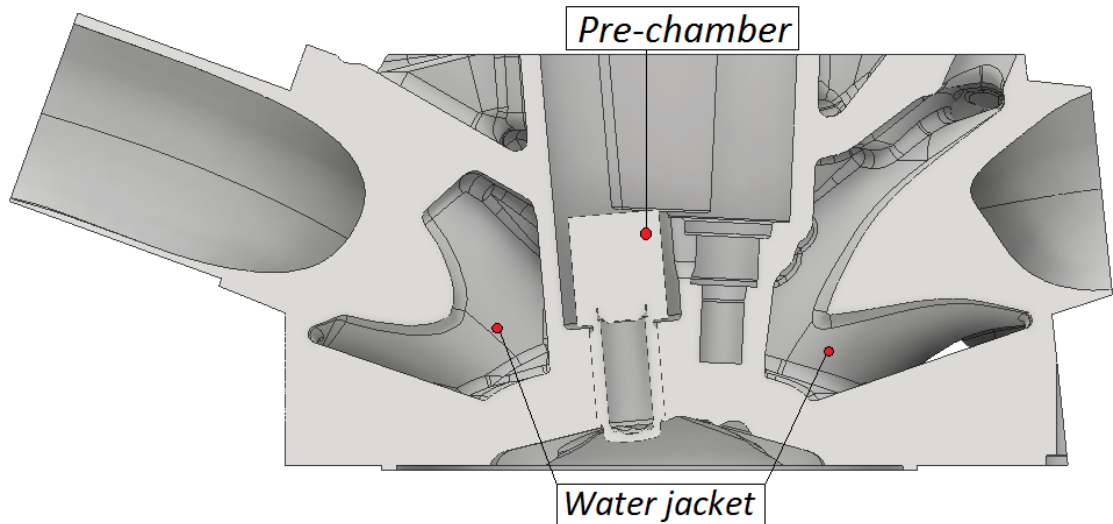
Figure 5.22: Section view of cylinder head geometry for the heat transfer analysis.

bustion chamber to pre-chamber solid and cylinder head and then to water jackets and ambient air.

CHT analysis is required to study the simultaneous heat transfer between solid and fluid regions. In an engine, the time-scale required to resolve solid heat transfer is much higher than time-scales of fluid flow, combustion and convective heat transfer inside the cylinder. So, it takes many engine cycles for the solid temperature to reach a steady state. CONVERGE CFD uses super cycling approach to accelerate heat transfer to reach a steady state in solid domain. In super cycling, fluid and solid heat transfer is solved together using a transient solver first and then periodically freeze the fluid domain to solve the steady state solid temperature [58]. This process is repeated until the solid temperature converges. In this simulation, it took five cycles for the solid temperature to converge.

Following assumptions are used to simplify the calculation.

- Heat transfer through valves is ignored due to the fact that it is not affecting heat transfer to and from the pre-chamber solid part.

- Heat transfer to water jackets and ambient air is defined through a heat transfer coefficient (500 and $10 W/m^2 K$ respectively) and a far field temperature based on the available engine test data. These HTC values are taken from literature and a lower value is assumed to simulate higher solid temperature. A detailed approach would require HTC values from a separate steady state heat transfer analysis of water jacket.

- Copper is used as pre-chamber material because it has very similar thermal conductivity of Copper Beryllium (CuBe): the material planned to use for the pre-chamber construction.

Temperature distribution at a mid-plane section of pre-chamber is shown in the Fig. 5.23. Surface temperature of the pre-chamber solid is shown in the Fig. 5.24.
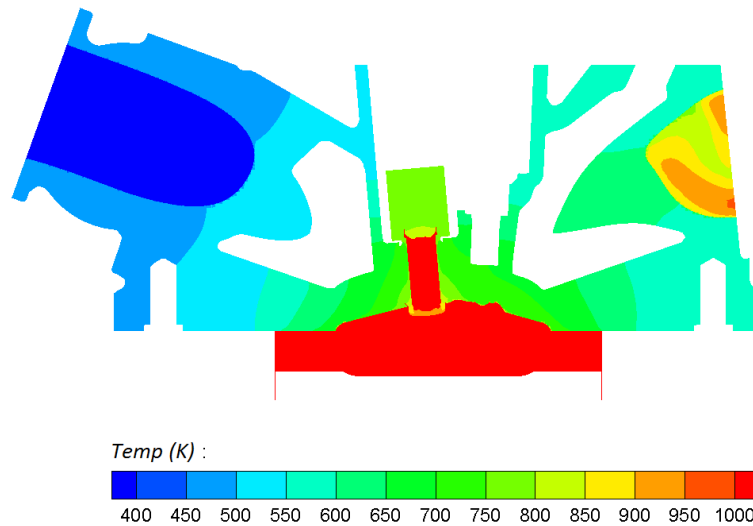
Figure 5.23: Temperature distribution at 40 deg after TDC$_{\text{firing}}$.

Tip area of the pre-chamber is observed to be at the highest temperature as this
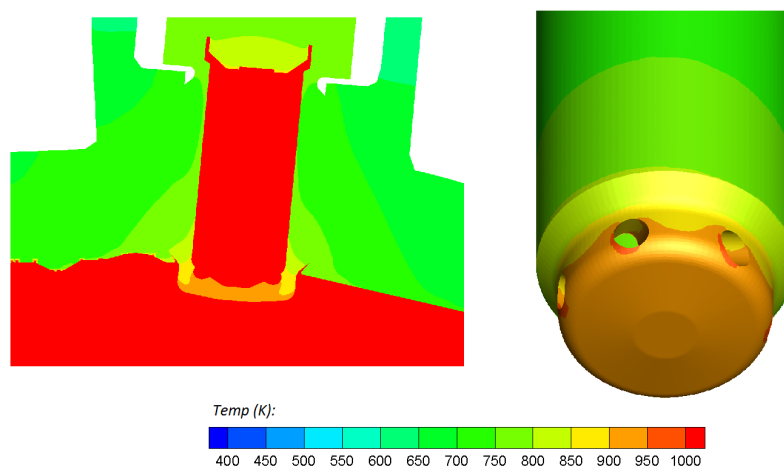
Figure 5.24: Temperature distribution of pre-chamber at 40 deg after TDC$_{\text{firing}}$. Left: Section view of pre-chamber. Right: Pre-chamber surface temperature.

region takes heat from both pre-chamber and main chamber regions. The maximum temperature at the pre-chamber tip was observed to be above 900K. At this temperature levels, CuBe Alloy 3 was identified as the suitable material due to superior high temperature strength and higher thermal conductivity. The melting point of CuBe Alloy 3 is 1300 K. Properties of Copper Beryllium, provided by the material supplier is given in Appendix B.

During initial testing with the pre-chamber, it was found that pre-chamber mounting threads (same as the spark plug mounting for the base engine) melted and fused to the pre-chamber body as shown in Fig. 5.25a and removal of the pre-chamber from the cylinder head observed to be difficult due to the same reason. As a design countermeasure, cylinder head design was modified to add copper beryllium insert, which was press fitted on a larger bore and later machined for pre-chamber mounting M12 threads. The modified design is shown is shown in Fig. 5.25b.

(a) Post test pre-chamber part with melted aluminium on threads.
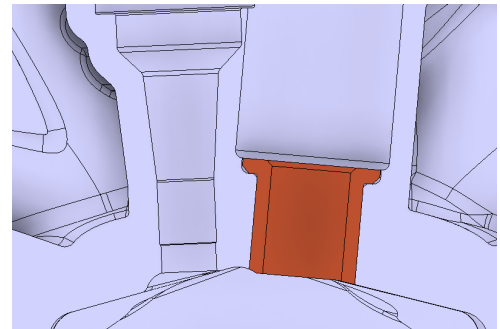
(b) CuBe insert on cylinder head for pre-chamber mounting.

Figure 5.25: Pre-chamber design improvement.

Chapter 6

Experimental Set-up: Engine Testing

Contents

6.1 Introduction

An AC dynamo-meter test facility available at London South Bank University was used to compare the engine performance with base spark plug design and the pre-chamber designs, finalised through CAE study. The research project also involved development of a bespoke single cylinder research engine and a two-stage super charger boost rig. The CAD representation of the engine test set-up is shown in Fig. 6.1. With this AC dynamo-meter, engine can be motored to undertake friction measurement with ignition and fuelling switched off. The engine test cell operation was controlled through the test cell automation system, CADET V14[1]. The CADET controls dyno loading and speed. It also controls the operation of a cooling post with three heat exchangers to maintain the temperature of engine coolant, lubrication oil and air. Some of the measurements are taken by the test cell system including engine torque, fuel flow rate, air flow rate, air temperature, pressure and humidity.

---

[1]A product of Sierra CP engineering
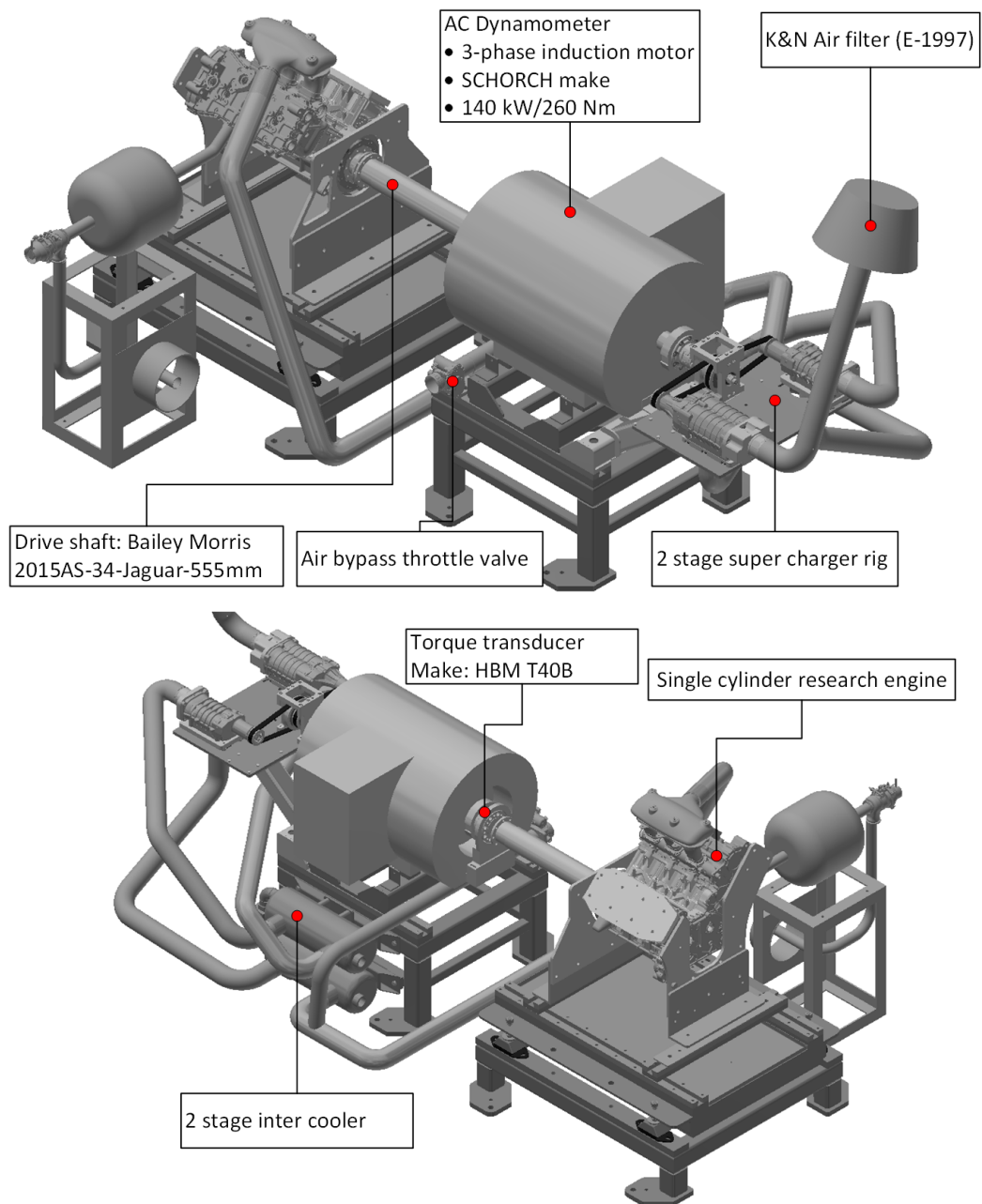
Figure 6.1: Engine dyno test set up.

The engine ECU also records engine specific measurements including relative AFR (λ), engine knock level and exhaust gas temperature. A Matlab script was used to combine both set of readings to produce a spread sheet for easier visualisation and analysis.

6.2   Single cylinder research engine

The single cylinder research engine (SCRE) was developed to study the combustion characteristics of a twin-turbo lean-burn V6 motor-sport engine, used in fuel

flow limited racing events. As the research is aimed to improve the combustion performance of the base engine, results from single cylinder can be implemented on multi-cylinders of the base V6 engine. The CAD representation of the SCRE is shown in in Fig. 6.2. The single cylinder engine was developed from the base V6
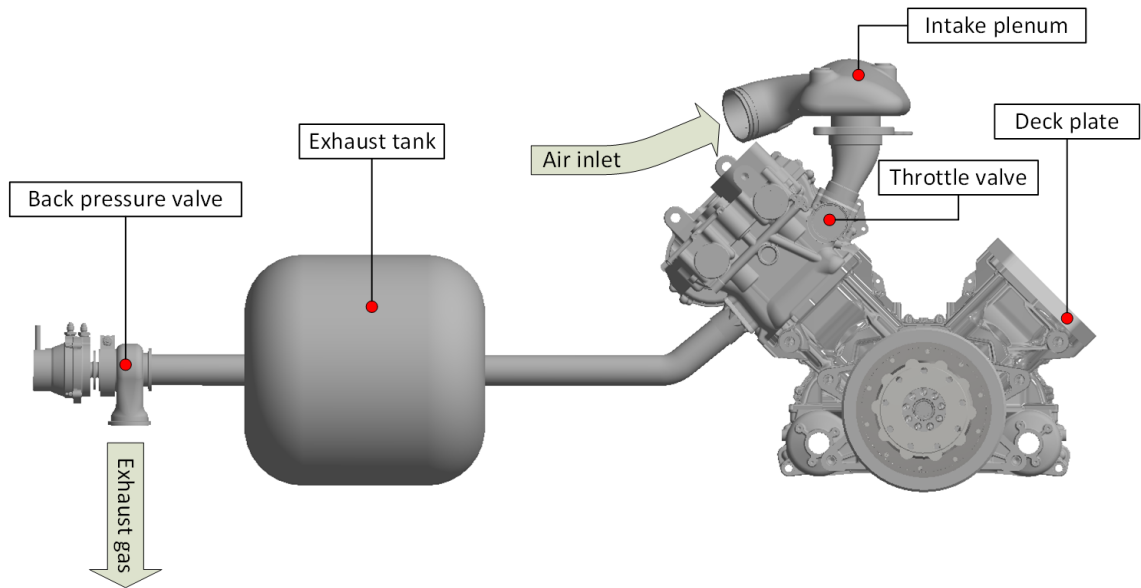
Figure 6.2: Single cylinder research engine.

engine with following changes:

- Both turbochargers removed.

- Crank-train and cylinder head assembly on the right hand side bank was removed, effectively making an in-line 3 cylinder engine. This arrangement helped in achieving balancing of the primary and secondary forces without any additional balancer shafts.

- Counter weight mass reduced to compensate for the reduction in rotating mass on the right hand side bank.

- On remaining active bank, ignition and fuelling disabled on two cylinders with only one cylinder firing.

- Moment of inertia of the flywheel was increased to compensate for higher torsional vibration of the crank-shaft, resulting from the absence of power strokes from 5 cylinders.

- On active bank, all three cylinders have active valve-train system, but air supply to two cylinders were blocked at intake runner while testing the third cylinder to save pumping losses from the two cylinders. All three cylinders were prepared with three different pistons, developed to evaluate three different

combustion chamber designs. Cylinder 6 was built with the base bowl-piston as that of the turbo-charged base engine. Cylinder 5 was built with a flat piston with higher compression ratio of 15.

- Deactivation of two intake runners on two cylinders also helped to match intake pressure pulsations with the base V6 engine.

- An exhaust tank (28 Litre) was added to attenuate exhaust gas pulsations.

- An exhaust back pressure valve was added to replicate exhaust back pressure, imposed by the turbo-charger on the base V6 engine.

- Few key design specifications of the single cylinder research engine are given in the Table. 6.1.

Combustion chamber	Pent-roof with bowl piston
Compression ratio	14.0 (Cyl 6) , 15.0 (Cyl 5)
Maximum engine speed	8000
Displacement	500 cc
Bore/stroke ratio	1.24
Number of valves per cylinder	4
Fuel	Gasoline with 20.4% ethanol by volume
Fuel injection pressure	325 Bar

Table 6.1: Design specifications of the single cylinder research engine

The engine has a centrally mounted direct fuel injector with cam operated high pressure fuel pump. The fuel flow to the engine was measured by a Fuel Measurement System (FMS 1000^2), connected to the test cell automation system.

6.3 Two stage supercharger rig

With the SCRE, exhaust enthalpy from single cylinder was not sufficient enough to power a turbo-charger and hence a separate high pressure air supply system was developed to compensate turbocharged air supply of the base V6 engine. A two-stage supercharger rig was developed which was designed to be driven by the dyno. The CAD representation of the super-charger rig is shown in Fig. 6.3. Outlet of superchargers connected to a water-cooled inter-cooler with closed loop temperature control, managed by test bed automation.

---

[2]A product of Sierra CP engineering
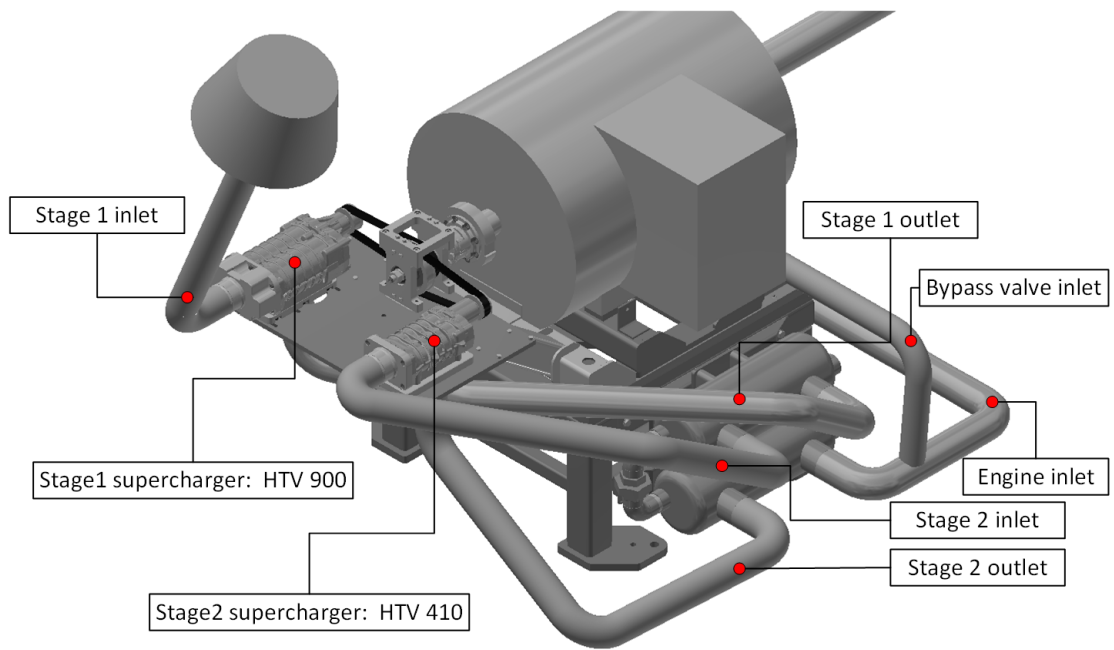
Figure 6.3: Two-stage supercharger boost rig.

6.4   Engine management system

The LifeCal[3] software along with Life Racing F90F ECU was used for the calibration of the single cylinder research engine. The schematic diagram 6.4 explains various hardware units and key measurement and actuation signals used for the engine calibration.

6.4.1   Knock limited spark advance (KLSA) strategy

The SCRE was equipped with a transducer based knock sensor mounted close to the combustion chamber on the cylinder block outer surface, which detects the surface vibrations produced during combustion. ECU decides the knocking state by analysing the vibration signal measured by the knock sensor and then retard the ignition timing when a knocking cycle is detected. This momentary ignition retard is required to prevent "runaway knock"[76]. Runaway knock is defined as the continuous knocking cycles and it happens when an initial knocking event destroys the thermal boundary layer inside the combustion chamber and results in very high combustion chamber wall temperature and thus creates hot spots, increasing knock probability for next cycles. Ignition angle is reinstated back in smaller increments in subsequent cycles.

There are different strategies employed in engine calibration to detect a knocking cycle. One strategy proposed by Bosch [77] and is similar to the strategy employed

---

[3]A product of Life Racing Ltd
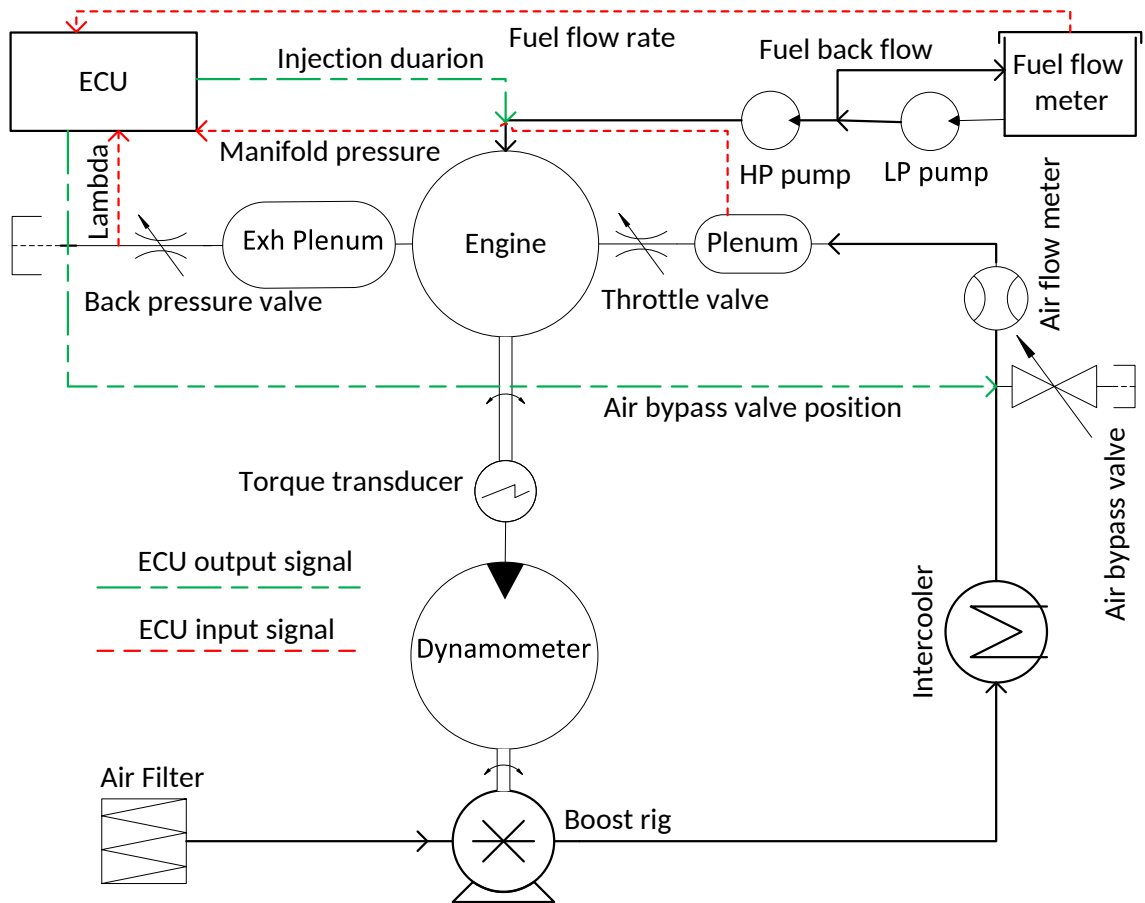
Figure 6.4: Schematic diagram of single cylinder engine test set-up. Various signals and actuators to maintain fuel flow rate at full-load are shown.

for the SCRE is discussed here. In this method, ECU looks for the signal in a calibrated measurement window close to $\text{TDC}_{\text{firing}}$ where the knock is expected to occur. This signal is then band filtered around the knocking frequencies, rectified and integrated to obtain a measure of energy within the window. A normalised value of this energy value is used to compute the final knock intensity. One example for normalising variable is the measure of energy associated with a heavy knocking cycle, which can damage the engine. A moving average of this normalised knock intensity values, computed from a fixed number of upstream cycles is used to define a reference level, representing a base noise level for that operating point. A knock threshold value is also defined as a function of this base noise level. This knock threshold is decided in the testing by confirming an actual knocking cycle, either by analysing the cylinder pressure data or by listening to the characteristic metal hitting noise associated with the engine knock. When an individual cycle knock intensity crosses the knock threshold value, ECU detects it as knocking. Fig. 6.5 shows implementation of this knock detection strategy for SCRE.
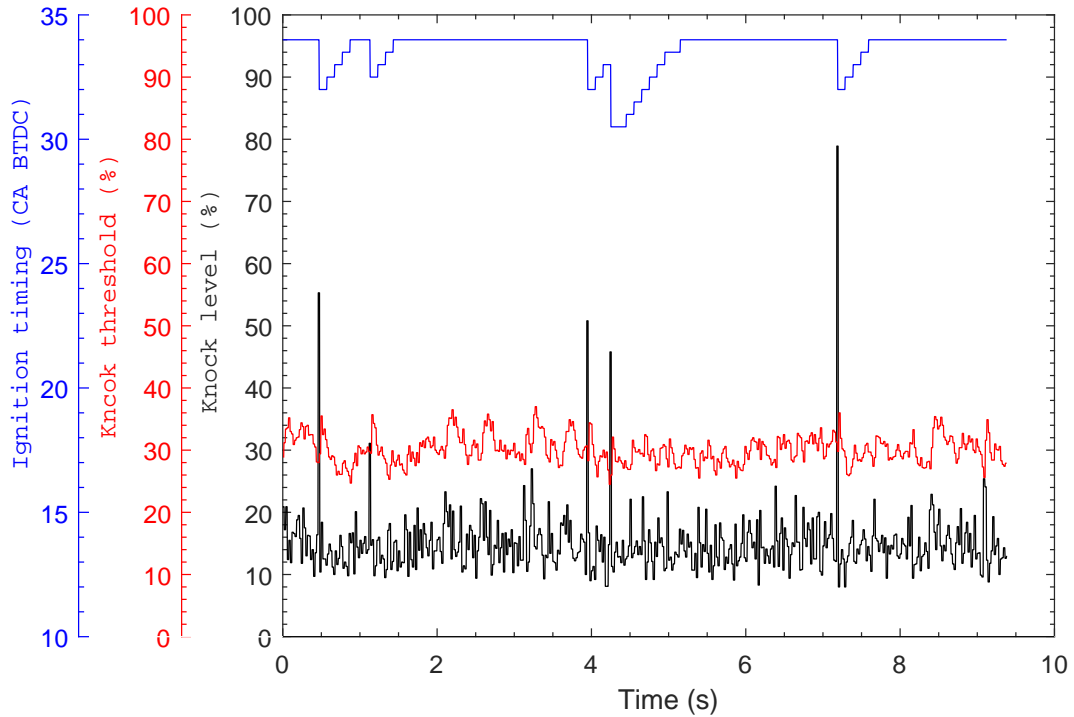
Figure 6.5: Knock Limited Spark Advance at 6000 rpm, full load.

6.4.2   Test pattern

A motor-sport engine mostly runs at full load and the performance measurement for the single cylinder engine was also done at full load. Performance measurement was conducted in an automated test sequence, controlled by the test bed automation software, CADET V14. The test sequence was initiated once the engine achieved optimum coolant and oil temperature level. The engine test set-up has a closed loop control to maintain air, coolant and oil temperature to the desired level. Both oil and coolant inlet temperature to the engine was maintained at 85ºC and engine air inlet temperature was maintained at 35ºC. The test cell had no provision to control test cell ambient temperature and test cell ventilation was manually adjusted to keep the temperature at moderate level, depending on outside temperature. The automated test sequence is shown in Fig. 6.6. At a constant engine speed, throttle position is changed from part load to full load and maintained at full load for 10 seconds. Simultaneously, supercharger bypass valve is closed to achieve a manifold pressure target, which is defined as a function of throttle position and engine speed in an engine calibration map. Full load manifold pressure target is set at a higher value than what actually required for achieving target fuel flow rate and lambda target. Once the fuel flow target is achieved, the strategy corrects the manifold pressure target to maintain the fuel flow rate. Total measurement duration at full load was 10 seconds. Engine achieves a stable condition within initial 5 seconds and data logging was done for last 5 seconds. The measured parameters for last 5
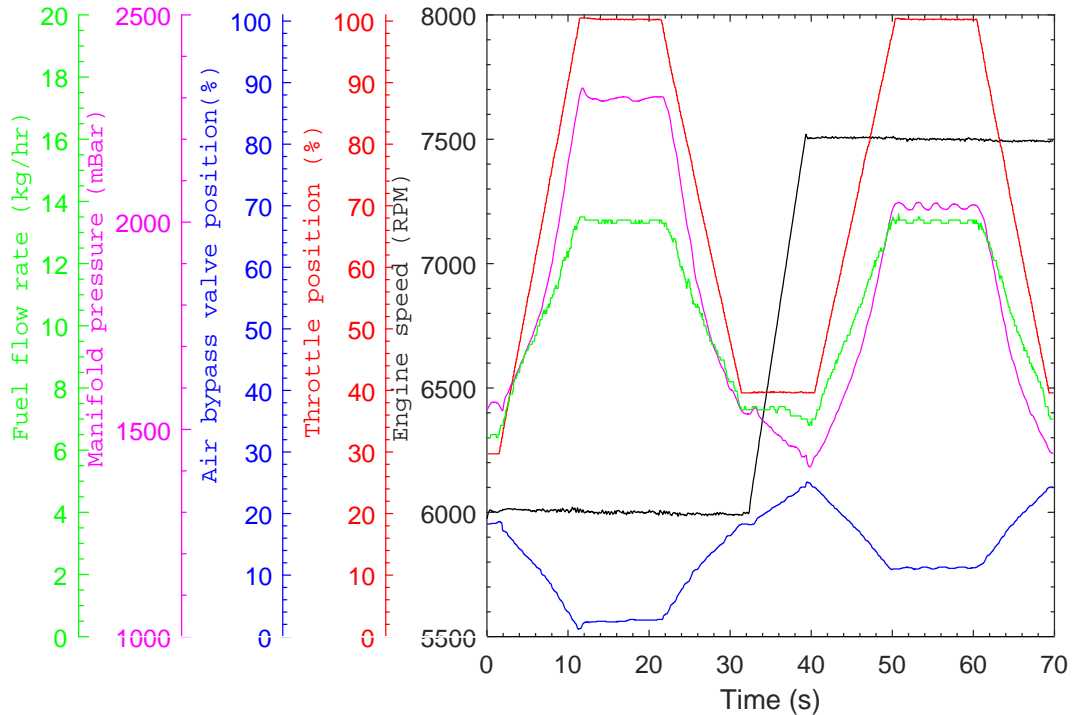
Figure 6.6: Full load performance measurement test pattern.

seconds is averaged and used for the analysis.

6.5   Combustion measurement

Crank angle resolved cylinder pressure was measured to study the combustion performance of the single cylinder research engine. AVL X-ion data acquisition system was used to measure the cylinder pressure. A piezoelectric crystal based pressure sensor (AVL G015DK) was mounted on the cylinder head with the probe location is on the intake side squish land. Measurements are taken for 100 continues cycle and with a resolution of 0.1 deg CA. The measured cylinder pressure data is post processed in AVL CONCERTO software to calculate various derived parameters including heat release, knock signals, cyclic variation and IMEP.

6.6   Summary

This chapter described the test engine facility developed at London South Bank University to run a single cylinder engine to do performance evaluation of pre-chamber ignition system for fuel-flow limited motor-sports application. This test cell was developed completely new and some of the hardware concepts used for this test rig, including the two-stage boost rig and the V6 converted single cylinder

research engine were unique in concept.

Individual contribution to test rig development

Development of this engine test facility involved contributions from different organisations including Advanced Engine Research Ltd and Sierra CP Engineering Ltd. As this engine test facility was developed altogether new, I had to get involved in different activities that includes technical as well as project management and coordinating between different organisation. Following are the key technical areas I worked to develop the test rig:

- Calculation of engine balancing forces to decide which multi-cylinder engine to be used as the base for single cylinder research engine development, with minimum modifications for the base multi-cylinder engine, and a V6 engine was proposed.

- Design and fabrication of mounting components for single cylinder research engine on the engine dynamo-meter.

- Selection of low pressure fuel pump and fuel pressure regulator.

- Design and development of air intake system for super-charger rig, single cylinder engine and air bypass valve system.

- Development of the calibration strategy in LifeCal for single cylinder engine with a closed loop control for bypass pressure valve to maintain manifold pressure demand [4]. On the turbo-charged base V6 engine, same is achieved through controlling turbo-charger waste gate valve and it required a new strategy to operate the super-charger rig for the single cylinder engine.

---

[4]This calibration strategy was developed under the guidance of Will Pedley of Advanced Engine Research Ltd.

Chapter 7

Engine Performance Results

Contents

7.1   Introduction

This chapter discusses full load performance of two pre-chamber designs which were developed based on the CFD study discussed in Chapter 5 and its comparison to the base spark ignition performance. Initial testing was done on cylinder with compression ratio of 14 and with fuel flow rate of 13.32 kg/hr. Based on this evaluation, one pre-chamber was selected for further testing and full load tests were repeated with increased dilution and another case with a higher compression ratio of 15. Engine full load tests were conducted with following parameters maintained to a target value through a closed loop control strategy.

- Fuel flow rate (13.32 kg/hr)

- Intake air, coolant and oil temperature

- Relative AFR (λ=1.2) measured at exhaust pipe

- Exhaust back pressure

Humidity was not controlled for the tests as provision for the same was not available with the test facility. Exhaust back pressure was taken from 1D simulation results for the base turbo-charged V6 engine. Performance measurements were done at full load and two speed points: 6000 and 7500 rpm. The fuel flow target of 13.32 kg-hr for the single cylinder engine is corresponding to a total fuel flow rate of 80 kg-hr for the base V6 engine.

Both fuel flow rate and test speeds are different from the values used in the CFD model development (Chapter 4) and for the pre-chamber design parametric study (Chapter 5). This was due to a belt failure observed with the boost rig and eventually one stage had to be removed from the boost rig, limiting maximum outlet pressure to a lower value. So, fuel flow rate target had to be revised from 17.5 to 13.32 kg-hr for the testing. The same manifold pressure limitation also prevented running higher lean limit at a lower engine speed. Also, with the single cylinder engine, increased crankshaft torsional oscillations were observed at 7000 rpm and test speeds had to change to 6000 and 7500 rpm. These two speed points tested were on either side of the engine speed at which the simulations were conducted. As both test points were run at the same fuel flow rate of 13.32 kg/hr, at higher speed, the engine uses less fuel per cycle and hence produced lower $IMEP_g$. Manifold absolute pressure was above 2.0 Bar for both the test points.

In §6.4.1, knock detection strategy utilised for the engine was discussed in detail. For the spark plug ignition, full load test at a speed was performed with ignition system allowed to learn (continuously advancing ignition timing till detecting knock and then retarding) while maintaining a moving average spark retard of 0.2° CA over 100 cycles. This ignition learning with maintaining an average spark retard was done with a provision available in the calibration software. This provision saves the effort of conventional approach of deciding ignition timing by listening to engine knock to decide the threshold knock level. Once the ignition angle that achieves 0.2° CA average spark retard was identified, same was updated as the base ignition angle for the future tests and ignition learning was switched off thereafter. With the ignition learning switched off, maximum ignition angle for a given operating point is limited. With this setting, the engine responds to a knock event which arises from cyclic variation, and momentarily retarding by a pre-defined angle and then reinstated to the base ignition angle in smaller steps in subsequent cycles, as previously shown in Fig. 6.5. This strategy allows engine to operate at the Knock Limited Spark Advance (KLSA) while maintaining the ignition angle nearly constant. It is worth to mention again that the ignition angles for the base spark ignition engine all full-load operating points were knock limited and MBT condition was not achieved.

With the pre-chamber ignition, the transducer based knock signal was observed to be very noisy. This is due to additional high frequency oscillations associated with the pre-chamber jets, which appear in the same frequency range of knock excited vibrations. So, with the pre-chamber combustion, ignition timing was decided by listening to engine knock noise and also by observing cylinder pressure traces. With the pre-chamber ignition, KLSA was not achieved as it requires momentary ignition retard with a knock event, which was not possible with noisy knock sensor signals. Thus, for actual implementation, an alternate knock detection strategy would be required to get the best performance from the engine. Cylinder pressure based knock detection methods are discussed in Chapter 8 with a suitable pressure based method is identified to detect knock with the pre-chamber ignition. With the pre-chamber ignition, knocking was not observed at 7500 rpm and ignition timing was decided by the MBT ignition timing. For pre-chamber testing, all calibration parameters other than ignition timing were kept the same as the base spark plug case.

7.2 Evaluation of pre-chamber design

7.2.1 Engine performance

Full load engine performance results (indicated power and ISFC) are shown in Fig. 7.1, along with ignition timing and exhaust gas temperature. All the test cases were repeated four times and the best result was used for the comparison, yet the repeatability was found to be good. As the single cylinder engine was built with active crank-train and valve-train systems on all three cylinders, frictional losses are substantial and hence indicated figures are used for both power and specific fuel consumption. As the cylinder pressure sensor used for this experiment is of lower sensitivity type, pumping loop calculation was not accurate and hence gross indicated values are used for all calculations here. The changes which are evaluated in this study are related to combustion and had minimum influence on friction and gas exchange, so the changes observed in the indicated figures must be seen in net power and BSFC in the same proportion. The ignition angle with the pre-chamber was retarded by around 14 degrees at both points, which shows a substantial reduction in burn duration achieved with the pre-chamber ignition. The exhaust gas temperature observed with both pre-chambers are lower compared to spark ignition case. Both these results together show combustion duration with the pre-chamber is retarded substantially over the spark ignition. Exhaust gas temperature is an indicator for combustion phasing and a lower value indicates combustion phasing is advanced over the spark plug combustion, which means knock resistance of the engine is improved. Only PC2 shows performance gain over the spark ignition, de-
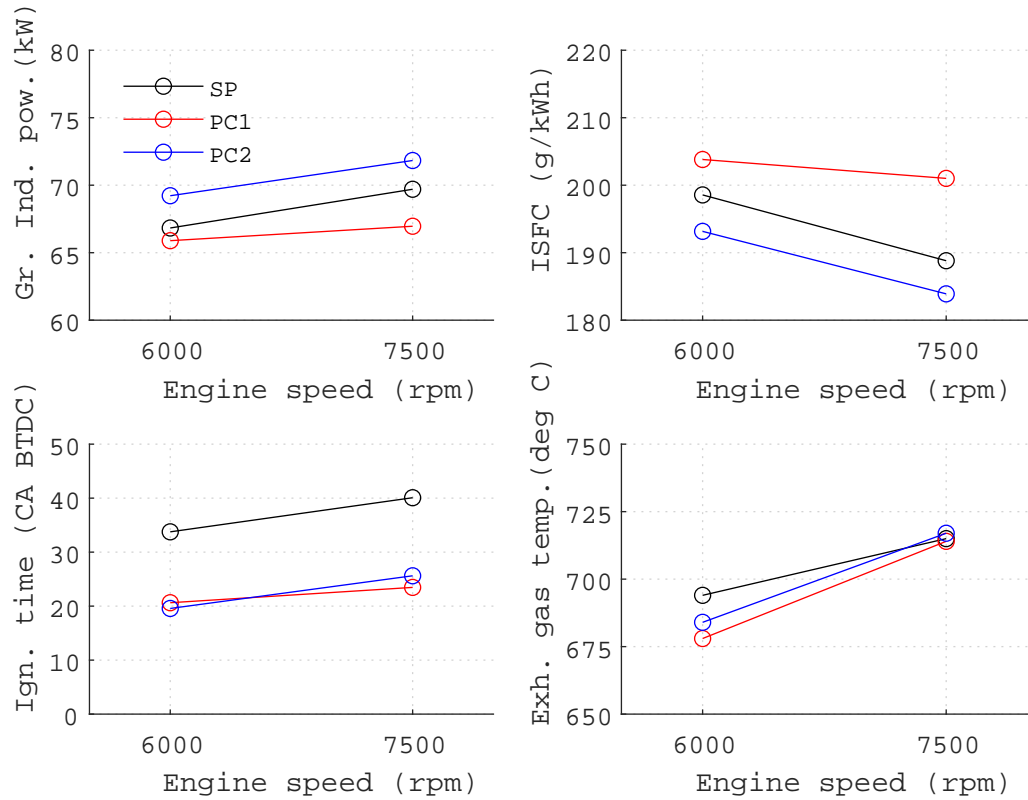
Figure 7.1: Full load engine performance at $\lambda = 1.2$, fuel flow rate=13.32 kg-hr

spite PC1 shows identical ignition timing as that of PC1. The reason for this drop in performance with PC1 is discussed in following section.

7.2.2 Combustion analysis

Cylinder pressure data was measured for 100 continues cycles for all the test points discussed in the previous performance comparison section. The measured cylinder pressure with respective average data is shown in Fig. 7.2. The pre-chamber combustion shows substantial difference to spark plug combustion with narrow and closely placed peak pressure curves. The comparison of average pressure curves are shown in Fig. 7.3. At 6000 rpm, peak pressure was increased by 10 bar with PC2. PC1 also achieved higher peak pressure at 6000 rpm, but this higher peak pressure was not translated to gain in IMEP_g. The gain in peak pressure is much reduced at 7500 rpm with PC2 and a lower peak pressure was observed with PC1 compared to the spark plug case.

For constant fuel flow rate, engine consumes same fuel flow at both speed points. But for the same fuel flow rate, a higher engine speed requires less fuel per cycle. Thus for a given λ, a higher engine speed requires reduced air flow and manifold boost pressure and produces less IMEP_g. Also, a higher engine speed results in
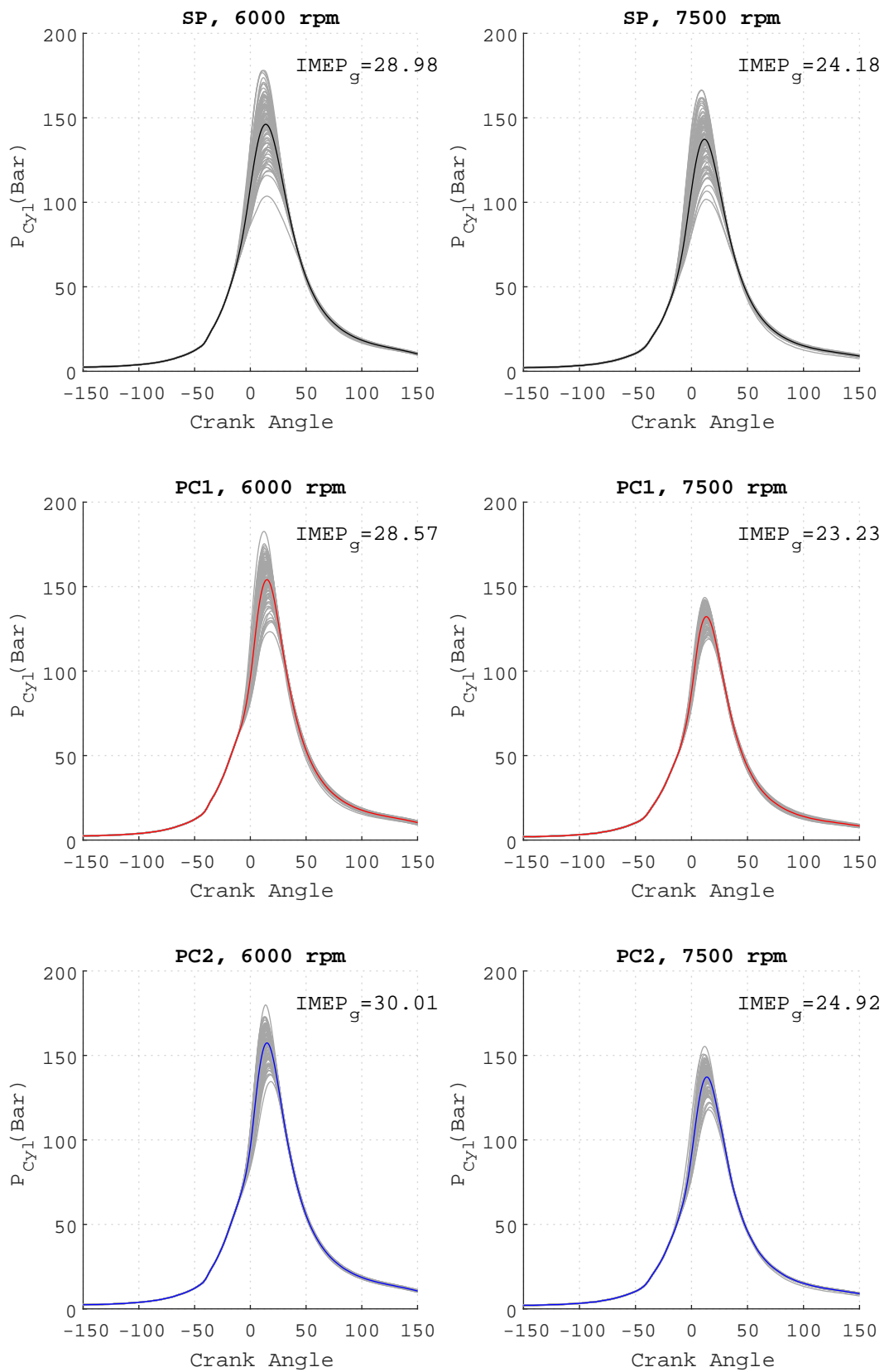
Figure 7.2: Cylinder pressure comparison for spark plug and two pre-chamber designs, 100 cycles data with average pressure curve
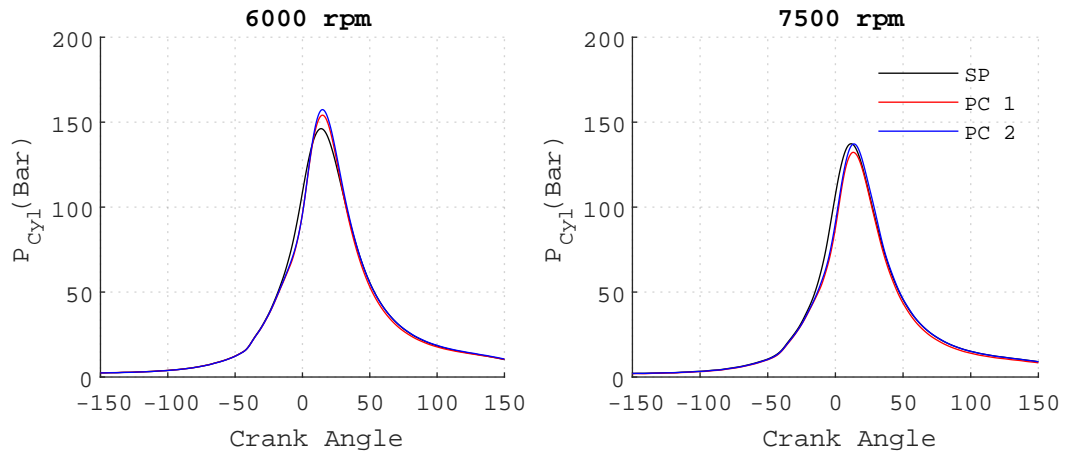
Figure 7.3: Average cylinder pressure comparison for spark plug and two pre-chamber designs.

reduced end gas residence time and has increased turbulence from higher piston velocity. Both these factors make a higher engine speed less susceptible to knock. Thus, for the engine speeds tested, performance at 6000 rpm was more affected by knocking compared to 7500 rpm. As shown in Table. 7.1, for spark ignition, crank angle at which MFB50% achieved was retarded at 6000 rpm compared to 7500 rpm. So the gain in $IMEP_g$ achieved with PC2 is a result of combustion phasing advance

	MFB50% (CA ATDC)	
Engine speed	**6000**	**7500**
SP	14.1	11.0
PC1	12.3	10.8
PC2	12.5	11.3

Table 7.1: Comparison of combustion phasing anchor angles (MFB50%, CAD with respect to TDC) for spark ignition and pre-chamber ignition.

possible with the pre-chamber ignition. The combustion anchor angle, MFB50% was advanced even without a live knock detection system. At 7500 rpm, even for the spark ignition, engine was operating close to MBT point and gain in $IMEP_g$ from the pre-chamber combustion was reduced. For this engine, MBT is achieved when MFB50% is between 10 to 12 CA After TDC_{firing}.

The comparison of CoV of $IMEP_g$ and maximum pressure is shown in Fig. 7.4a and Fig. 7.4b. Standard deviation of combustion anchor angles: MFB10% and MFB50% are shown in Fig. 7.5. Standard deviation is used to show variation of combustion anchor angles instead of CoV because crank angle close to zero appears in the denominator for CoV calculation. All the test cases did show CoV of $IMEP_g$ less than 3% and noticeable differences are only visible with CoV of Pmax. With the PC2, lower CoV and higher $IMEP_g$ was achieved at both speed points over the base spark ignition case. Ignition delay and burn duration comparison are shown in

(a) IMEP$_\text{g}$ (b) Maximum pressure
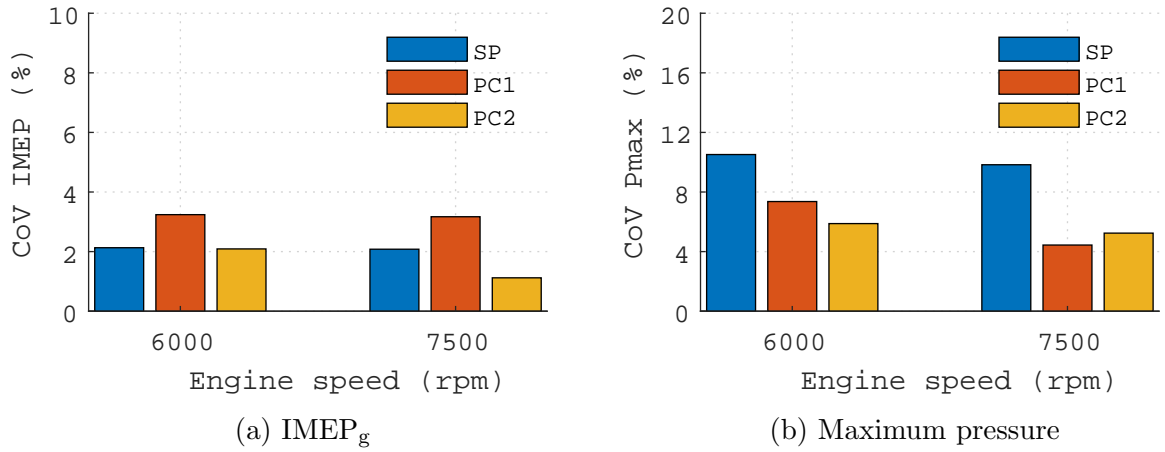
Figure 7.4: Coefficient of variation of pressure related parameters.

(a) MFB10%   (b) MFB50%
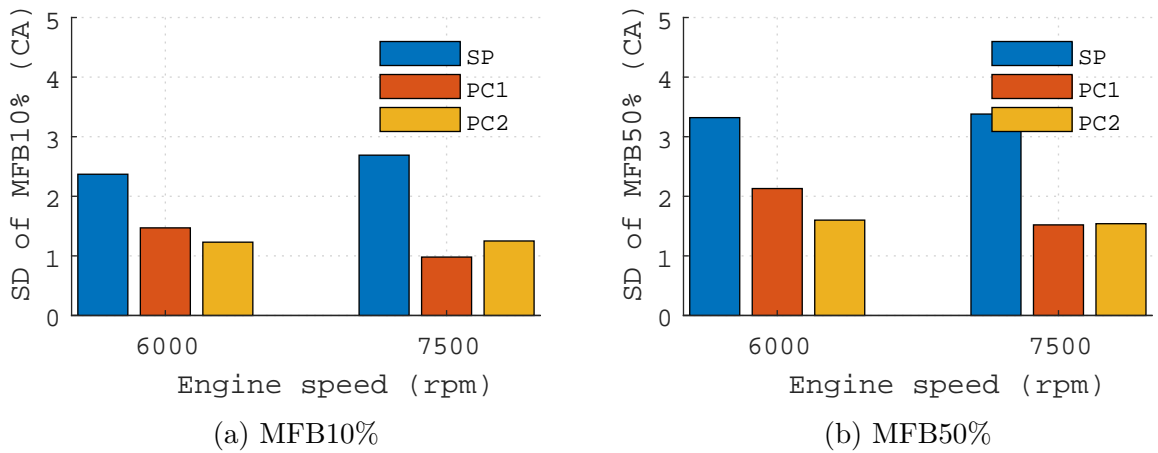
Figure 7.5: Standard deviation of combustion anchor angles.

Fig. 7.6. Despite having identical ignition delay and reduced burn duration as PC2, PC1 produced less IMEP$_\text{g}$ than even the base spark ignition case. PC1 resulted in higher CoV of IMEP$_\text{g}$ compared to the spark plug case, despite having noticeable lower CoV of peak pressure as shown in Fig. 7.4b.

This results show that performance gain from reducing burn duration is not significant and more gain is obtained from advancing combustion phasing. Combustion phasing advance results in higher peak cylinder pressure, because combustion happens with air-fuel mixture is at more compressed sate than a late combustion event and hence more piston work (PdV) is produced. This finding agree with the observation made by Heywood [8] that reducing burn duration has diminishing effect on ISFC reduction. Nevertheless, a faster burn process is more robust, and has the potential to operate much leaner, without a large deterioration in combustion quality [8].

The base motor-sport engine was developed with high intake valve seat mask-
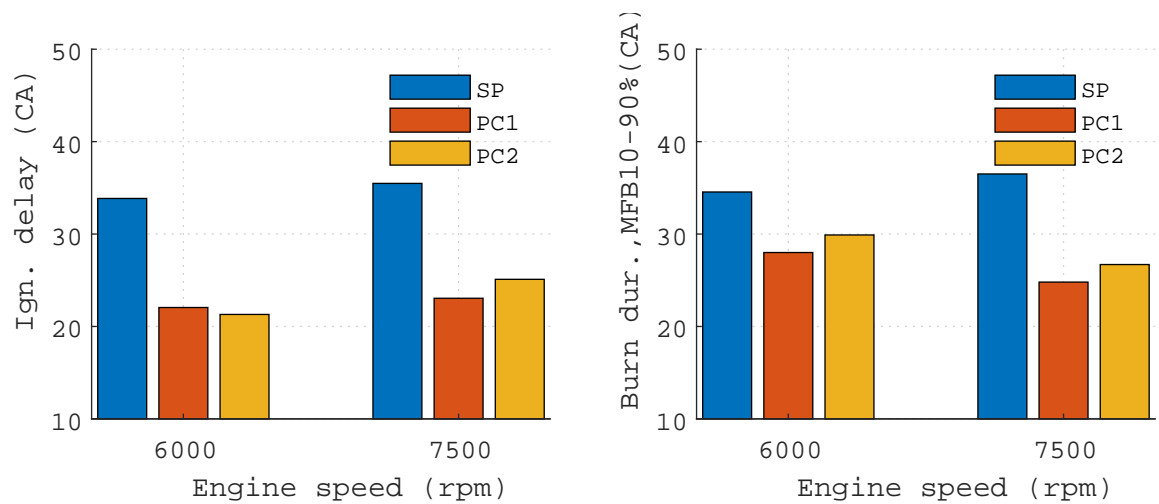
Figure 7.6: Ignition delay and burn duration comparison of spark plug and two pre-chamber designs

ing to induce tumble inside the cylinder to aid turbulent combustion. So the burn duration was not very high for the base engine with spark ignition, despite burning lean mixture. The penalty associated with high valve seat masking is a reduced discharge coefficient across the intake valves and thus requires increased manifold pressure to get the required air flow for given fuel flow and λ. Higher manifold pressure is achieved on a turbo-charged engine by closing exhaust waste gate valve to direct more exhaust gas to turbine. Closing of exhaust waste gate valve results in higher exhaust back pressure and resultant increased residuals inside the cylinder. So the pre-chamber opens a possibility of reducing intake valve seat masking and can achieve reduced manifold pressure and exhaust back pressure. This work established that combustion start is independent of in-cylinder flow field. Even the earlier stage of combustion in the main chamber is influenced by jet induced turbulence. Also, it was observed that jets coming out of the pre-chamber produces shock waves, which discussed in detail in Chapter 8. These shock waves can potentially change the flow field in the main combustion chamber. It is yet to understand the influence of shock waves on combustion chamber mean flow field and turbulence level. So, the pre-chamber opens the possibility of reviewing current tumble generation strategy at the cost volumetric efficiency or exhaust back pressure. To demonstrate the influence of exhaust back pressure, a test was conducted at 6000 rpm full-load by reducing the exhaust back pressure from 1.9 Bar to 1.3 Bar and combustion stability and performance were observed to improve with lower back pressure, as shown in the Table.7.2. Even if tumble flow field is less effective for turbulent combustion with the pre-chamber, changing air flow field can change air guided spray formation including pre-chamber enrichment. So when cylinder aerodynamics is reviewed for pre-chamber combustion, spray formation must be considered.

Exh. pressure (Bar)	CoV(IMEP$_g$)	CoV(Pmax)	Pmax	ISFC
1.9	2.1	5.9	157.4	193.2
1.3	1.6	4.3	166.2	191.7

Table 7.2: Impact of back pressure on performance, 6000 rpm, ignition angle: 19.5º BTDC.

Instantaneous heat release rate is calculated from measured cylinder pressure and using first law of thermodynamics with variable poly-tropic coefficients. Instantaneous heat release rate and integrated heat release results are shown in Fig. 7.7. With the pre-chamber ignition, maximum heat release rate is substantially higher

(a) 6000 rpm

(b) 7500 rpm
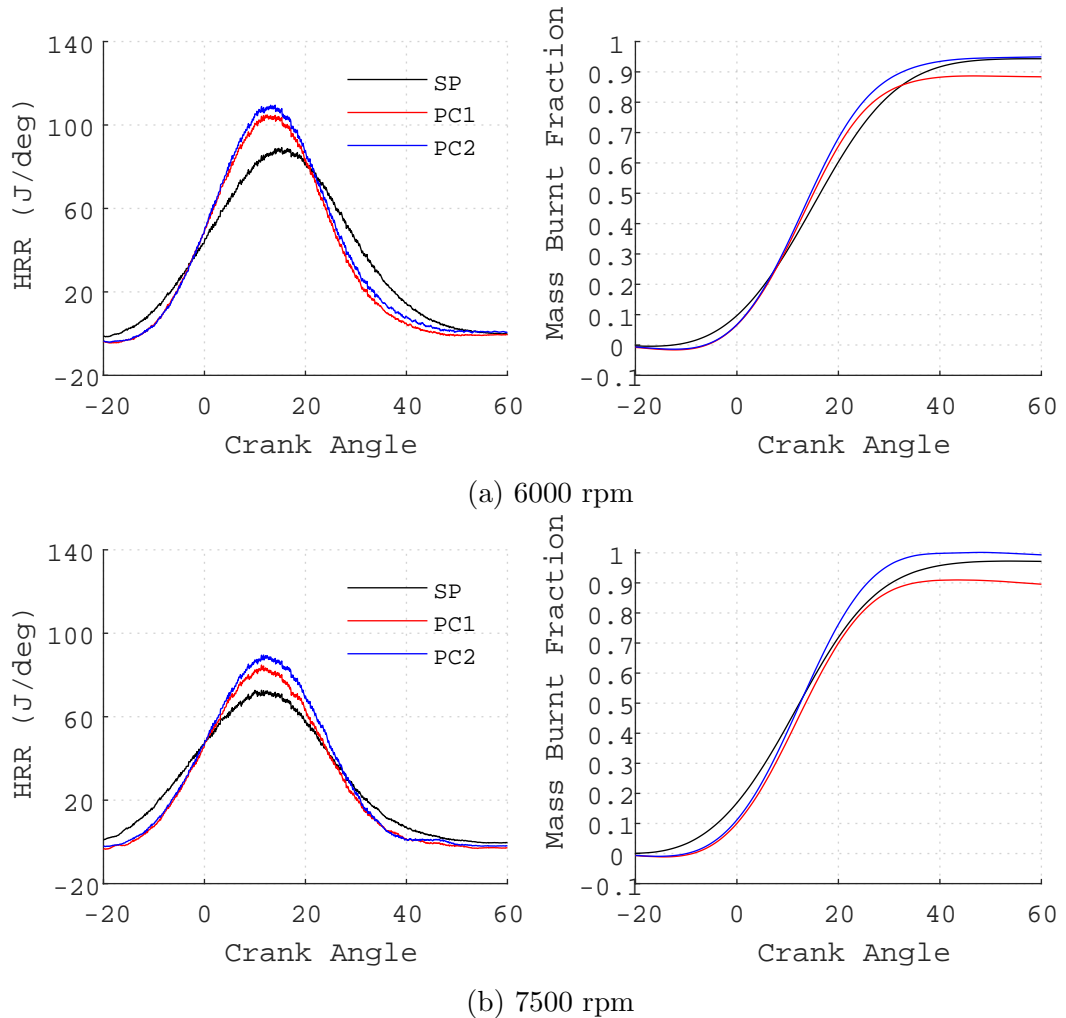
Figure 7.7: Instantaneous and mass burnt fraction, based on average of 100 cycles. Mass burn fraction is calculated by normalising integrated heat release with fuel energy supplied. Fuel energy= mass of fuel injected per cycle × Lower Calorific Value.

and integrated heat release data also shows the shortened burn duration. For lean burn combustion with relative AFR in the range of 1 to 1.4, combustion efficiency is close to unity [5]. Also, there were no misfire cycles or much delayed combustion observed with pre-chamber, showing combustion is completed well before the exhaust valve opens at 120º CA ATDC. So, the difference between fuel energy supplied and

energy released (apparent net heat release calculated from the pressure data) inside the cylinder is mainly from the heat transfer to the walls. With PC1, net heat release is lower for the same fuel energy supplied, indicates higher heat transfer losses. For PC2, tail end of combustion is influenced by pressure oscillations and net heat release rate appears to be over predicted at 7500 rpm. So the drop in net heat release is not visible with PC2 design, though heat transfer loss to coolant and oil found to be identical to the base spark ignition data. Even with PC1, coolant outlet temperature was observed to be identical to the base data. Due to high thermal conductivity of pre-chamber construction material (CuBe), heat is dissipated directly to ambient air, as visible in temperature variation shown in Fig. 5.23. Also, Copper based spark plug washer initially used for mounting the spark plug on the pre-chamber melted and fused to pre-chamber, before it was replaced with steel washers, shows increased heat transfer along the pre-chamber body and then to air. Calculated cylinder temperature is shown in Fig. 7.8 and with pre-chamber combustion peak temperature was observed to be high, also contributing to increased heat transfer. As PC1 has higher surface area and more number of nozzles, the combined

(a) 6000 rpm   (b) 7500 rpm
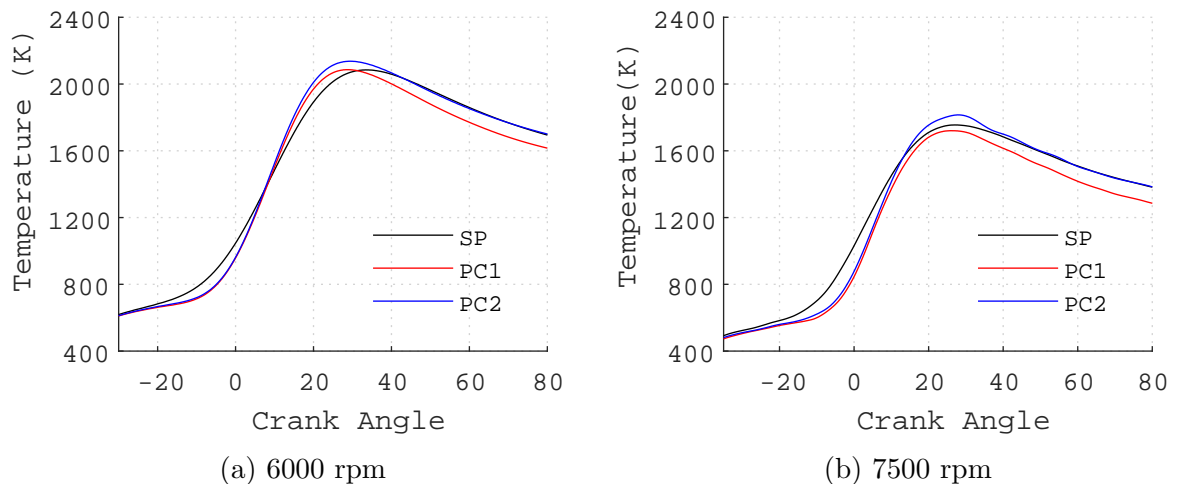
Figure 7.8: In-cylinder temperature comparison based on average of 100 cycles.

effect of surface area and cylinder temperature is resulting in increased heat transfer to the wall. The reason for reduced IMEP$_g$ observed with the PC1 can be concluded as the result of increased heat transfer loss.

Pre-ignition

As already mentioned for the pre-chamber tests, ignition timing was retarded from KLSA ignition timing to run the engine with minimum knock events, because of the absence of a live knock detection system. Test attempts were made to move closer to KLSA ignition timing, but resulted in run-away knock and pre-ignition. For PC2 and at 6000 rpm, test run with 1º ignition advance from the finalised

ignition timing resulted in pre-ignition event as shown in Fig. 7.9. A pre-ignition event is identified by earlier heat release and resultant pressure rise, even before the ignition event. This pre-ignition event is unusual because the previous cycle was not a knocking cycle and hence is not a result of run-away knock. This pre-ignition indicates the presence of a hot spot inside the combustion chamber. Based on the CHT analysis discussed in the §5.3, highest temperature was observed at the pre-chamber tip area. Though, a CuBe sleeve was added to improve heat transfer, it was not adequate enough to dissipate heat from the pre-chamber tip area. So even with a live knock detection system, there is a chance for pre-ignition and further design improvement is required to aid heat transfer from the pre-chamber tip area. One option could be to modify the water jacket design to make pre-chamber mounting sleeve water cooled.
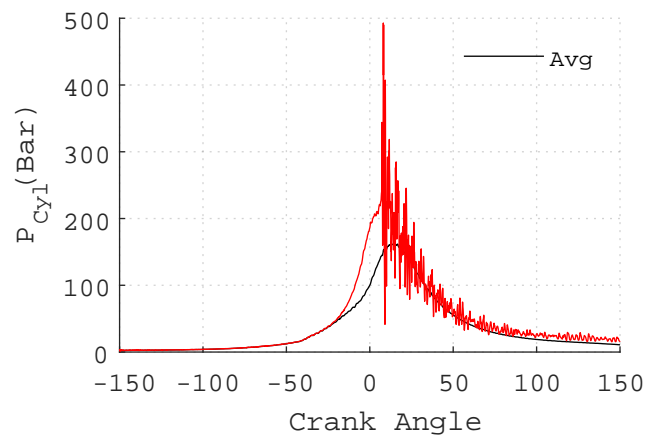
Figure 7.9: Pre-ignition cycle comparison with average of 100 cycle. PC2, 6000 rpm, Ignition time= 21º BTDC

7.3 Pre-chamber evaluation for higher dilution

Tests continued by increasing λ up to 1.4. For a turbo-charged engine running with restricted fuel flow, dilution is increased by adding more air in to the engine and this higher airflow is achieved by increasing manifold pressure. A higher manifold pressure requires closing of exhaust waste gate valve to direct more exhaust gas to the turbine and can see an increase in back pressure. For the single cylinder engine, higher lean test cases were run with increased back pressure by closing exhaust back pressure valve. Here the same base turbo charger was assumed for the back pressure calculation in 1D model. Once an optimum λ is identified, it is possible to select a different turbine/compressor map suitable for changed air flow and then back pressure can be reduced, but is not considered in this study. Dilution study was conducted only for 7500 rpm as 6000 rpm requires much higher manifold pressure

and was not possible to achieve from the boost rig with only one supercharger connected. Variation of ISFC with dilution is shown in Fig. 7.10.

(a) ISFC variation

(b) Standard deviation of combustion start
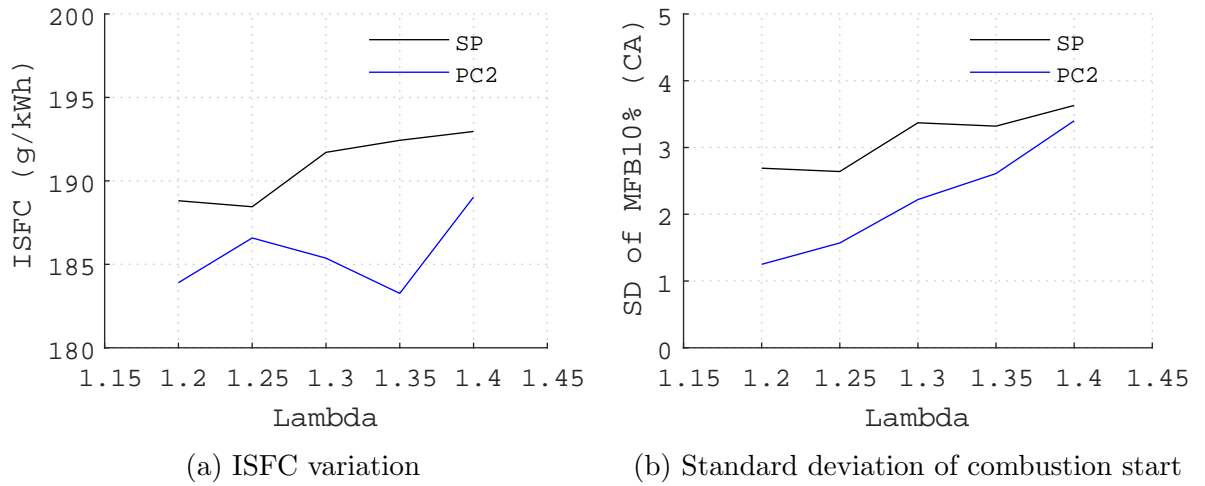
Figure 7.10: Pre-chamber performance with increased dilution

Pre-chamber combustion did show similar gains at higher lean limit over spark ignition, though it didn't extend the lean limit from λ of 1.2 for the engine in tested condition. With higher dilution, main chamber combustion become even slower and ignition timing had to advance to achieve MFB50% anchor angle close to 12, to achieve the MBT ignition timing. For λ=1.4, ignition timing was advanced by almost 20º compared to λ=1.2, as shown in Fig. 7.11b. Pre-chamber scavenging happening during late compression stroke. CFD results for variation of λ within the pre-chamber and near the spark plug is shown in Fig. 7.11a. In this case, fuel

(a) λ inside the pre-chamber and near the spark plug (CFD results)

(b) Ignition timing
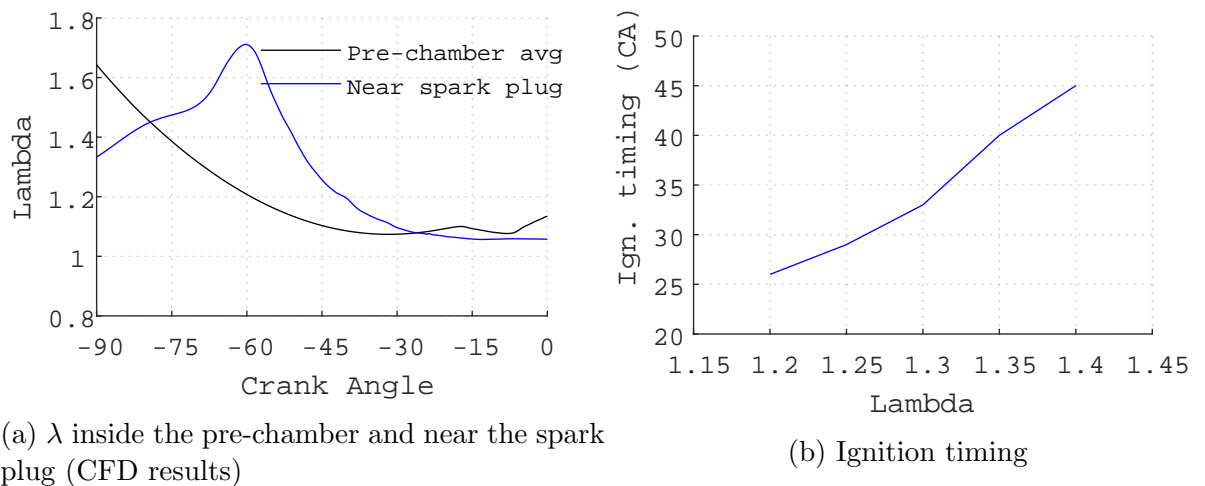
Figure 7.11

injection started at 310º CA BTDC and ends at 205º CA BTDC. As discussed in §5.2.2, pre-chamber enrichment and scavenging happens when the pressure difference between main chamber and pre-chamber is substantial, during compression

stroke. As in-cylinder fuel mixing results in a stratified state as previously shown in Fig. 5.3, fuel enrichment achieves a lowest λ value around 30° BTDC, and then further starts to increase. Whereas fuel-mixture state near the spark plug shows slightly different behaviour as shown in Fig. 7.11a, with all residual gases initially move towards the spark plug during late compression stage, resulting high λ values at around 60° CA BTDC, and then starts to decreasing as it approaches TDC. Scavenging near the spark plug completes after 30° BTDC. So, with this mixture formation, it is ideal to keep ignition angle after 30° CA BTDC. Further Advancing ignition timing will result in burning lean mixture inside the pre-chamber. Hence, earlier ignition timing results in high variation in combustion start as observed in the testing, shown in Fig. 7.10b. So it is crucial to keep ignition timing close to TDC and one way of achieving the same is to increase the compression ratio so that ignition timing is decided by KLSA. Both compression ratio and lean limit to be considered together and it requires an extensive study considering turbine/compressor maps for optimum back pressure to achieve target air flow, piston design for increased compression ratio and revised port geometry.

7.4 Pre-chamber evaluation for higher compression ratio

Both PC2 pre-chamber and spark plugs were evaluated on cylinder 5 with compression ratio of 15. This higher compression ratio was achieved by removing the bowl profile from the base piston and thus making a flat piston and all other design features of the combustion chamber were kept the same. It is key to note that this engine has air guided mixture formation and changing piston shape can have influence on mixture formation. Cylinder pressure comparison is shown in Fig. 7.12. The change in peak cylinder pressure values are observed to be higher at CR 15 with clear change is visible at 7500 rpm compared to CR 14 results. Heat release rate comparison is shown in Fig. 7.13. Ignition delay and burn duration is shown in Fig. 7.14. Results show that pre-chamber is able to reproduce the gain at a higher compression ratio as well.

7.5 Correlation of prediction to measurement

To validate the pre-chamber CFD models, simulated results were compared with the pre-chamber test results. Two cases which achieved correlation and another case which couldn't obtain good correlation are shown in Fig. 7.15, Fig. 7.16 and in Fig. 7.17 respectively. For PC2, CFD model achieved good correlation to the mea-
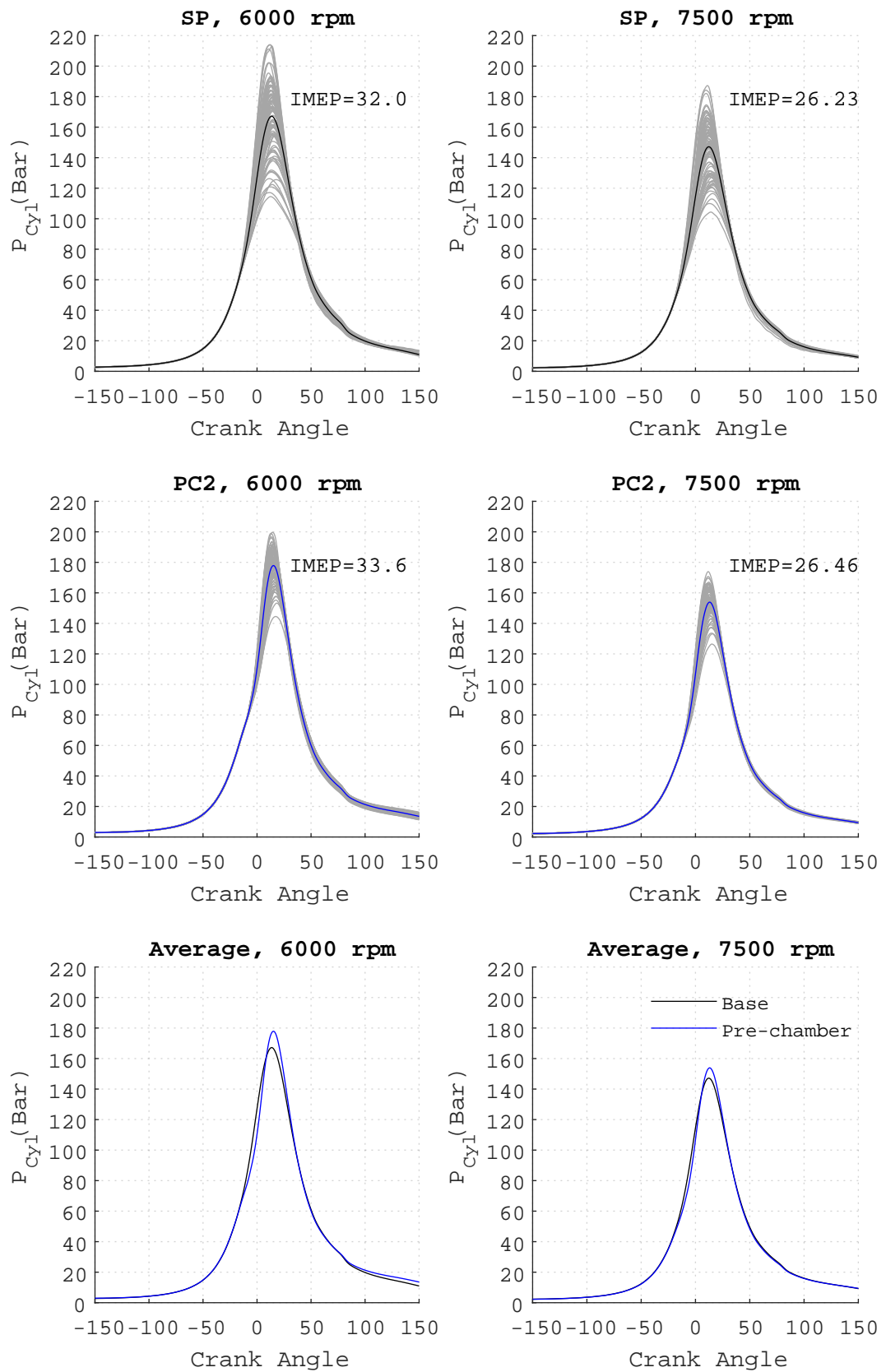
Figure 7.12: Cylinder pressure comparison for spark plug and two pre-chamber designs, 100 cycles data with average pressure curve.

(a) 6000 rpm

(b) 7500 rpm
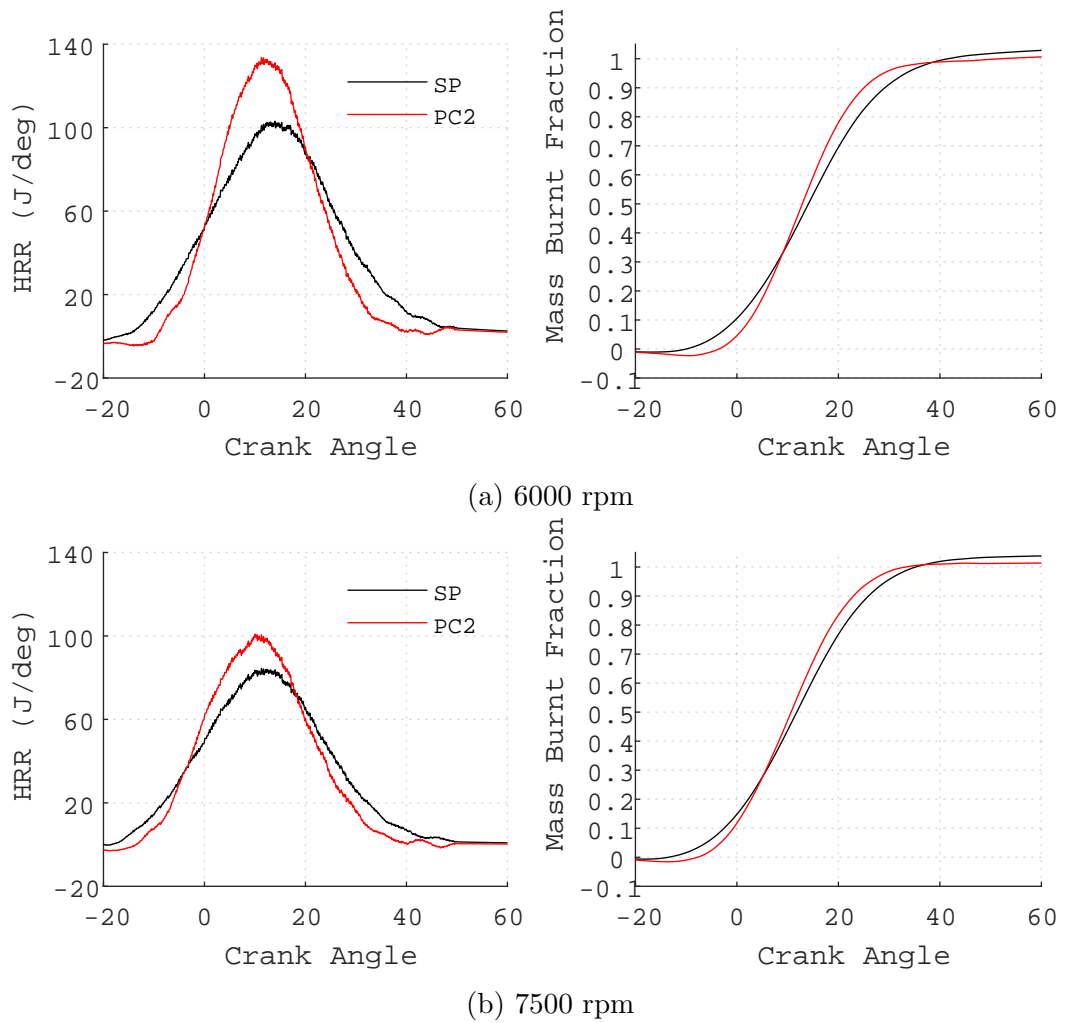
Figure 7.13: Instantaneous and mass burnt fraction for CR 15, based on average of 100 cycles.
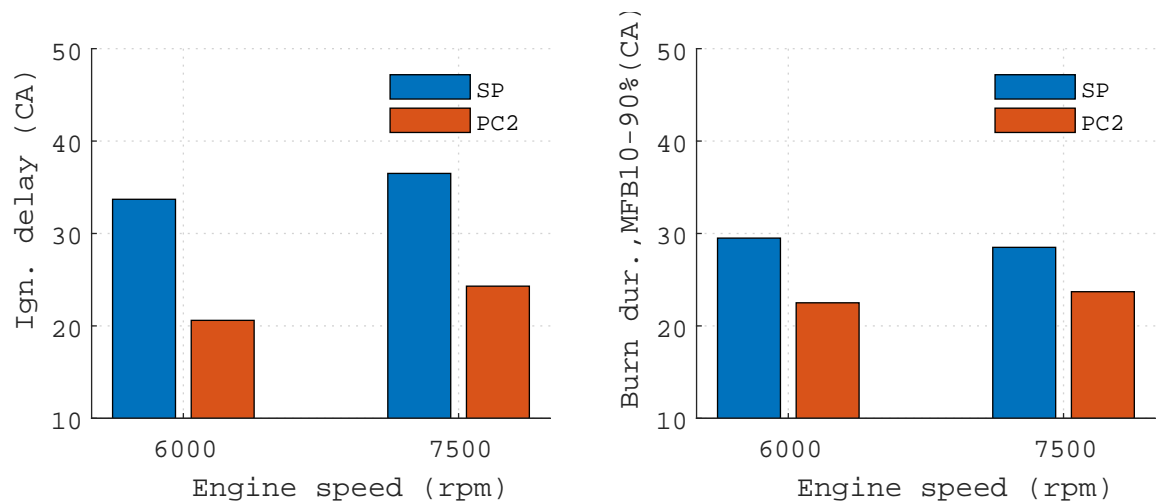
Figure 7.14: Ignition delay and burn duration comparison for CR 15

sured average pressure data. The small discrepancies are attributed to the mismatch of combustion phasing. It is key to note that with a RANS based CFD model, it is difficult to identify ignition timing corresponding to KLSA operating point and to
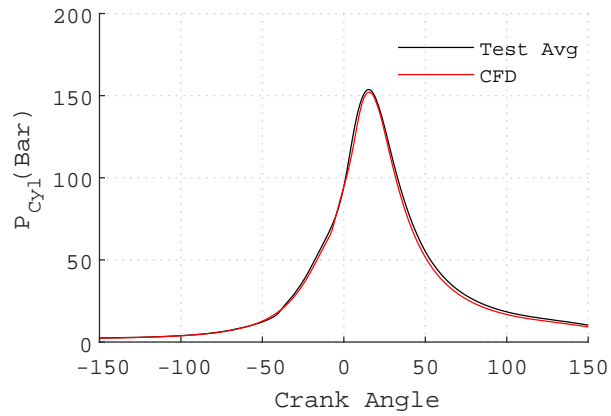
Figure 7.15: Correlation of test and CFD results for PC 2, 6000 rpm
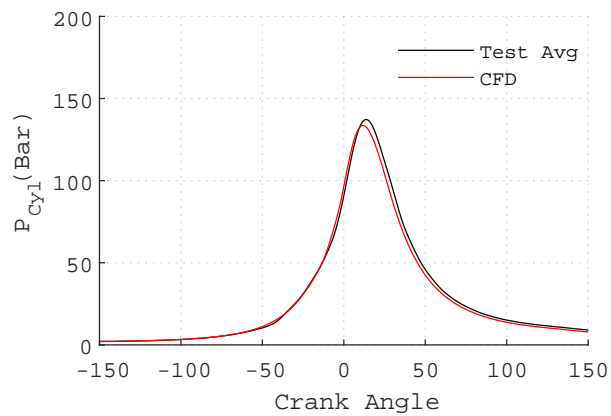
Figure 7.16: Correlation of test and CFD results for PC 2, 7500 rpm
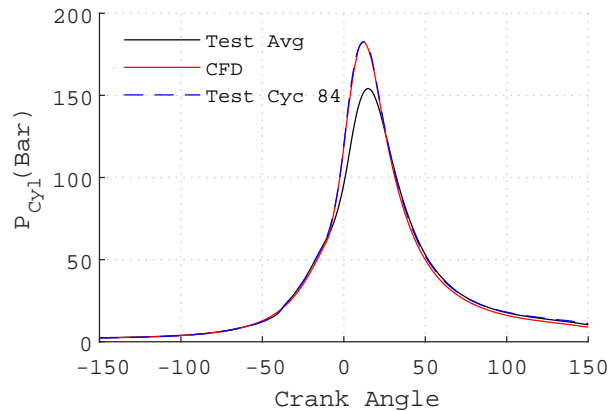
Figure 7.17: Correlation of test and CFD results for pre-chamber design option 1, 6000 rpm. A single measured cycle is shown as Test Cyc 84.

make exact prediction on performance (IMEP$_g$). Because, when engine is running at KLSA, a knocking cycle is an extreme variation of the pressure curve, mainly attributed to the lowest ignition delay compared to the other cycles and a RANS model is expected give a pressure curve close to the average pressure curve. So, a CFD model is more useful in predicting the performance of different designs with same ignition timing.

For PC1, CFD model over predicts the pressure curve. Higher peak pressure observed with the large volume pre-chamber was not reproduced in the test. This deviation indicates that the CFD model was not able to reproduce the combustion instability associated with lean mixture inside the pre-chamber, observed with the large volume pre-chamber. The spark ignition model used in the CFD model ensured combustion start even with lean mixture and more accurate spark ignition models are required to account for unstable combustion start. Spark plug sees different mixture state between the base engine and with the pre-chamber, where mixture state near the spark plug tip is leaner and has more residuals. For such challenging conditions, the energy deposition based spark ignition models are not truly predictive, due to assumptions involved in this model [78]. Scarcelli et al. proposed a hybrid Lagrangian-Eulerian spark ignition model for the operating conditions that pose a challenge for the ignition success and flame propagation [78]. Alternatively, assessment can be made on combustion stability by looking at the mixture state inside the pre-chamber and near the spark plug. Though average pressure curve was found to have a higher deviation, there were individual test cycles matching to the predicted pressure curve as shown in the same Fig. 7.17 and it shows that the predicted pressure curve is realizable if combustion stability can be achieved by having rich mixture inside the pre-chamber.

7.6 Summary

In this chapter, performance of two pre-chamber designs were compared with spark ignition combustion and a design (0.8 cc volume, 4 nozzles, 1.5 nozzle diameter) is proposed for final implementation. Pre-chamber ignition system is able to report substantial reduction in burn duration and cyclic variation. For the base combustion chamber design with CR 14, the gain in $IMEP_g$ is 3.6% and 5.4 units reduction in ISFC at 6000 rpm. The gain is limited due to following reasons:

- Testing conducted at a reduced fuel flow rate due to boost rig failure and spark ignition itself worked well with reduced cylinder loading and achieved close to MBT ignition angles.

- With pre-chamber ignition, KLSA was not achieved due to the absence of live knock detection system.

Though cyclic variation was reduced substantially, lean limit was not extended from the base lambda of 1.2 tested. This is because, tests are conducted at 7500 rpm, where MBT ignition timing is achieved and leaner mixture requires ignition advance

to maintain MFB50% angle same as the base level, which results in pre-chamber ignition before pre-chamber enrichment.

Chapter 8

Engine Knock Analysis

Contents

8.1   Background

With the pre-chamber ignition system, knock level measured by the knock sensor was observed to be very high and uneven compared to the base spark ignition level, as shown in Fig. 8.1. With the pre-chamber ignition, the high-pass filtered cylinder pressure data shows knock like distinct peaks between 10 to 0 deg before TDC (Fig. 8.2). These peaks are happening even before MFB10% point and hence cannot be associated to end gas auto-ignition. There is another peak observed immediately after TDC with increased amplitude. CFD results show that jets exit from the pre-chamber between 10 to 0 degree before TDC. Numerical study also shows local jet velocity reaching Mach 1 inside the nozzle when the jet comes out of the pre-chamber, as shown in Fig. 8.3. So, it can be concluded that pre-chamber jet flow is producing high frequency pressure oscillations as result of the jet reaching sonic velocity. These jet induced shock waves and its reflections excite the structure just like normal knock induced shock waves do and these signals detected as knock signal by the knock sensor. So, these additional high frequency vibrations make it difficult to use a transducer based knock sensor for its intended purpose.
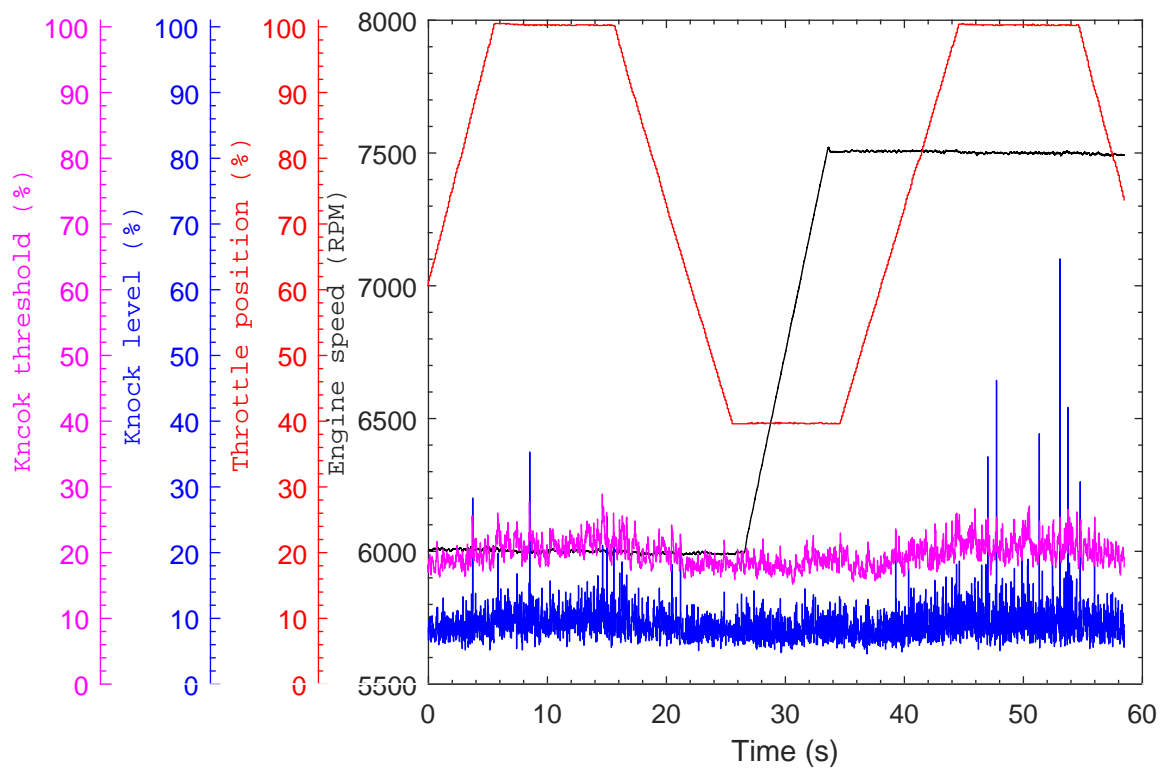
(a) Base
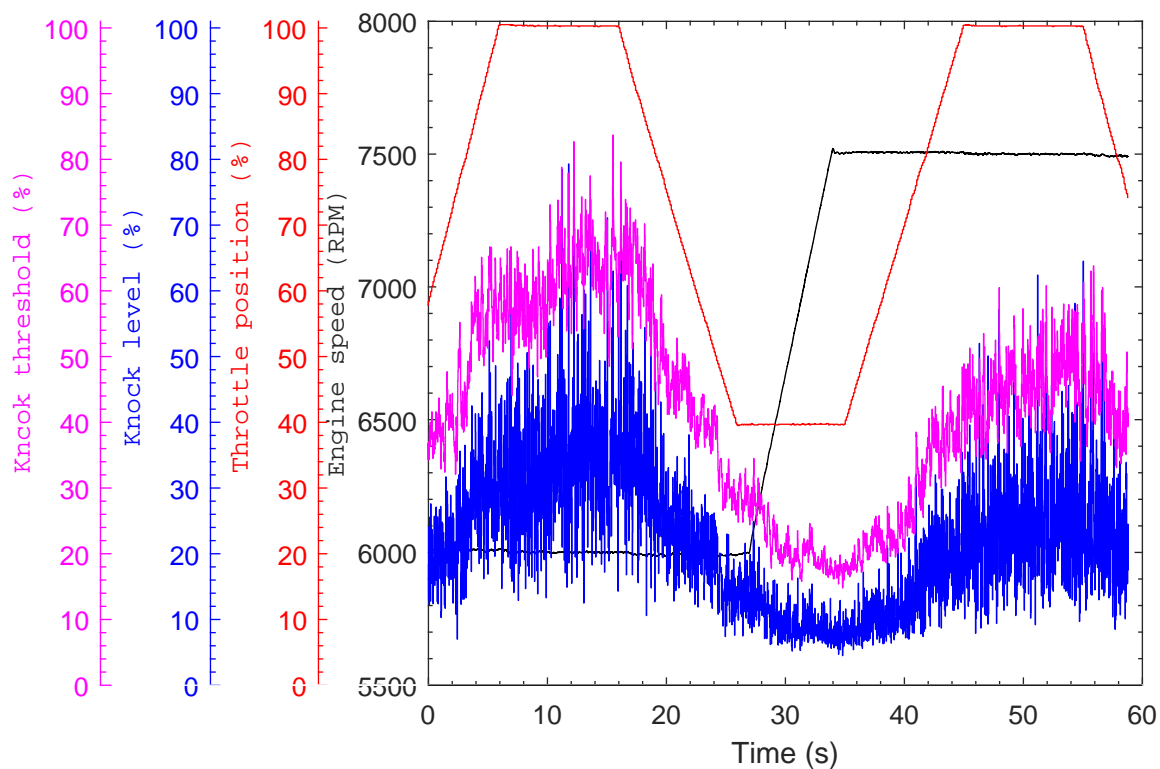
(b) PC

Figure 8.1: Knock level and threshold against engine speed and throttle position.

(a) Base, 6000 rpm

(b) Base, 7500 rpm

(c) PC1, 6000 rpm

(d) PC1, 7500 rpm

(e) PC2, 6000 rpm

(f) PC2, 7500 rpm
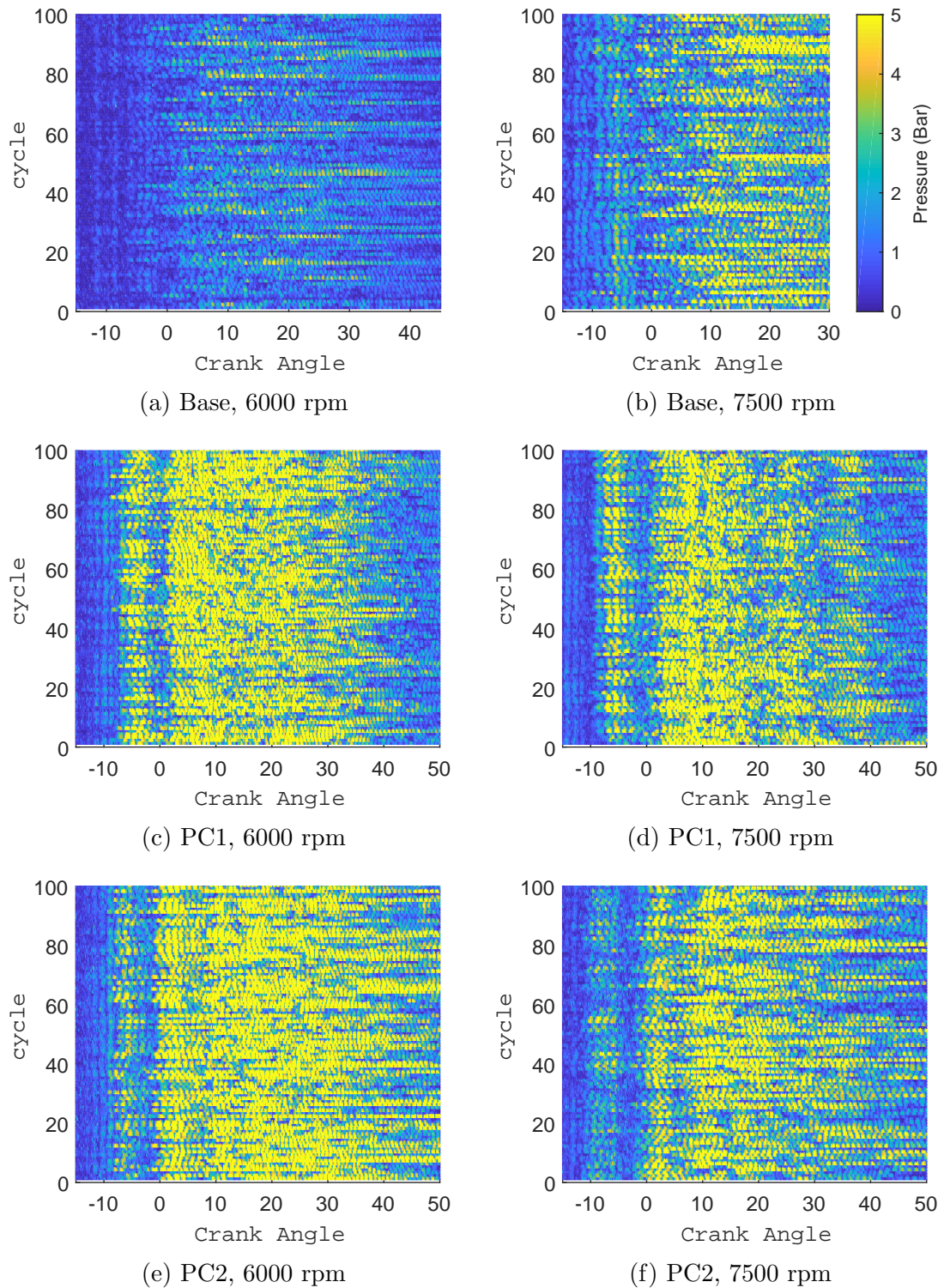
Figure 8.2: Knock pressure calculated by high pass filtering (Mean Value Filter) of measured in-cylinder pressure data for 100 cycles.

Jet produced oscillations are observed to be higher at 6000 rpm, as shown in Fig. 8.4. Average operating pressure during compression stroke at 6000 rpm is higher compared to 7500 rpm (Fig. 8.5), and resulting in less charge entering the pre-chamber and resultant reduced charge burning inside the pre-chamber. The peak pressure produced inside the pre-chamber is a function of charge burned inside
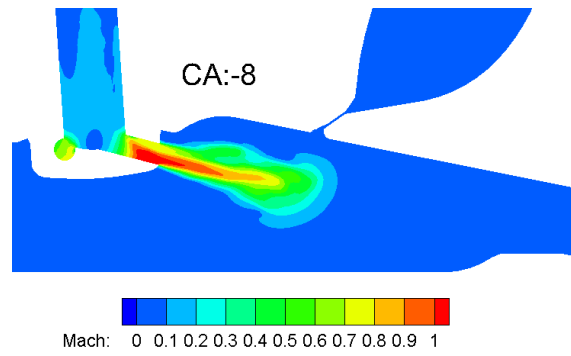
Figure 8.3: Variation of Mach number when the jet comes out of the pre-chamber, with local flow velocity inside the nozzle crossing Mach 1, resulting in shock waves inside the combustion chamber.

(a) PC1, 6000 rpm

(b) PC1, 7500 rpm

(c) PC2, 6000 rpm
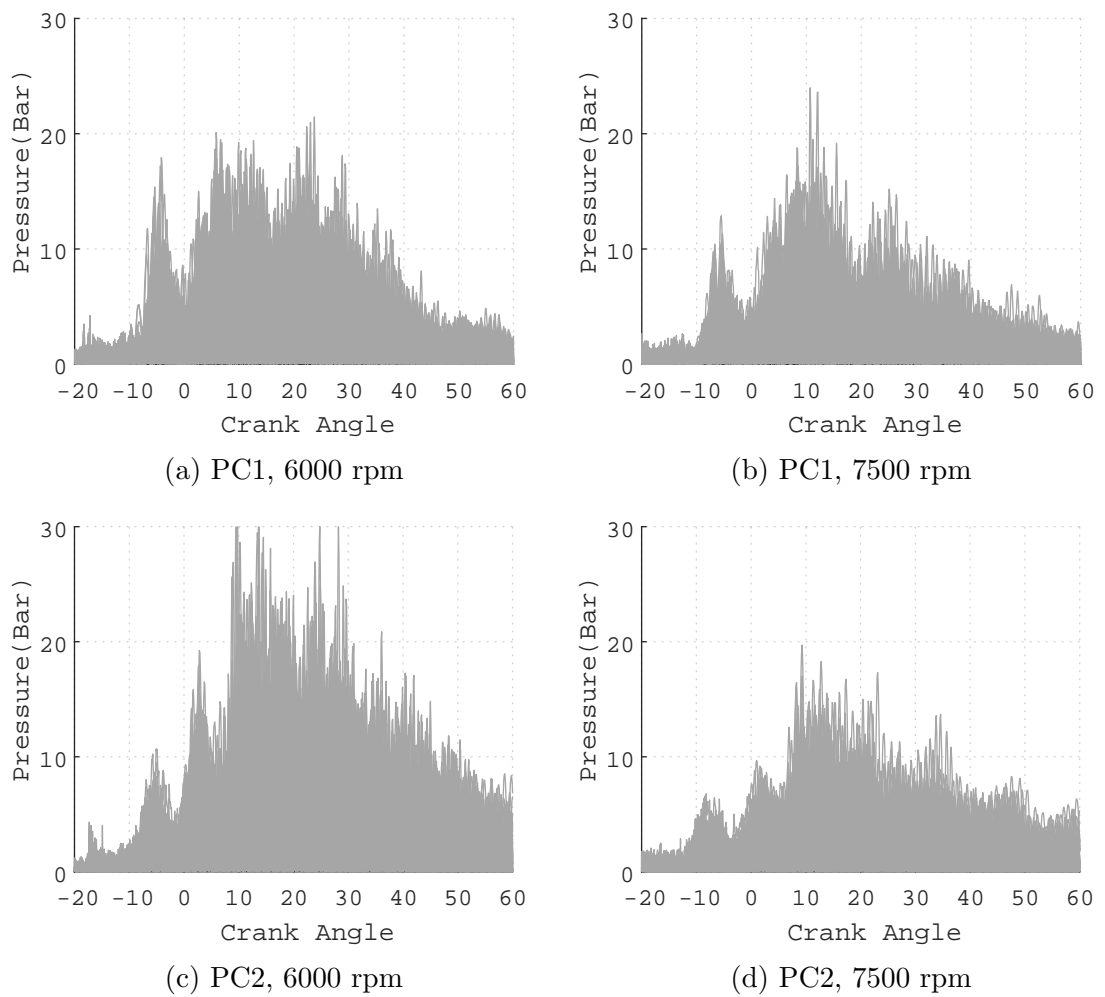
(d) PC2, 7500 rpm

Figure 8.4: Comparison of high pass filtered pressure signals (mean value filter) for PC1 and PC2. 100 cycles data

the pre-chamber and hence peak pressure observed to be lower at 7500 rpm. The reduced pre-chamber peak pressure results in reduced pressure difference across the chambers and resulting in lower jet velocities.
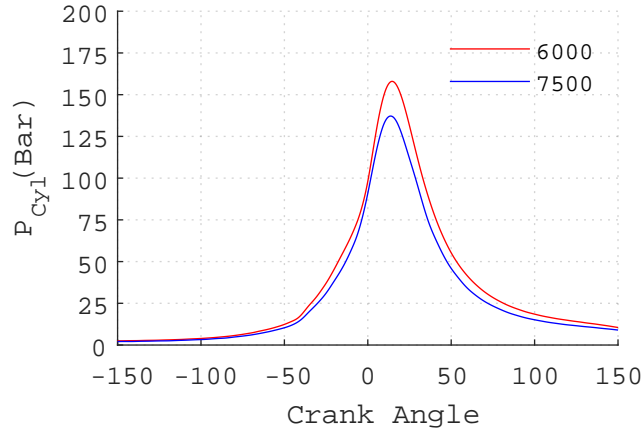
Figure 8.5: Measured average cylinder pressure comparison for pre-chamber combustion at different engine speeds.

8.2   Cylinder pressure based knock detection

In this section, an alternate knock detection strategy based on instantaneous cylinder pressure is investigated to address the problem of difficulty in detecting engine knock with a transducer based knock sensor. Cylinder pressure based knock detection is already used in motor-sports engines for accurate prediction of knock [79], [80]. As a motor-sport engine normally operates at higher engine speeds, the signal to noise ratio is low and makes it difficult to use a transducer based sensor. This section reviews different cylinder pressure based knock parameters previously proposed by researchers and investigated how these methods are working with pre-chamber combustion.

8.2.1   MAPO, IMPO and DKI

One of the earliest and most used pressure based knock indicator is the maximum amplitude of pressure oscillations (MAPO). MAPO is defined as the peak of pressure oscillations due to knock ([81],[76], [82]). The crank angle resolved pressure signal is high pass filtered to get oscillations and has to be compared with a threshold to define a knocking cycle. Another equally popular knock index is integral of modulus of pressure oscillations (IMPO), initially proposed by Arrigoni [83]. IMPO is a way to represent the energy contained in the high frequency oscillations of the measured pressure signal. A threshold has to be identified for IMPO as well to define a knocking cycle. Both MAPO and IMPO have dimensions and Brecq et al. proposed a dimensionless knock indicator (DKI) based on both MAPO and IMPO [84]. MAPO, IMPO and DKI for one cycle is given by

$$MAPO = |P_{hp}| \tag{8.1}$$

$$IMPO = \int_0^W |P_{hp}| d\theta \tag{8.2}$$

$$DKI = \frac{IMPO}{MAPO \times W} \tag{8.3}$$

Where P_{hp} is high pass filtered pressure signal and W is the measuring window in crank angle degrees. DKI can be interpreted as ratio of two areas: First, IMPO is the area under high pass filtered pressure signals and the second term, MAPO×W is the area of computational window [84]. A knocking cycle results in a lower DKI value. By virtue of this definition, DKI has the potential to work better when the signal noise is high. MAPO, IMPO and DKI are calculated for 100 continues cycles and for a measuring window of 40º CA for both ignition system and are shown in Fig. 8.6 and Fig. 8.7. The measuring window starts from TDC_{firing} and this window is same as what was used for the knock sensor. Attempts were made to delay the start of measuring window, for example: 5º CA $ATDC_{firing}$, to avoid the influence of jet induced oscillations from knock detection, but it was found that knock onset is also happening as early as 5º CA $ATDC_{firing}$, and hence there is a risk of missing a knock event with such a delayed measuring window.

Both MAPO and IMPO are able to distinguish knocking cycles accurately for spark ignition combustion. For pre-chamber ignition, MAPO and IMPO are influenced by the jet oscillations and these indicators are over predicting the knock. It is worth to mention that with the pre-chamber ignition, KLSA was not achieved and knocking events were not expected. For both ignition systems, DKI doesn't give an accurate prediction of knocking cycle.
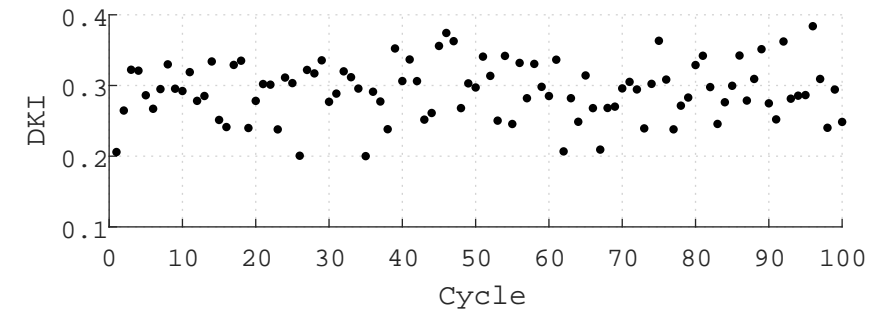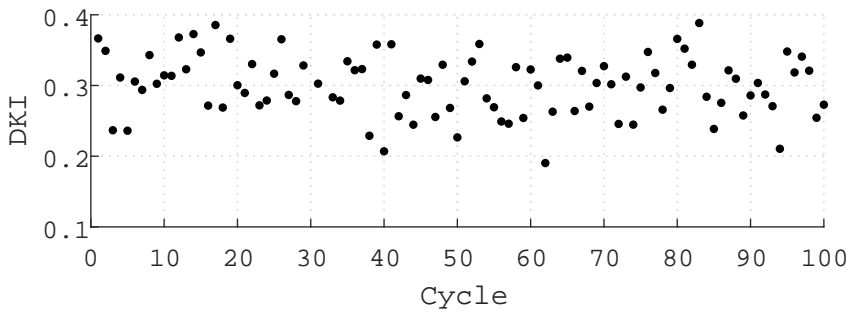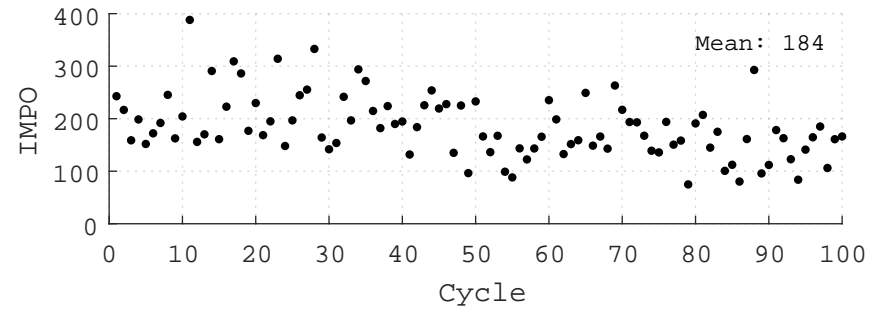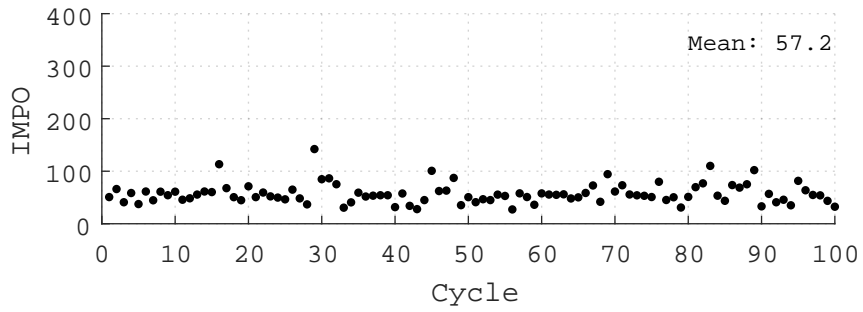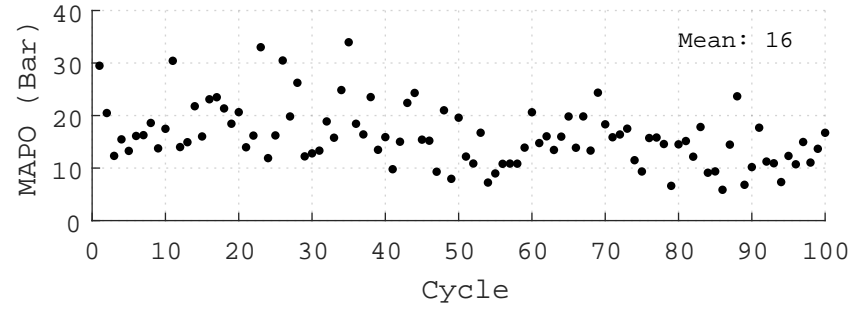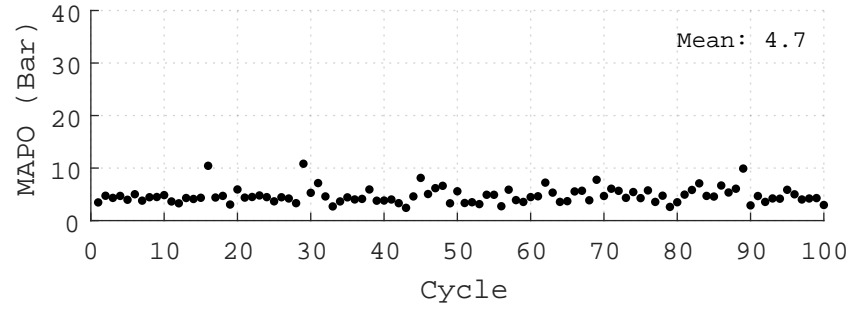
(a) Base

(b) PC2

Figure 8.6: MAPO, IMPO and DKI at 6000 rpm
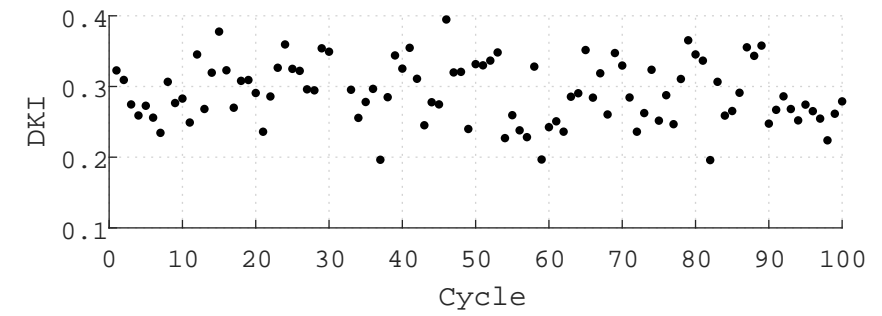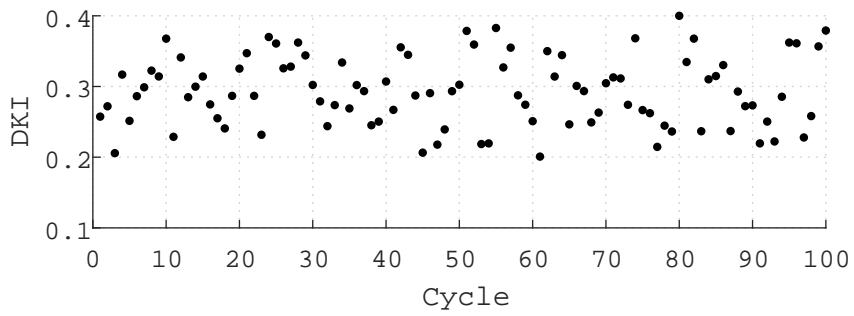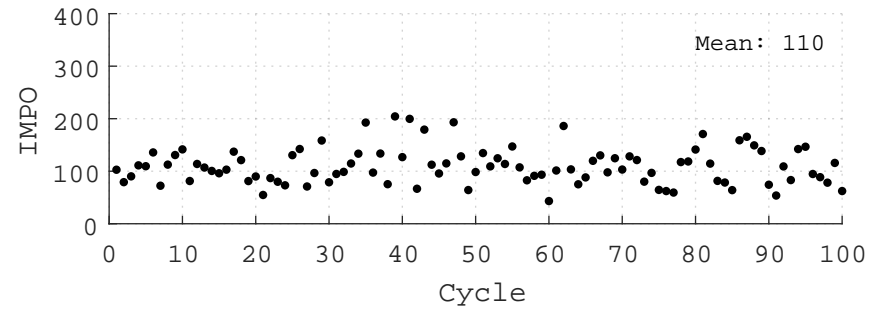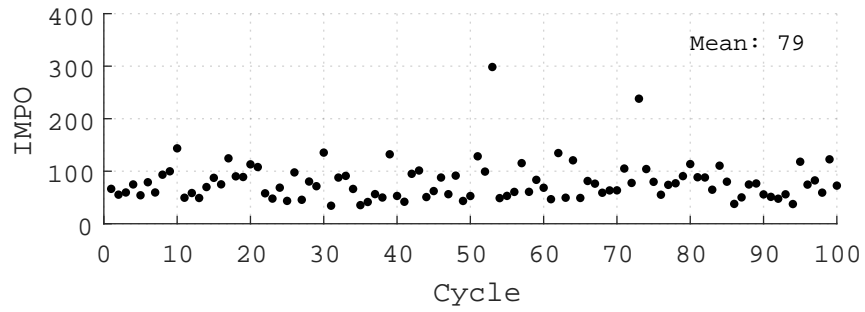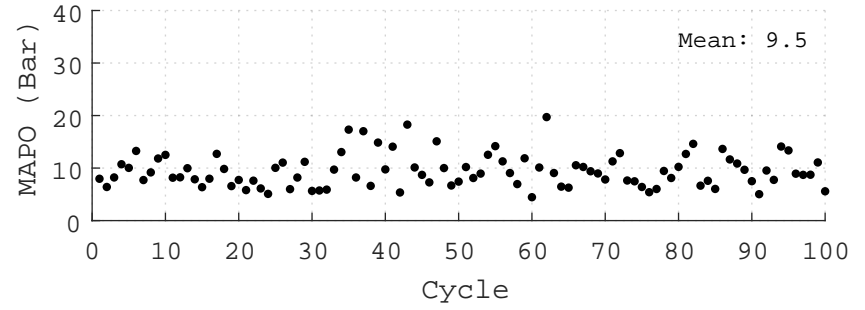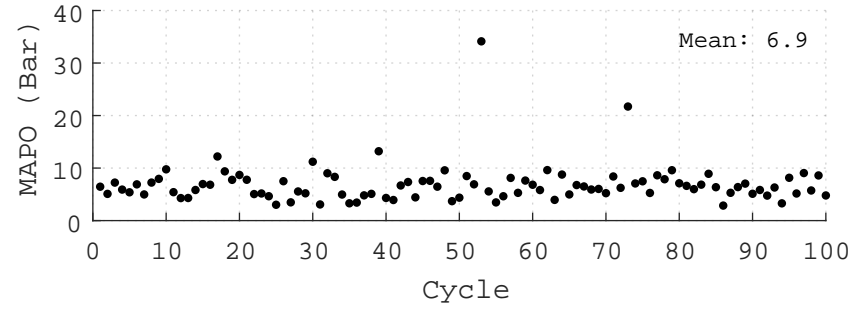
(a) Base

(b) PC2

Figure 8.7: MAPO, IMPO and DKI at 7500 rpm

8.2.2 LKI

A logarithmic based knock indicator is formulated based on the findings by Hudson et al.[85] as given in Eq. 8.4.

$$LKI = ln\left(C \times \frac{\sum_n P_{hp}^2(n)}{n}\right) \tag{8.4}$$

The constant C can be tuned to make a knocking event have a positive value. The value of mean LKI can be used to advance ignition time to ensure operating point is close to KLSA. n is the number of samples in the measuring window. For same constant C, LKI is also over predicting the knock level with the pre-chamber ignition as shown in Fig. 8.8.

The reason for discussing all above cylinder pressure based knock detection methods, despite these methods failed to capture low knock level associated with pre-chamber combustion is to emphasise the difficulty of knock prediction with pre-chamber ignition system. Also, some of these methods including MAPO and IMPO can be used for knock detection by changing some of the settings like measuring window and filtering frequency. It is worth to mention that when the jets come out of the pre-chamber, cylinder temperature is much lower compared to end gas auto-ignition state, where cylinder temperature is much higher. Cylinder temperature decides the sound velocity and frequency of pressure oscillations. So, there is a possibility for segregating pre-chamber jet induced pressure oscillations from end gas auto-ignition. Oscillation frequencies calculated based on cylinder temperature before and after combustion and in the radial direction results in difference of 1.5kHz. It requires further analysis to understand whether this difference is sufficient enough to segregate knocking oscillations from jet oscillations in actual testing conditions. But no further work was done on this direction because the objective was to use same knock detection method for both spark ignition and pre-chamber ignition.
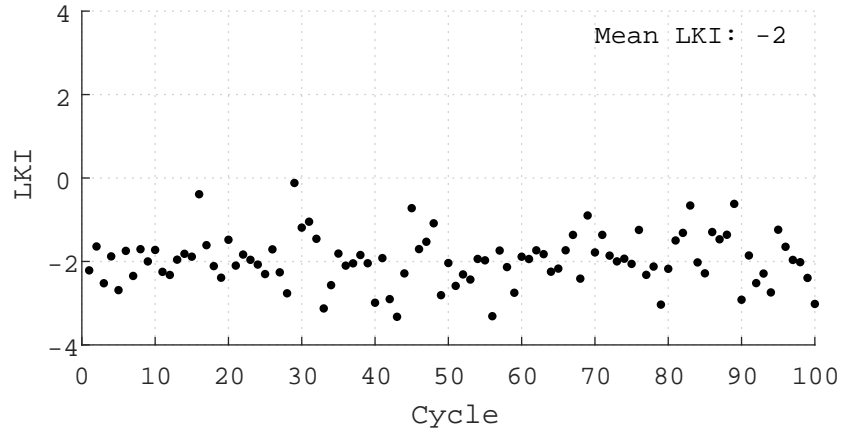
(a) Base, 6000 rpm
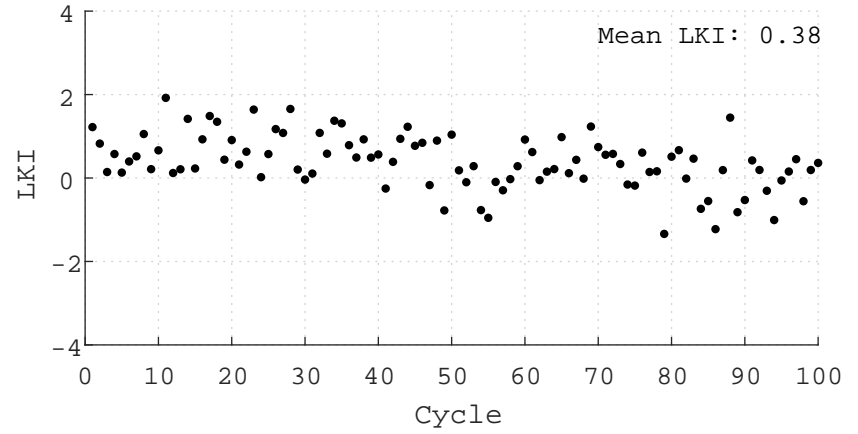
(b) PC2, 6000 rpm
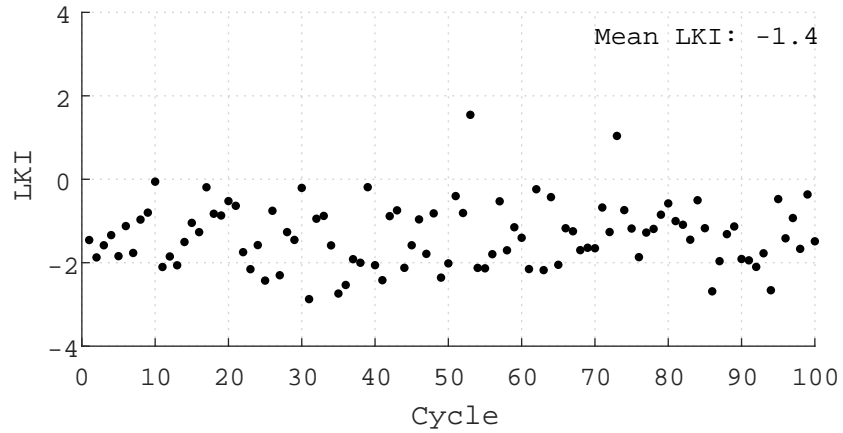
(c) Base, 7500 rpm
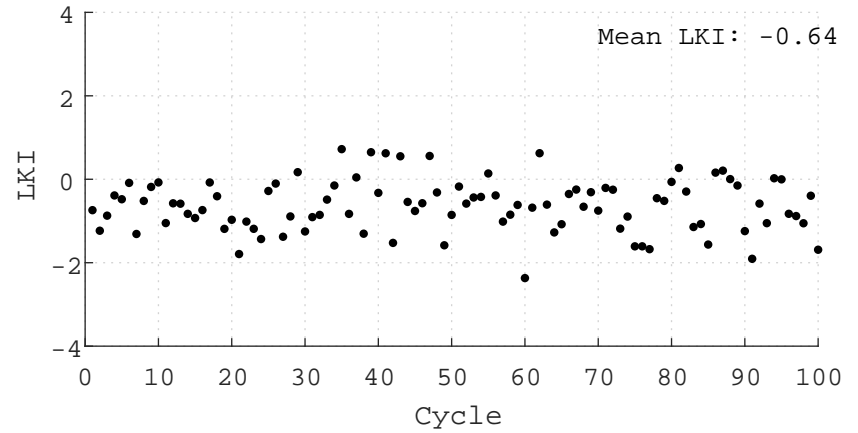
(d) PC2, 7500 rpm

Figure 8.8: Logarithmic Knock Index (LKI) results

(a) 100 cycles data with average heat release   (b) Knocking cycle, cycle:60
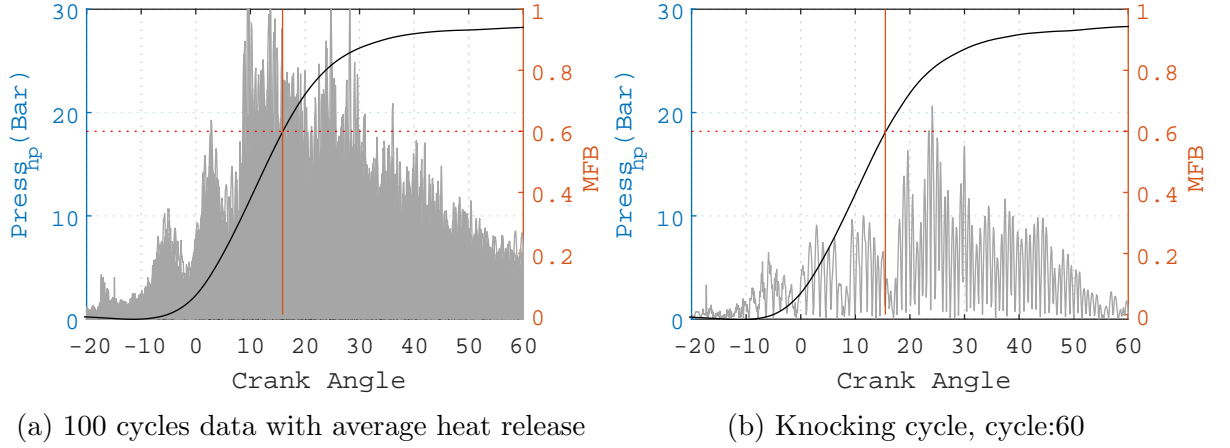
Figure 8.9: Heat release and pressure oscillations, PC2, 6000 rpm

8.2.3   KI2

This dynamic knock detection method proposed by Galloni [86] is capable of resolving knock intensity on a cycle by cycle case without defining a pre-determined threshold. This method benefit from the fact that the fastest combustion cycle results in higher pressure oscillations and knock. In this method, whole combustion event is divided in to two phases. A knock threshold ($\mathrm{Mapo_{th,j}}$)is defined based on the maximum pressure oscillation in the first phase of combustion.

$$Mapo_{th,j} = k.max(P_{knock,j}(\theta)|_{SA}^{\theta_{60\%}}) \tag{8.5}$$

Where k is a constant and taken as 2 for this study. The maximum oscillation in the second phase is compared to the threshold calculated in the first phase to define the knock intensity as follows:

$$I2_j = \frac{max\left[(P_{knock,j}(\theta)|_{\theta_{60\%}}^{\theta_{99\%}} - Mapo_{th,j}), 0\right]}{Mapo_{th,j}} \tag{8.6}$$

This method looks for a knock event only after 60% charge is burned and that too based on comparing with a dynamic threshold defined for that particular cycle. Heat release calculation was done on a low-pass filtered signal and jet oscillation has no influence on this calculation. Amplitude of jet oscillations contribute to defining the dynamic threshold level and otherwise has no effect on deciding a knocking cycle. As already discussed, amplitude of jet oscillations is a function of cylinder loading and it helps in capturing a knock event with varying engine loading, without any tuning. It is worth to mention that amplitude of knock pressure oscillations also increases with cylinder loading. A graphical explanation for how this method works is shown in Fig. 8.9. The knock intensity at an operating point has been calculated

using the following equation:

$$KI2\% = \frac{\sum_{j=1}^{N_{cyc}} I2_j}{N_{cyc}}.100 \tag{8.7}$$

Now KLSA can be achieved by operating within a range of KI2, the lower limit representing knock free and higher limit representing maximum allowable knock. Fig. 8.10 shows I2 results for 100 cycles for both ignition systems and it is clear that with this method, pre-chamber results show lower knock level, something all other knock detection methods previously discussed here failed to capture. Fig. 8.11 shows all knocking cycles for both ignition systems predicted as knock by KI2 knock index.

A motor-sport engine often used with different power rating for the same race, depending on the race condition. For example, the engine is tuned for maximum power during qualifying sessions. With fuel flow restriction, one possible direction to get more power from the engine is to advance ignition timing and allowing more knocking cycles. With KI2 method, same can be implemented by increasing the constant, k in the Eq:8.5.
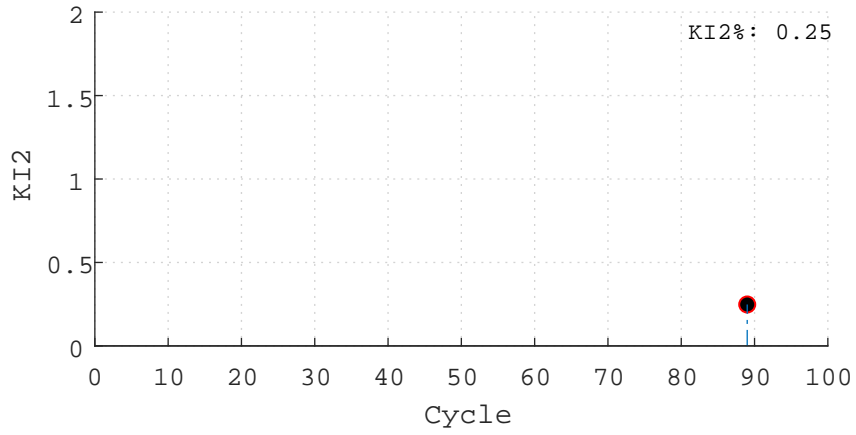
(a) Base, 6000 rpm
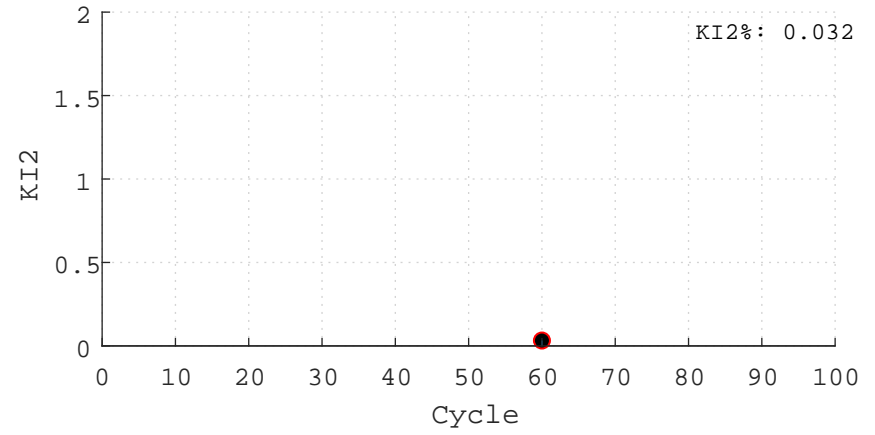
(b) PC, 6000 rpm
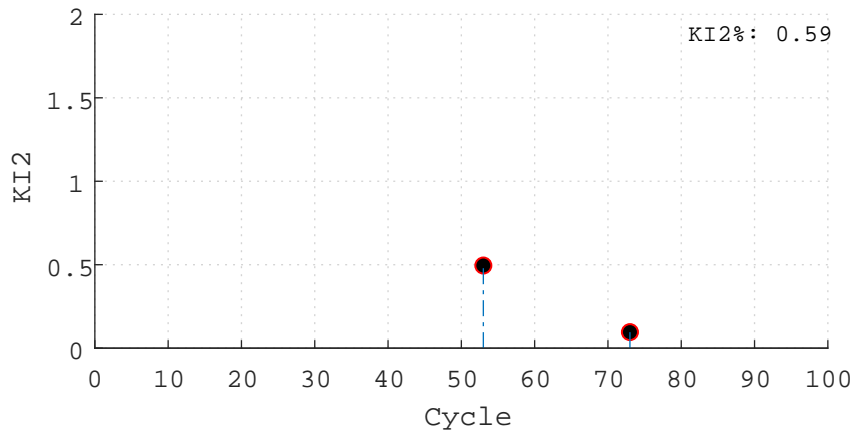
(c) Base, 7500 rpm
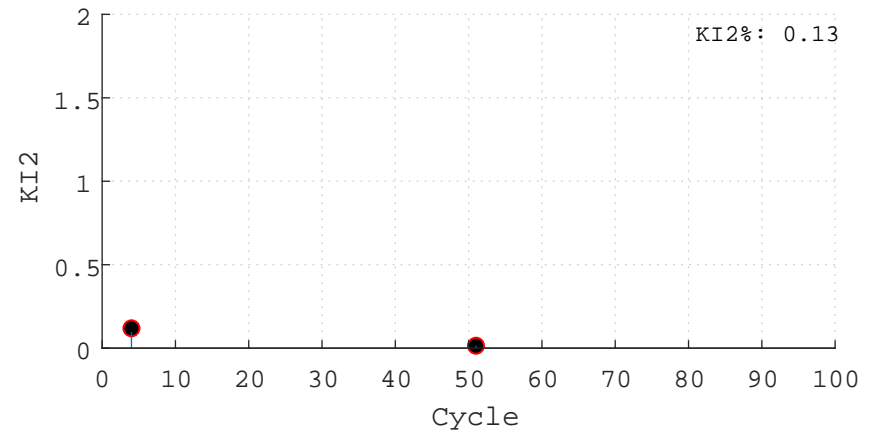
(d) PC, 7500 rpm

Figure 8.10: Knock Index (KI2) results

Fig. 8.11 shows all individual cycles detected by this method as knocking cycle.

(a) Base, 6000 rpm, Cycle: 89

(b) Base, 7500 rpm, Cycle: 53

(c) Base, 7500 rpm, Cycle: 73

(d) PC2, 6000 rpm, Cycle: 60

(e) PC2, 7500 rpm, Cycle: 4

(f) PC, 7500 rpm, Cycle: 51
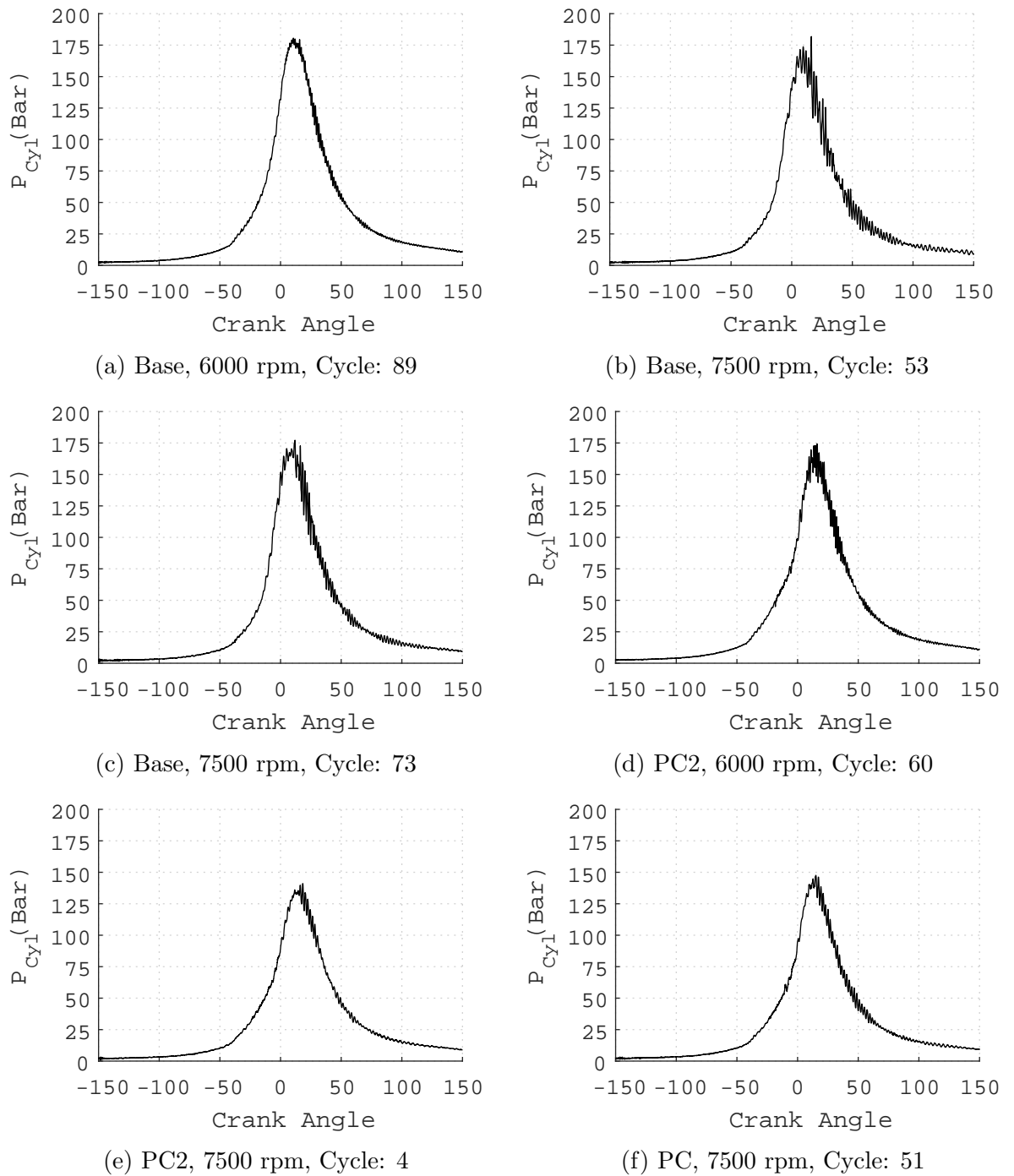
Figure 8.11: Knocking cycles

8.3 Summary

This chapter discussed the difficultly of using a transducer based knock detection and conventional cylinder pressure based knock indicators for an engine with pre-chamber ignition system. KI2 method is identified as a knock detection method for

high-speed, high BMEP, pre-chamber ignited gasoline engine. This method was not implemented for live knock detection on SCRE due to ECU hardware limitations. For cylinder pressure based knock detection, it requires ECU hardware modification to include additional channels for pressure sensors and also increases memory demand substantially for data logging and processing. Although combustion analyser can process the pressure signal and give feedback to ECU, filtering of pressure signal, which is necessary for detecting knock pressure, results in signal latency and hence was not used. Implementation of KI2 also require simultaneous heat release calculation, results in more calculation per cycle. With necessary hardware updates, KI2 can be used for live knock detection.

Chapter 9

Conclusions and Future Work

Contents

9.1 Conclusions

1. A RANS based multi-dimensional engine model with detailed chemistry based combustion model can aid the design of combustion devices like pre-chamber.

2. While designing the pre-chamber, scavenging inside the pre-chamber is a key factor to be considered and combustible air/fuel mixture is much beneficial inside the pre-chamber. This research used a passive pre-chamber system and air guided spray formation was utilised to get rich mixture inside the pre-chamber. But, for overall relative AFR of 1.2 tested, achieving λ below 1.0 inside the pre-chamber was difficult. This research identified that a small volume pre-chamber helps in maintaining reduced λ inside the pre-chamber.

3. Pre-chamber ignition system is able to reduce the burn duration substantially for a lean-burn gasoline engine over the conventional spark ignition system. Combining both changes in ignition delay and burn duration, around 30% reduction in total burn duration was achieved. This short burn duration is benefiting in reduced cyclic variation and resultant lower ISFC. The gain in performance due to reduction in cyclic variation is limited as the base engine also has lower cyclic variation, due to high tumble flow and resultant turbulent combustion.

4. Multi-dimensional engine model shows pre-chamber is able to produce distributed ignition sites through turbulent flame jets. This multiple ignition sources can reduce end-gas residence time and hence has the potential to reduce end-gas auto-ignition. Also, these turbulent flame jets can be directed

towards the potential knock initiation sites like valve pockets on the piston, burning such sensitive areas first and hence improving knock resistance of the engine. Experimental results proved this finding as combustion anchor angle could be advanced with pre-chamber, even without achieving KLSA operating points. This factor of improving knock resistance was contributing more to performance gain with pre-chamber.

5. Pre-chamber system results in increased heat transfer losses with additional pre-chamber surface area and limits the performance gain. This research shows heat transfer loss from the pre-chamber is only significant for a large volume pre-chamber (>1.0cc).

6. A transducer based knock detection system has difficulty in detecting engine knock with pre-chamber ignition system. Also, cylinder pressure based knock detection methods including MAPO and IMPO are failed to detect knocking cycle due to high frequency oscillations with the pre-chamber jets. A cylinder pressure based knock detection method, KI2 knock indicator, originally proposed by Galloni [86], was identified as a suitable live knock detection method and could be used for high BMEP, high speed pre-chamber ignited gasoline engines.

7. This research could not extend the lean limit of the base engine beyond λ, 1.2, though pre-chamber system worked better compared to spark ignition with increased dilution up to λ, 1.4.

8. Heat dissipation from the pre-chamber component, especially the area which is exposed to both pre-chamber and main combustion chamber is crucial in avoiding pre-ignition.

9.2 Future work

1. With the current fuel flow rate tested (13.32 kg-hr), engine was operating close to MBT conditions. The pe-chamber has to be tested at increased cylinder loading (17.5 kg-hr), where knock limited spark retard is higher.

2. The pre-chamber was tested on a combustion chamber, designed to work best with spark ignition. With the pre-chamber, influence of cylinder aerodynamics on turbulent combustion has to be reviewed and combustion chamber can be re designed to benefit pre-chamber ignited combustion. This work established that reducing exhaust back pressure has a positive effect on engine performance. So, reducing intake valve seat masking, currently used in the engine to aid turbulent combustion, can benefit in reduced back pressure, resulting in

lower residuals and better performance. Transient performance for the turbo-charged engine can also be improved with reduced manifold pressure demand, which is possible with improved volumetric efficiency as a result of reduced valve seat masking.

3. With the current engine, lean limit could not be extended, because the base engine was operating close to MBT ignition timing and higher dilution results in slower flame speed inside the main chamber and requires ignition advance to keep the same combustion anchor angle. But as identified in this work, earlier ignition timing results in pre-chamber combustion before pre-chamber scavenging and enrichment with fresh air-fuel mixture, resulting in high combustion cyclic variation. So it is crucial to keep ignition timing close to TDC, which is for this work identified as after 30° CA BTDC. One option is to bring back KLSA instead of MBT ignition timing by increasing the compression ratio. So lean limit and compression ratio can be simultaneously increased to keep the ignition angle close to TDC, with both these changes can increase thermal efficiency. Variable intake valve timing can be implemented to change the effective compression ratio in order to maintain KLSA ignition timing to the optimum value for a wider speed range.

4. With this work, base spray settings were used. It is possible to study split injection with later injection can be done during later stages of compression stroke. Upward directed air flow during compression stroke and with reverse jets to the pre-chamber, pre-chamber enrichment can be improved. A CFD simulation with split injection shows localised enrichment near the spark plug, but the case could not be tested because the fuel quantity injected per cycle is not sufficient to have split injection, meeting injector minimum holding time (1 ms) and dwell time (2 ms).

5. Pre-ignition events observed with the pre-chamber testing has to be addressed by changing combustion chamber design to increase heat transfer from the pre-chamber tip area.

References

[1] ONS. Road transport and air emissions. Office for National Statistics, UK; 2019. Available from: https://www.ons.gov.uk/economy/environmentalaccounts/articles/roadtransportandairemissions/2019-09-16.

[2] IMechE. A Complementary Approach Using Sustainable and Low Carbon Fuels. Institution of Mechanical Engineers; 2020.

[3] EIA. Annual Energy Outlook 2020: Transportation. US Energy Information Administration; 2020. Available from: www.eia.gov/aeo.

[4] Whiting C. FIA Formula one world championship regulations; 2018. Available from: https://www.fia.com/regulation/category/110.

[5] Heywood JB. Internal combustion engine Fundamentals. vol. 2; 2006.

[6] Abraham J, Williams FA, Bracco FV. A Discussion of Turbulent Flame Structure in Premixed Charges. SAE Technical Paper. 1985;850345.

[7] Stone R. Introduction to Internal Combustion Engines. 4th ed. Palgrave Macmillan; 2012.

[8] Heywood JB. Combustion chamber design for optimum spark ignition engine performance. International Journal of Vehicle Design. 1984;5(3).

[9] Hires S, Tabaczynski R, Novak J. The Prediction of Ignition Delay and Combustion Intervals for a Homogeneous Charge, Spark Ignition Engine. SAE Technical Paper. 1978;780232.

[10] Toulson E, Schock HJ, Attard WP. A review of prechamber initiated jet ignition combustion systems. SAE Technical Paper. 2010;2010-01-22.

[11] Metghalchi M, Keck JC. Burning Velocities of Mixtures of Air with Methanol, Isooctane, and Indolene at High Pressure and Temperature. Combustion and Flame. 1982;48:191–210.

[12] Groff EG, Matekunas FA. The Nature of Turbulent Flame Propagation in a Homogeneous Spark-Ignited Engine. SAE Technical Paper. 1980;800133.

[13] Matekunas FA. Modes and Measures of Cyclic Combustion Variability. SAE Technical Paper. 1983;830337.

[14] Young MB. Cyclic Dispersion in the Homogeneous-Charge Spark-Ignition Engine—A Literature Survey. SAE Technical Paper. 1981;810020.

[15] Hansel JG. Lean Automotive Engine Operation - Hydrocarbon Exhaust Emissions and Combustion Characteristics. SAE Technical Paper. 1971;710164.

[16] Ozdor N, Dulger M, Sher E. Cyclic Variability in Spark Ignition Engines A Literature Survey. SAE Technical Paper. 1994;940987.

[17] Vermorel O, Richard S, Colin O, Angelberger C, Benkenida A, Veynante D. Towards the understanding of cyclic variability in a spark ignited engine using multi-cycle LES. Combustion and Flame. 2009;156:1525–1541.

[18] Adomeit P, Lang O, Pischinger S, Aymanns R, Graf M, Stapf G. Analysis of Cyclic Fluctuations of Charge Motion and Mixture Formation in a DISI Engine in Stratified Operation. SAE Technical Paper. 2007;2007-01-14.

[19] Goryntsev D, Sadiki A, Klein M, Janicka J. Large eddy simulation based analysis of the effects of cycle-to-cycle variations on air-fuel mixing in realistic DISI IC-engines. Proceedings of the Combustion Institute. 2009;32.

[20] Truffin K, Angelberger C, Richard S, Pera C. Using large-eddy simulation and multivariate analysis to understand the sources of combustion cyclic variability in a spark-ignition engine. Combustion and Flame. 2015;162:4371–4390.

[21] Tomazic D, Kleeberg H. The Future of the Internal Combustion Engine. In: SAE 2011 Electronic Systems for Vehicle Propulsion Symposium. SAE 2011 Electronic Systems for Vehicle Propulsion Symposium. SAE International; 2011. .

[22] Griffiths JF, Barnard JA. Flame and combustion. CRC Press; 1995.

[23] Freeland P, Warth M, Mahr B. Minimising autoignition for optimum efficiency in high specific output spark ignited engines. In: 4th International Conference on Knocking in Gasoline Engines. IAV automotive engineering; 2013. .

[24] Towers JM, Hoekstra RL. Engine Knock , A Renewed Concern In Motorsports - A Literature Review. SAE Technical Paper. 1998;983026.

[25] Bai Yl, Wang Jx, Wang Z, Shuai Sj. Knocking Suppression by Stratified Stoichiometric Mixture With Two-Zone Homogeneity in a DISI Engine. Journal of Engineering for Gas Turbines and Power. 2012;135(1):012803.

[26] Liang L, Reitz RD, Iyer CO, Yi J. Modeling Knock in Spark-Ignition Engines Using a G-equation Combustion Model Incorporating Detailed Chemical Kinetics. SAE Technical Paper. 2007;2007-01-01.

[27] Wang Z, Liu H, Reitz RD. Knocking combustion in spark-ignition engines. Progress in Energy and Combustion Science. 2017;61:78–112.

[28] Grandin B, Ångström HE, Stålhammar P, Olofsson E. Knock suppression in a turbocharged SI engine by using cooled EGR. In: International Fall Fuels and Lubricants Meeting and Exposition. SAE International; 1998. .

[29] Su J, Xu M, Li T, Gao Y, Wang J. Combined effects of cooled EGR and a higher geometric compression ratio on thermal efficiency improvement of a downsized boosted spark-ignition direct-injection engine. Energy Conversion and Management. 2014;78.

[30] Goto T, Isobe R, Yamakawa M, Nishida M. The new Mazda gasoline engine Sky- activ-G. ATZ Auto Technology. 2011;.

[31] Takahashi D, Nakata K, Yoshihara Y, Ohta Y, Nishiura H. Combustion Development to Achieve Engine Thermal Efficiency of 40% for Hybrid Vehicles. SAE Technical Paper. 2015;2015-01-12.

[32] Matsura K, Sato Y, Yoshida K, Sono H. Proposal of Knock Mitigation Method Through Enhancement of Local Heat Transfer. In: 5th International Conference on Knocking in Gasoline Engines. IAV automotive engineering; 2017. .

[33] Attard WP, Blaxill H, Anderson EK, Litke P. Knock Limit Extension with a Gasoline Fueled Pre-Chamber Jet Igniter in a Modern Vehicle Powertrain. SAE International Journal of Engines. 2012;2012-01-11.

[34] Guardian. Britain to ban sale of all diesel and petrol cars and vans from 2040; 2017.

[35] Attard WP, Kohn J, Parsons P. Ignition Energy Development for a Spark Initiated Combustion System Capable of High Load, High Efficiency and Near Zero NOx Emissions. SAE Technical Paper. 2010;2010-32-00.

[36] Mamakos A. Feasibility of Introducing Particulate Filters on Gasoline Direct Injection Vehicles, Institute for Energy and Transport. Joint Research Center Scientific and Policy Reports 2011; 2011.

[37] EEA. Air Quality in Europe — 2013 Report. European Environment Agency; 2013. Available from: https://www.eea.europa.eu/publications/air-quality-in-europe-2013.

[38] Amin P, Kakaee AH, Pourya R, Reitz RD. Progress and recent trends in reactivity-controlled compression ignition engines. International Journal of Engine Research. 2016;17(5):481–524.

[39] Attard WP, Parsons P. Flame Kernel Development for a Spark Initiated Pre-Chamber Combustion System Capable of High Load , High Efficiency and Near Zero NOx Emissions. SAE Technical Paper. 2012;2010-32-00.

[40] Tasuku D, Shizuo Y, Akira I, Isao F. Research and Development of the Honda CVCC Engine. SAE Technical Paper. 1974;(740605):20.

[41] C Robinet, P Higelin, B Moreau OP, Andrzejewski J. A New Firing Concept for Internal Combustion Engines: 'I'APIR". SAE Technical Paper. 1999;1999-01-06.

[42] Couet S, Higelin P, Moreau B. APIR: A New Firing Concept for the Internal Combustion Engines - sensitivity to knock and in-cylinder aerodynamics. SAE Technical Paper. 2001;2001-01-19.

[43] Zhao F, Thomas NA, Dennis NA, John ED, James AE, Paul MN. Homogeneous Charge Compression Ignition (HCCI) Engines. SAE International; 2003.

[44] Chinnathambi P, Bunce M, Cruff L. RANS Based Multidimensional Modeling of an Ultra-Lean Burn Pre-Chamber Combustion System with Auxiliary Liquid Gasoline Injection. SAE 2015 World Congress and Exhibition. 2015;2015-01-03.

[45] Toulson E, Thelen BC. A computational study on the effect of the orifice size on the performance of a turbulent jet ignition system. Proceedings of the Institution of Mechanical Engineers, Part D: Journal of Automobile Engineering. 2016;.

[46] Thelen BC, Toulson E. A Computational Study of the Effects of Spark Location on the Performance of a Turbulent Jet Ignition System. SAE Technical Paper. 2016;2016-01-06.

[47] Gussak LA, Turkish MC, Siegla DC. High Chemical Activity of Incomplete Combustion Products and a Method of Prechamber Torch Ignition for Avalanche Activation of Combustion in Internal Combustion Engines. SAE Technical Paper. 1975;750890.

[48] Kettner M, Rothe M, Velji A, Spicher U, Kuhnert D, Latsch R. A new flame jet concept to improve the inflammation of lean burn mixtures in SI engines. SAE Technical Paper. 2005;2005-01-36.

[49] Attard WP, Blaxill H. A Single Fuel Pre-Chamber Jet Ignition Powertrain Achieving High Load, High Efficiency and Near Zero NOx Emissions. SAE International Journal of Engines. 2011;2011-01-20.

[50] Attard WP, Blaxill H. A Lean Burn Gasoline Fueled Pre-Chamber Jet Ignition Combustion System Achieving High Efficiency and Low NOx at Part Load. SAE International Journal of Engines. 2012;2012-01-11.

[51] Attard WP, Blaxill H. A Gasoline Fueled Pre-Chamber Jet Ignition Combustion System at Unthrottled Conditions. SAE International Journal of Engines. 2012;2012-01-03.

[52] Attard WP, Fraser N, Parsons P, Toulson E. A Turbulent Jet Ignition Pre-Chamber Combustion System for Large Fuel Economy Improvements in a Modern Vehicle Powertrain. SAE Technical Paper. 2010;2010-01-14.

[53] Vedula RT, Song R, Stuecken T, Zhu GG, Schock H. Thermal efficiency of a dual-mode turbulent jet ignition engine under lean and near-stoichiometric operation. International Journal of Engine Research. 2017;.

[54] Geiger J, Pischinger S, Böwing R. Ignition Systems for Highly Diluted Mixtures in SI-Engines. SAE Technical Paper. 1999;1999-01-07.

[55] Hamori F. Exploring the Limits of Hydrogen Assisted Jet Ignition. Ph.D. thesis. The University of Melbourne; 2006.

[56] Anderson EK, Attard WP, Brown A, Litke P, Grinstead K, Hoke J. Experimental Study of a Pre-Chamber Jet Igniter in a Turbocharged Rotax 914 Aircraft Engine. SAE Technical Paper. 2013;2013-01-16.

[57] Richards KJ, Senecal PK, Pomraning E. CONVERGE 2.4. Convergent Science, Inc., Madison, WI(2018); 2018.

[58] Richards KJ, Senecal PK, Pomraning E. CONVERGE 2.4 Manual. Convergent Science, Madison, WI (2018); 2018.

[59] Richard S, Colin O, Vermorel O, Benkenida a, Angelberger C, Veynante D. Towards large eddy simulation of combustion in spark ignition engines. Proceedings of the Combustion Institute. 2007;31 II:3059–3066.

[60] Granet V, Vermorel O, Lacour C, Enaux B, Dugué V, Poinsot T. Large-Eddy Simulation and experimental study of cycle-to-cycle variations of stable and unstable operating points in a spark ignition engine. Combustion and Flame. 2012;159:1562–1575.

[61] Pope SB. Turbulent Flows; 2000.

[62] Pomraning E, Richards K, Senecal PK. Modeling Turbulent Combustion Using a RANS Model, Detailed Chemistry, and Adaptive Mesh Refinement. SAE Technical Paper Series. 2014;2014-01-11.

[63] Launder BE, Sharma BI. Application of the energy-dissipation model of turbulence to the calculation of flow near a spinning disc. Letters in Heat and Mass Transfer. 1974;.

[64] Launder BE, Spalding DB. Mathemtical Models of Turbulence. Journal of Applied Mathematics and Mechanics. 1973;.

[65] Amsden AA, O'Rourke PJ, Butler TD. KIVA-II: A Computer Program for Chemically Reactive Flows with Sprays. Los Alamos National Lab,. 1989;.

[66] Senecal PK, Pomraning E, Richards KJ. Multi-dimensional modeling of direct-injection diesel spray liquid length and flame lift-off length using CFD and parallel detailed chemistry. SAE Technical Paper. 2003;2003-01-10.

[67] Robert J. Chemkin-II: A Fortran chemical kinetics package for the analysis of gas-phase chemical kinetics. Sandia National Laboratories Report. 1991;.

[68] Liu YD, Jia M, Xie MZ, Pang B. Development of a new skeletal chemical kinetic model of toluene reference fuel with application to gasoline surrogate fuels for computational fluid dynamics engine simulation. Energy and Fuels. 2013;.

[69] Marinov NM. A detailed chemical kinetic model for high temperature ethanol oxidation. International Journal of Chemical Kinetics. 2002;.

[70] Turns SR. An introduction to combustion: concepts and applications; 2000.

[71] Issa RI. Solution of the implicitly discretised fluid flow equations by operator-splitting. Journal of Computational Physics. 1986;.

[72] Richards K, Pomraning E, Probst D. The Observation of Cyclic Variation in Engine Simulations When Using RANS Turbulence Modeling. Proceedings of the ASME 2014 Internal Combustion Engine Division Fall Technical Conference. 2014;p. 1–19.

[73] Jupudi RS, Finney CEA, Primus R, Wijeyakulasuriya S, Klingbeil AE, Tamma B, et al. Application of High Performance Computing for Simulating Cycle-to-Cycle Variation in Dual-Fuel Combustion Engines. SAE Technical Papers. 2016;2016-01-07.

[74] Scarcelli R, Richards K, Pomraning E, Senecal PK, Wallner T, Sevik J. Cycle-to-Cycle Variations in Multi-Cycle Engine RANS Simulations. SAE Technical Papers. 2016;2016-01-05.

[75] Pitz WJ, Cernansky NP, Dryer FL, Egolfopoulos FN, Farrell JT, Friend DG, et al. Development of an Experimental Database and Chemical Kinetic Models for Surrogate Gasoline Fuels. In: SAE Technical Paper. vol. 2007-01-01. SAE International; 2007. Available from: https://doi.org/10.4271/2007-01-0175.

[76] Chun KM, Heywood JB. Characterization of knock in a spark-ignition engine. In: SAE Technical Papers; 1989. .

[77] Biehl M, Meister M. Model Based Knock Detection. In: 5th International Conference on Knocking in Gasoline Engines. Springer; 2017. .

[78] Scarcelli R, Zhang A, Wallner T, Som S, Huang J, Wijeyakulasuriya S, et al. Development of a Hybrid Lagrangian-Eulerian Model to Describe Spark-Ignition Processes at Engine-Like Turbulent Flow Conditions. Journal of Engineering for Gas Turbines and Power. 2019 sep;141(9).

[79] Neo GH, Collings N. Pressure data analysis of formula one racing engines. SAE Technical Papers. 1997;970061(412).

[80] Randolph A. Cylinder Pressure Based Combustion Analysis in Race Engines. SAE Technical Paper. 1994;942487.

[81] Leppard WR. Individual-cylinder knock occurence and intensity in multicylinder engines. SAE Technical Papers. 1982;820074.

[82] Benson G, Fletcher EA, Murphy TE, Scherrer HC. Knock (Detonation) Control by Engine Combustion Chamber Shape. In: SAE International Congress and Exposition. SAE International; 1983. .

[83] Arrigoni V, Cornetti G, Gaetani B, Ghezzi P. Quantitative systems for measuring knock. 1972;.

[84] Brecq G, Bellettre J, Tazerout M. A new indicator for knock detection in gas SI engines. International Journal of Thermal Sciences. 2003;42(5):523–532.

[85] Hudson C, Gao X, Stone R. Knock measurement for fuel evaluation in spark ignition engines. Fuel. 2001;80(3):395–407.

[86] Galloni E. Dynamic knock detection and quantification in a spark ignition engine by means of a pressure based method. Energy Conversion and Management. 2012;64:256–262.

Appendix A

Chemical Mechanism

```
! Reaction mechanism of TRF
! Development of a new skeletal chemical kinetic model of toluene reference fuels with
    application to gasoline surrogate fuels for CFD engine simulation.
! Energy & Fuels
! Yao-Dong Liu, Ming Jia, Mao-Zhao Xie*, Bin Pang
! Dalian University of Technology
! February, 2013
! Units are cm3, mole, cal; k = a*t**n exp(-e/rt).
! 56 species and 168 reactions.
! Low temperature and decomposition reactions of PRF are based on Tanaka and Tsurushima.
! Sub mechanism of toluene are based on Yasuyuki Sakai, Andrae and Mehl.
! C2-C3 reactions are from Patel.
! C2C2 reactions are from Yoo.
! Other small molecule reactions are from Klippenstein.
ELEMENTS
H O N AR C
END
SPECIES
O2          N2          CO2         H2O         CO          H2          OH
H2O2        HO2         H           O           CH4         CH3O        CH2O
HCO         CH3         C2H3        C2H4        C2H5        C3H4        C3H5
C3H6        C3H7        C7H16       C7H15       C7H15O2     C7H14OOH    O2C7H14OOH
C7KET       C5H11CO     C7H14       C8H18       C8H17       C8H17O2     C8H16OOH
O2C8H16OOH  C8KET       C6H13CO     C8H16       CH2OH       CH3OH
C7H8        C6H5CH2     C6H5CHO     C6H5CO      C6H5        C6H5O       C6H6
C6H5OH      C5H5        C5H4O       C5H4OH      C4H5
C2H2        CH2CO       HCCO
!
!**********************************************************
! Ethanol sub set
! Ref: Marinov, IJCK 31:183-220 (1999)
!**********************************************************
!
C2H5OH      CH3CHOH     C2H4OH      CH3CH2O     HOC2H4O2    CH3HCO      CH2CHCH3
!
END
! UNITS ARE CM3, MOLE, CAL; K = A T**N EXP(-E/RT)---------------------------------
REACTIONS
! N-HEPTANE
C7H16     + O2      = C7H15     + HO2                  1.000E+16   0.00    46000.0
 REV                                               /  1.000E+12   0.00        0.0 /
C7H16     + OH      =>C7H15     + H2O                  5.000E+13   0.00     3000.0          !
     MODIFIED
C7H16     + HO2     =>C7H15     + H2O2                 1.000E+13   0.00    16950.0
C7H15     + O2      = C7H15O2                          3.000E+12   0.00        0.0          !
     MODIFIED
 REV                                               /  2.510E+13   0.00    27400.0 /
C7H15O2             = C7H14OOH                         1.510E+11   0.00    19000.0
 REV                                               /  1.000E+11   0.00    11000.0 /
C7H14OOH  + O2      = O2C7H14OOH                       6.160E+10   0.00        0.0          !
     MODIFIED
 REV                                               /  2.510E+13   0.00    27400.0 /
O2C7H14OOH          =>C7KET     + OH                   8.910E+10   0.00    17000.0
C7H15     + O2      = C7H14     + HO2                  3.160E+11   0.00     6000.0
 REV                                               /  3.160E+11   0.00    19500.0 /
C7KET               =>C5H11CO   + CH2O   + OH          3.980E+15   0.00    43000.0
C5H11CO   + O2      =>C3H7      + C2H3   + CO   + HO2  3.160E+13   0.00    10000.0          !
     CHANGED
C7H14     + O2      =>C3H6      + C2H5   + CH2O + HCO  3.160E+13   0.00    10000.0          !
     COMBINED,CHANGED
C7H15               =>C3H6      + C2H5      + C2H4     6.500E+12   0.00    28810.0          !
```

```
      COMBINED,CHANGED, MODIFIED
! ISO–OCTANE
C8H18     + O2       = C8H17     + HO2                    6.000E+15   0.00    46000.0                   !
     MODIFIED
 REV                                             / 1.000E+12    0.00        0.0 /
C8H18     + OH       =>C8H17     + H2O                    2.000E+13   0.00     3000.0                   !
     MODIFIED
C8H18     + HO2      =>C8H17     + H2O2                   1.000E+13   0.00    16950.0
C8H17     + O2       = C8H17O2                            1.000E+12   0.00       0.0
 REV                                             / 2.510E+13    0.00    27400.0 /
C8H17O2               = C8H16OOH                          1.510E+11   0.00    21800.0
 REV                                             / 1.000E+11    0.00    11000.0 /
C8H16OOH  + O2       = O2C8H16OOH                         1.160E+11   0.00       0.0                    !
     MODIFIED
 REV                                             / 2.510E+13    0.00    27400.0 /
O2C8H16OOH           =>C8KET     + OH                     8.910E+10   0.00    17000.0
C8H17     + O2       = C8H16     + HO2                    3.160E+11   0.00     6000.0
 REV                                             / 3.160E+11    0.00    19500.0 /
C8KET              =>C6H13CO  + CH2O  + OH              3.980E+15   0.00    43000.0
C6H13CO   + O2       =>C3H7      + C3H5  + CO   + HO2 3.160E+13   0.00    10000.0                   !
     CHANGED
C8H16     + O2       =>C3H7      + C3H6  + CH2O + HCO 3.160E+13   0.00    10000.0                   !
     COMBINED
C8H17              =>C3H7      + C3H6  + C2H4        1.117E+17  −1.27   29700.0                   !
     COMBINED, MODIFIED
! TOLUENE
C7H8=C6H5CH2+H                                2.090E+15    0.00     87463.4       ! SAKAI
C7H8=C6H5+CH3                                 2.660E+16    0.00     97830.4       ! SAKAI
C7H8+O2=C6H5CH2+HO2                           1.500E+14    0.00     41400.0       ! MEHL
C7H8+H=C6H6+CH3                               1.200E+13    0.00      5100.0       ! MEHL
C7H8+OH=C6H5CH2+H2O                           3.000E+12    0.00      1700.0       ! MEHL
C6H5CH2+O=C6H5CHO+H                           2.110E+14    0.00        0.0        ! SAKAI
C6H5CH2+O=C6H5+CH2O                           1.190E+14    0.00        0.0        ! SAKAI
C6H5CH2+HO2=>C6H5CHO+H+OH                     5.000E+14    0.00        0.0        ! THIS WORK
C6H5CHO+OH=H2O+C6H5CO                         3.440E+09    1.18      −447.0       ! SAKAI
C6H5CHO+H=H2+C6H5CO                           2.280E+10    1.05      3279.0       ! SAKAI
C6H5CO=C6H5+CO                               3.000E+12    0.00     34860.0       ! SAKAI
C6H6+H=C6H5+H2                                2.000E+13    0.00     18600.0       ! SAKAI
C6H6+OH=C6H5+H2O                              1.630E+08    1.42      1451.0       ! SAKAI
C6H6+O=C6H5+OH                                2.000E+13    0.00     14700.0       ! SAKAI
C6H5+H=C6H6                                   2.000E+14    0.00        0.0        ! ANDRAE
C6H5+O2=C6H5O+O                               2.600E+13    0.00      6100.0       ! ANDRAE
C6H5O=C5H5+CO                                 7.400E+11    0.00     43900.0       ! SAKAI
C6H5O+H=C6H5OH                                2.500E+14    0.00        0.0        ! SAKAI
C6H5OH+O2=C6H5O+HO2                           1.000E+13    0.00     38000.0       ! SAKAI
C6H5OH+H=C6H5O+H2                             1.200E+14    0.00     12400.0       ! SAKAI
C6H5OH+O=C6H5O+OH                             1.300E+13    0.00      2900.0       ! SAKAI
C6H5OH+OH=C6H5O+H2O                           3.000E+06    2.00     −1310.0       ! SAKAI
C6H5OH+HO2=C6H5O+H2O2                         1.000E+12    0.00      1000.0       ! SAKAI
C5H5+O=C4H5+CO                                3.200E+13   −0.17       440.0       ! ANDRAE
C5H5+OH=C5H4OH+H                              3.500E+57  −12.18     48350.0       ! ANDRAE
C5H4OH=C5H4O+H                                2.100E+13    0.00     54000.0       ! ANDRAE
C5H4O=>C2H2+C2H2+CO                           5.700E+32   −6.76     68500.0       ! ANDRAE
   DUP
C5H4O=>C2H2+C2H2+CO                           6.200E+41   −7.87     98700.0       ! ANDRAE
   DUP
C4H5=C2H2+C2H3                                1.000E+14    0.00     43890.0       ! SAKAI
! C2–C3 REACTIONS
C3H7               = C2H4      + CH3                      9.600E+13   0.00    30950.0
C3H7               = C3H6      + H                        1.250E+14   0.00    36900.0
C3H6               = C2H3      + CH3                      3.150E+15   0.00    85500.0
C3H6      + CH3    = C3H5      + CH4                      9.000E+12   0.00     8480.0
C3H5      + O2     = C3H4      + HO2                      6.000E+11   0.00    10000.0
C3H4      + OH     = C2H3      + CH2O                     1.000E+12   0.00       0.0
C3H4      + OH     = C2H4      + HCO                      1.000E+12   0.00       0.0
C2H5      + O2     = C2H4      + HO2                      2.000E+10   0.0    −2200.0
C2H4      + OH     = CH2O      + CH3                      6.000E+13   0.00      960.0
C2H4      + OH     = C2H3      + H2O                      8.020E+13   0.00     5955.0
C2H3      + O2     = CH2O      + HCO                      4.000E+12   0.00     −250.0
C2H3      + HCO    = C2H4      + CO                       6.034E+13   0.00       0.0
! C2H2 REACTIONS
C3H5       =   C2H2+CH3      2.397E+48  −9.90   8.208E+04
 REV               /  2.610E+46  −9.82   3.695E+04   /
C2H4(+M)   =   C2H2+H2(+M)   1.800E+13   0.00   7.600E+04
 LOW              /  1.500E+15   0.00   5.544E+04   /
C2H3+O2    = C2H2+HO2        2.120E−06   6.00   9.484E+03
 REV              /  1.114E−07   6.33   1.757E+04   /
C2H3+H     =   C2H2+H2       2.000E+13   0.00   2.500E+03
 REV              /  1.331E+13   0.00   6.808E+04   /
C2H2+H(+M) = C2H3(+M)        3.110E+11   0.58   2.589E+03
 LOW              /  2.254E+40  −7.269   6577.      /
 TROE/ 1.0  1.E−15  675.  1.E+15/
 H2/2/ H2O/5/ CO/2/ CO2/3/
```

```
C2H2+O2     =   HCCO+OH         2.000E+08   1.50   3.010E+04
 REV                        /   2.232E+05   1.50   2.540E+04   /
C2H2+O      =   HCCO+H          1.430E+07   2.00   1.900E+03
 REV                        /   2.021E+05   2.00   1.331E+04   /
C2H2+OH     =   CH2CO+H         2.190E-04   4.50  -1.000E+03
 REV                        /   2.161E-03   4.50   1.966E+04   /
CH2CO+H     =   CH3+CO          1.100E+13   0.00   3.400E+04
 REV                        /   2.400E+12   0.00   4.020E+04   /
CH2CO+O     =   HCCO+OH         1.000E+13   0.00   8.000E+03
 REV                        /   1.432E+10   0.00  -1.255E+03   /
CH2CO+OH    =   HCCO+H2O        1.000E+13   0.00   2.000E+03
 REV                        /   1.412E+11   0.00   9.995E+03   /
CH2CO+H     =   HCCO+H2         2.000E+14   0.00   8.000E+03
 REV                        /   6.522E+11   0.00   8.400E+02   /
HCCO+OH     =   HCO+HCO         1.000E+13   0.00   0.000E+00
 REV                        /   2.411E+14   0.00   4.036E+04   /
HCCO+O      =   H+CO+CO         8.000E+13   0.00   0.000E+00
 REV                        /   0.000E+00   0.00   0.000E+00   /
HCCO+O2     =   CO2+HCO         2.400E+11   0.00  -8.540E+02
 REV                        /   1.474E+14   0.00   1.336E+05   /
! ************ H2-O2 CHAIN REACTIONS *********************
! HESSLER, J. PHYS. CHEM. A, 102:4517 (1998)
! 1.26 BAULCH 94
H+O2=O+OH                   3.547E+15  -0.406   1.6599E+4
! SUTHERLAND ET AL., 21ST SYMPOSIUM, P. 929 (1986)
! 3.16 BAULCH 92
O+H2=H+OH                   0.508E+05   2.67   0.629E+04
! MICHAEL AND SUTHERLAND, J. PHYS. CHEM. 92:3853 (1988)
!USE 2 - THIS RATE IS SIMILAR TO TSANG 86.
H2+OH=H2O+H                 0.216E+09   1.51   0.343E+04
! SUTHERLAND ET AL., 23RD SYMPOSIUM, P. 51 (1990)
! USE 2.5 - THIS RATE IS FASTER THAN TSANG 86
O+H2O=OH+OH                 2.97E+06    2.02   1.34E+4
! *************** H2-O2 DISSOCIATION REACTIONS ******************
! TSANG AND HAMPSON, J. PHYS. CHEM. REF. DATA, 15:1087 (1986)
! 3 TSANG 86
H2+M=H+H+M                  4.577E+19  -1.40   1.0438E+05
   H2/2.5/ H2O/12/
   CO/1.9/ CO2/3.8/
! TSANG AND HAMPSON, J. PHYS. CHEM. REF. DATA, 15:1087 (1986)
! USE 2. TSANG 86 SUGGEST 1.3 BUT THERE ARE SOME DISCREPANCIES IN DATA IN NIST.
O+O+M=O2+M                  6.165E+15  -0.50   0.000E+00
   H2/2.5/ H2O/12/
   CO/1.9/ CO2/3.8/
! TSANG AND HAMPSON, J. PHYS. CHEM. REF. DATA, 15:1087 (1986)
! 5 TSANG 86
O+H+M=OH+M                  4.714E+18  -1.00   0.000E+00
   H2/2.5/ H2O/12/
   CO/1.9/ CO2/3.8/
! TSANG AND HAMPSON, J. PHYS. CHEM. REF. DATA, 15:1087 (1986)
! 2 BAULCH 92 SOME ADJUSTMENT FROM BAULCH HAS TAKEN PLACE.
!H+OH+M=H2O+M               2.212E+22  -2.00   0.000E+00
H+OH+M=H2O+M                3.800E+22  -2.00   0.000E+00
   H2/2.5/ H2O/12/
   CO/1.9/ CO2/3.8/
!************** FORMATION AND CONSUMPTION OF HO2******************
! COBOS ET AL., J. PHYS. CHEM. 89:342 (1985) FOR KINF
! MICHAEL, ET AL., J. PHYS. CHEM. A, 106:5297 (2002) FOR K0
!*********************************************************************
! MAIN BATH GAS IS N2 (COMMENT THIS REACTION OTHERWISE)
!
! 3.16 BAULCH 94
 H+O2(+M)=HO2(+M)        1.475E+12   0.60   0.00E+00
     LOW/6.366E+20   -1.72   5.248E+02/
     TROE/0.8   1E-30   1E+30/
     H2/2.0/ H2O/11./ O2/0.78/ CO/1.9/ CO2/3.8/
!*********************************************************************
! MAIN BATH GAS IS AR OR HE (COMMENT THIS REACTION OTHERWISE)
!
! 3.16 BAULCH 94
!H+O2(+M)=HO2(+M)        1.475E+12   0.60   0.00E+00
!     LOW/9.042E+19   -1.50   4.922E+02/
!     TROE/0.5 1E-30   1E+30/
!     H2/3.0/ H2O/16/ O2/1.1/ CO/2.7/ CO2/5.4/
! TSANG AND HAMPSON, J. PHYS. CHEM. REF. DATA, 15:1087 (1986) [MODIFIED]
! 2 TSANG AND HAMPSON 86
HO2+H=H2+O2                 1.66E+13    0.00   0.823E+03
! TSANG AND HAMPSON, J. PHYS. CHEM. REF. DATA, 15:1087 (1986) [MODIFIED]
! 2 TSANG AND HAMPSON 86
HO2+H=OH+OH                 7.079E+13   0.00   2.95E+02
! BAULCH ET AL., J. PHYS. CHEM. REF DATA, 21:411 (1992)
! 3.16 BAULCH 92
HO2+O=O2+OH                 0.325E+14   0.00   0.00E+00
```

```
! KEYSER, J. PHYS. CHEM. 92:1193 (1988)
! 3.16 BAULCH 92
HO2+OH=H2O+O2                2.890E+13   0.00  -4.970E+02
! **************FORMATION AND CONSUMPTION OF H2O2******************
! HIPPLER ET AL., J. CHEM. PHYS. 93:1755 (1990)
! USE 5. ONLY 1 SET OF HIGH TEMPERATURE MEASUREMENTS.
! EXTRAPOLATION TO HIGHER TEMPS.
HO2+HO2=H2O2+O2              4.200E+14   0.00   1.1982E+04
   DUPLICATE
HO2+HO2=H2O2+O2              1.300E+11   0.00  -1.6293E+3
   DUPLICATE
! BROUWER ET AL., J. CHEM. PHYS. 86:6171 (1987) FOR KINF
! WARNATZ, J. IN COMBUSTION CHEMISTRY (1984) FOR K0
! 3.16 BAULCH 92
H2O2(+M)=OH+OH(+M)          2.951E+14    0.00   4.843E+04
! 2 WARNATZ 84
   LOW/1.202E+17   0.00   4.55E+04/
   TROE/0.5 1E-30 1E+30/
   H2/2.5/  H2O/12/
   CO/1.9/  CO2/3.8/
! TSANG AND HAMPSON, J. PHYS. CHEM. REF. DATA, 15:1087 (1986)
! 5 TSANG AND HAMPSON, JPC REF. DATA, 15:1087 (1986)
H2O2+H=H2O+OH               0.241E+14   0.00   0.397E+04
! TSANG AND HAMPSON, J. PHYS. CHEM. REF. DATA, 15:1087 (1986)
! 5 TSANG AND HAMPSON, JPC REF. DATA, 15:1087 (1986)
H2O2+H=HO2+H2               0.482E+14   0.00   0.795E+04
! TSANG AND HAMPSON, J. PHYS. CHEM. REF. DATA, 15:1087 (1986)
! 3 TSANG AND HAMPSON, JPC REF. DATA, 15:1087 (1986)
H2O2+O=OH+HO2               9.550E+06   2.00   3.970E+03
! HIPPLER AND TROE, J. CHEM. PHYS. LETT. 192:333 (1992)
! 1.26 ATKIN 2004
H2O2+OH=HO2+H2O             1.000E+12   0.00   0.000
       DUPLICATE
! USE 5 - BIG DEVIATION FROM BAULCH 92 AT HIGHER TEMPS.
H2O2+OH=HO2+H2O             5.800E+14   0.00   9.557E+03
       DUPLICATE
!************** CO/HCO REACTIONS ****************
! TROE, 15TH SYMPOSIUM
! 2.5 TSANG AND HAMPSON, JPC REF. DATA, 15:1087 (1986)
CO+O(+M)=CO2(+M)            1.80E+10   0.00   2384.
! FIT OF WESTMORELAND, AICHE J., 1986, REL. TO N2 - TIM ADJUSTED FROM MTA'S
! RATE CONSTANT, WHICH WAS REL TO AR.
   LOW/1.55E+24  -2.79   4191./
   H2/2.5/ H2O/12/ CO/1.9/ CO2/3.8/
! TSANG AND HAMPSON, JPC REF. DATA, 15:1087 (1986)
! 2 TSANG AND HAMPSON, JPC REF. DATA, 15:1087 (1986)
CO+O2=CO2+O                0.253E+13   0.00   0.477E+05
! THIS RATE CONSTANT IS MODIFIED PER AN UPDATED VALUE FOR HO2+HO2=H2O2+OH
! USE 5. THIS IS STILL A FACTOR OF 5 HIGHER THAN RECENT CALCS BY YOU ET AL.
CO+HO2=CO2+OH              3.01E+13    0.00    2.30E+04
! THIS STUDY (2004) BY MATCHING LITERATURE EXPERIMENT RESULTS
! 3.16 BAULCH 92
CO+OH=CO2+H                     2.229E+05   1.89   -1158.7
! THIS STUDY (2004) BY MATCHING LITERATURE EXPERIMENT RESULTS
! 3.16 BAULCH 94
HCO+M=H+CO+M              4.7485E+11   0.659   1.4874E+04
H2/2.5/ H2O/6/ CO/1.9/ CO2/3.8/
! TIMONEN ET AL., JPC, 92:651 (1988)
! 5 TSANG AND HAMPSON, JPC REF. DATA, 15:1087 (1986)
HCO+O2=CO+HO2             0.758E+13   0.00   0.410E+03
! TIMONEN ET AL., JPC, 91:692 (1987)
! 2 BAULCH 92
HCO+H=CO+H2               0.723E+14   0.00   0.000E+00
! TSANG AND HAMPSON, JPC REF. DATA, 15:1087 (1986)
!   2 BAULCH 92
HCO+O=CO+OH               0.302E+14   0.00   0.000E+00
! TSANG AND HAMPSON, JPC REF. DATA, 15:1087 (1986)
! 3 TSANG AND HAMPSON, JPC REF. DATA, 15:1087 (1986)
HCO+OH=CO+H2O             0.302E+14   0.00   0.000E+00
! ALL REACTIONS FROM TSANG AND HAMPSON, JPC REF. DATA, 15:1087 (1986)
! 3 TSANG AND HAMPSON, JPC REF. DATA, 15:1087 (1986)
HCO + O = CO2 + H                3.000E+13   0.00   0.000E+00
! 5 TSANG AND HAMPSON, JPC REF. DATA, 15:1087 (1986)
HCO + HO2 = CO2 + OH + H        3.000E+13   0.00   0.000E+00
! 2 TSANG AND HAMPSON, JPC REF. DATA, 15:1087 (1986)
HCO + CH3 = CO + CH4           1.200E+14   0.00   0.000E+00
! USE 10 BECAUSE THIS VALUE IS VERY DIFFERENT FROM YEE
HCO + HCO = H2 + CO + CO        3.000E+12   0.00   0.000E+00
! GLARBORG ET AL., COMBUST FLAME, 132:629 (2003)
! 2 BAULCH 92
HCO + HCO = CH2O + CO           3.0E+13   0.00   0.00
!********************** CH2O REACTIONS   ********************
! FRIEDRICHS ET AL., IJCK, 36:157 (2004)
```

```
! 3.16 BAULCH 94
 CH2O + M = HCO + H + M                 3.3E+39   −6.3   9.99E+04
 H2/2.5/ H2O/12.0/ CO/1.9/ CO2/3.8/
 CH2O + M = CO + H2 + M                 3.1E+45   −8.0   9.751E+04
 H2/2.5/ H2O/12.0/ CO/1.9/ CO2/3.8/
! IRDAM ET AL., IJCK, 25:285 (1993)
! 2 BAULCH 94
CH2O + H = HCO + H2                     5.74E+07   1.9   2.7486E+03
! TSANG AND HAMPSON, JPC REF. DATA, 15:1087 (1986)
! 2 BAULCH 92
CH2O + O = HCO + OH                     1.810E+13   0.00   3.080E+03
!TSANG AND HAMPSON, JPC REF. DATA, 15:1087 (1986)
! 10 BAULCH 92
CH2O + OH = HCO + H2O                   3.430E+09   1.18   −4.470E+02
!HIDAKA ET AL. COMBUST FLAME 92:365 (1993)
! 3.16 BAULCH 92.
CH2O + O2 = HCO + HO2                   1.23E+6 3.00 52000.
!EITENEER ET AL, JPC A. 102:5196 (1998)
! 3.16 BAULCH 92.
  CH2O + HO2 = HCO + H2O2               4.11E+4   2.5   10210.
!FISCHER ET AL. IJCK, 32:713 (2000)
! USE 2 − DIFFERENT FROM BAULCH 94 BY AT LEAST FACTOR OF 2.
CH2O+CH3 = HCO+CH4   3.636E−06   5.42   9.980E+02
!************************* CH4 REACTIONS*******************************
! SLAGLE ET AL., JPC, 91:4375 (1987)
! 1.58 BAULCH 92.
CH3 + O = CH2O + H                      8.430E+13   0.00   0.000E+00
! TSANG AND HAMPSON, JPC REF. DATA, 15:1087 (1986)
! 3.16 BAULCH 92.
CH3 + O2 = CH3O + O                     1.990E+18   −1.57   2.923E+04
!SCIRE ET AL. IJCK, 33:75 (2001)
! USE 10. VERY DIFFERENT FROM BAULCH
CH3 + O2 = CH2O + OH                    3.74E+11 0.0 14640.
! JIM SCIRE (PH.D. THESIS, 2002)ONLY FOR 1000 K
! CH3 + HO2 = CH3O + OH                 1.48E+13   0.00   0.00
!ZHU AND LIN (2001, J.PHYS.CHEM.A 105)
!CH3 + HO2 = CH3O + OH                  6.14244E+10   0.76   −2325   !1000−3000K
!CH3 + HO2 = CH3O + OH                  1.78853E+14   −0.24   −361.67 !300−1000K
! THIS STUDY (2004) BY MODIFING ZHU & LIN'S TO MATCH JIM'S VALUE AT 1000K
! 3 TSANG AND HAMPSON, JPC REF. DATA, 15:1087 (1986)
 CH3 + HO2 = CH3O + OH                  2.41E+10   0.76   −2325
! WALTER ET AL. 23RD SYMP. (INT.) COMBUST. P107 (1990)
! USE 2 BASED ON BAULCH 1994.
!GRI MECH 1.2
! 3.2 BAULCH 92.
 CH3+H(+M) = CH4(+M)                    1.270E+16   −0.630   383.00
      LOW  /   2.477E+33   −4.760   2440.00/
      TROE/  0.7830   74.00   2941.00   6964.00 /
    H2/2.0/ H2O/6.0/ CH4/2.0/ CO/1.5/ CO2/2.0/
! SCHATZ ET AL., JPC, 88:221 (1984)
! 1.58 BAULCH 92. CLOSE TO BAULCH VALUE.
CH4 + H = CH3 + H2                      5.470E+07   1.97   1.121E+04
! KLEMM ET AL. 18TH SYMP. (INT) COMBUST. P785 (1981)
! 2 BAULCH 92.
CH4 + O = CH3 + OH                      3.150E+12   0.50   10290.0
! FELDER AND MADRONICH, CST, 50:135 (1986)
! 1.41 BAULCH 92.
CH4 + OH = CH3 + H2O                    5.720E+06   1.96   2.639E+03
! SCIRE ET AL. IJCK, 33:75 (2001)
! 5 TSANG AND HAMPSON, JPC REF. DATA, 15:1087 (1986)
CH3 + HO2 = CH4 + O2                    3.16E+12   0.00   0.00
! TSANG AND HAMPSON, JPC REF. DATA, 15:1087 (1986)
! 5 TSANG AND HAMPSON, JPC REF. DATA, 15:1087 (1986)
CH4 + HO2 = CH3 + H2O2                  1.810E+11   0.00   1.858E+04
!************************* CH3OH/CH2OH REACTIONS *********************
! CRIBB ET AL. COMBUST FLAME, 88:186 (1992)
! USE 5. SOME DISCREPANCY IN THE LITERATURE.
 CH2OH + M = CH2O + H + M    1.0E+14 0.0 25.1E+3
! TSANG, JPC REF. DATA, 16:471 (1987)
! 2 TSANG, JPC REF. DATA, 16:471 (1987)
CH2OH + H = CH2O + H2                   6.000E+12   0.00   0.000E+00
! TSANG AND HAMPSON, JPC REF. DATA, 15:1087 (1986)
! 2 TSANG, JPC REF. DATA, 16:471 (1987)
CH2OH + H = CH3 + OH                    9.635E+13   0.00   0.000E+00
! TSANG, JPC REF. DATA, 16:471 (1987)
! 2 TSANG, JPC REF. DATA, 16:471 (1987)
CH2OH + O = CH2O + OH                   4.200E+13   0.00   0.000E+00
! TSANG, JPC REF. DATA, 16:471 (1987)
! 2 TSANG, JPC REF. DATA, 16:471 (1987)
CH2OH + OH = CH2O + H2O                 2.400E+13   0.00   0.000E+00
! GROTHEER ET AL., JPC, 92:4028 (1988)
! USED IN NORTON AND DRYER, IJCK, 22:219 (1990)
! HOWEVER, THEY ONLY USED THE HIGH TEMPERATURE PORTION OF THE FIT. THE HIGH
```

```
! TEMPERATURE PORTION ALONE IS 75% OF THE TOTAL AT 700K, 92.8% AT 1000 K
! USE 5. NON ARRHENIUS BEHAVIOUR.
 CH2OH + O2 = CH2O + HO2              2.410E+14   0.00   5.017E+03
     DUP
 CH2OH + O2 = CH2O + HO2              1.510E+15  −1.00   0.000E+00
    DUP
! TSANG, JPC REF. DATA, 16:471 (1987)
! 2 TSANG, JPC REF. DATA, 16:471 (1987)
CH2OH + HO2 = CH2O + H2O2            1.200E+13   0.00   0.000E+00
! THIS STUDY (2004) BY KEEPING THE BRANCHING RATIO IF USING FRIEDRICHS ET AL. (2004) BELOW
! USE 5 − RATE QUITE DIFFERENT FROM TSANG.
CH2OH + HCO = CH3OH + CO            1.000E+13   0.00   0.000E+0
! FRIEDRICHS ET AL. (IJCK, 2004, 36, 157)
! USE 5 − RATE QUITE DIFFERENT FROM TSANG.
CH2OH + HCO = CH2O + CH2O           1.500E+13   0.00   0.000E+00
!******* ETHYLENE GLYCOL FORMATION ****************
! TSANG, JPC REF. DATA, 16:471 (1987)
! 2 TSANG, JPC REF. DATA, 16:471 (1987)
 2CH2OH = CH3OH + CH2O               3.000E+12   0.00   0.000E+00
! TSANG, JPC REF. DATA, 16:471 (1987)
! 2 TSANG, JPC REF. DATA, 16:471 (1987)
 CH2OH + CH3O = CH3OH + CH2O         2.400E+13   0.00   0.000E+00
!********* CH3O REACTIONS *************
! PAGE ET AL., JPC, 93:4404 (1989)
! USE 2. REASONABLE AGREEMENT WITH BAULCH ET AL 92.
CH3O + M = CH2O + H + M              8.300E+17  −1.20   1.550E+04 !MC LIN
! WANTUCK ET AL., JPC, 91:4653 (1987)
! USE 5 DOBE ET AL. SHOW TEMPERATURE DEPENDANCE OF THIS RATE.
CH3O + H = CH3 + OH                  3.200E+13   0.00   0.000E+00
! TSANG AND HAMPSON, JPC REF. DATA, 15:1087 (1986)
! 5 TSANG AND HAMPSON, JPC REF. DATA, 15:1087 (1986)
CH3O + O = CH2O + OH                 6.000E+12   0.00   0.000E+00
! TSANG AND HAMPSON, JPC REF. DATA, 15:1087 (1986)
! 5 TSANG AND HAMPSON, JPC REF. DATA, 15:1087 (1986)
CH3O + OH = CH2O + H2O               1.800E+13   0.00   0.000E+00
! WANTUCK ET AL., JPC, 91:4653 (1987)
! 10 TSANG AND HAMPSON, JPC REF. DATA, 15:1087 (1986)
CH3O + O2 = CH2O + HO2               9.033E+13   0.00   1.198E+04
   DUP
CH3O + O2 = CH2O + HO2               2.200E+10   0.00   1.748E+03
   DUP
! TSANG AND HAMPSON, JPC REF. DATA, 15:1087 (1986)
! 10 TSANG AND HAMPSON, JPC REF. DATA, 15:1087 (1986)
CH3O + HO2 = CH2O + H2O2            3.000E+11   0.00   0.000E+00
! TSANG AND HAMPSON, JPC REF. DATA, 15:1087 (1986)
! 5 TSANG AND HAMPSON, JPC REF. DATA, 15:1087 (1986)
CH3O + CO = CH3 + CO2               1.600E+13   0.00   1.180E+04
! TSANG AND HAMPSON, JPC REF. DATA, 15:1087 (1986)
! 3 TSANG AND HAMPSON, JPC REF. DATA, 15:1087 (1986)
CH3O + HCO = CH3OH + CO             9.000E+13   0.00   0.000E+00
! TSANG AND HAMPSON, JPC REF. DATA, 15:1087 (1986)
! 5 TSANG AND HAMPSON, JPC REF. DATA, 15:1087 (1986)
2CH3O = CH3OH + CH2O                6.000E+13   0.00   0.000E+00
!********* CH3OH REACTIONS ***********
! GRI−3.0 (1999)
OH+CH3(+M)<=>CH3OH(+M)                       2.790E+18    −1.430      1330.00
! UP TO A FACTOR OF 2 DIFFERENT FROM RECENT THEORY CALCULATIONS OF JASPER ET AL.
! USE 2
     LOW  /   4.000E+36    −5.920    3140.00/
     TROE/    .4120   195.0   5900.00   6394.00/
H2/2.00/ H2O/6.00/ CH4/2.00/ CO/1.50/ CO2/2.00/
H+CH2OH(+M)<=>CH3OH(+M)                      1.055E+12     .500        86.00
! QUITE DIFFERENT FROM RECENT THEORY CALCULATIONS OF JASPER ET AL.
! USE 5
     LOW  /   4.360E+31    −4.650    5080.00/
     TROE/    .600   100.00   90000.0   10000.0 /
H2/2.00/ H2O/6.00/ CH4/2.00/ CO/1.50/ CO2/2.00/
H+CH3O(+M)<=>CH3OH(+M)                       2.430E+12     .515        50.00
! USE 3 TSANG, JPC REF. DATA, 16:471 (1987) − FACTOR GIVEN FOR HIGH
!PRESSURE LIMIT.
     LOW  /   4.660E+41    −7.440    14080.0/
     TROE/    .700   100.00   90000.0  10000.00 /
H2/2.00/ H2O/6.00/ CH4/2.00/ CO/1.50/ CO2/2.00/
! WARNATZ, IN GARDINER, JR. COMBUSTION CHEMISTRY (1984)
! NO UNCERTAINTY GIVEN IN NIST. USE 5
 CH3OH + H = CH2OH + H2             3.200E+13   0.00   6.095E+03
 CH3OH + H = CH3O + H2             8.000E+12   0.00   6.095E+03
! TSANG, JPC REF. DATA, 16:471 (1987)
! 5 TSANG, JPC REF. DATA, 16:471 (1987)
CH3OH + O = CH2OH + OH             3.880E+05   2.50   3.080E+03
! BOTT AND COHEN, IJCK, 23:1075 (1991) {356}
! NO UNCERTAINTY GIVEN IN NIST. USE 5
CH3OH + OH = CH3O + H2O            1.000E+06   2.10   4.967E+02
```

```
CH3OH + OH = CH2OH + H2O              7.100E+06   1.80  −5.960E+02
! TSANG, JPC REF. DATA, 16:471 (1987)
! 10 TSANG, JPC REF. DATA, 16:471 (1987)
CH3OH + O2 = CH2OH + HO2              2.050E+13   0.00   4.490E+04
! TSANG, JPC REF. DATA, 16:471 (1987)
! 10 TSANG, JPC REF. DATA, 16:471 (1987)
CH3OH + HCO = CH2OH + CH2O            9.635E+03   2.90   1.311E+04
! CATHONNET ET AL., J. CHIM. PHYS., 79:475 (1982)
! 10 TSANG, JPC REF. DATA, 16:471 (1987)
 CH3OH + HO2 = CH2OH + H2O2           3.980E+13   0.00   1.940E+04
! TSANG, JPC REF. DATA, 16:471 (1987)
! 3 TSANG, JPC REF. DATA, 16:471 (1987)
CH3OH + CH3 = CH2OH + CH4             3.190E+01   3.17   7.172E+03
! TSANG, JPC REF. DATA, 16:471 (1987)
! 10 TSANG, JPC REF. DATA, 16:471 (1987)
CH3O + CH3OH = CH3OH + CH2OH          3.000E+11   0.00   4.060E+03
!
!********************************************************
! Ethanol sub set
! Ref: Marinov, IJCK 31:183−220 (1999)
!********************************************************
!
C2H5OH(+M)=CH3+CH2OH(+M)                   5.94E+23  −1.68  91163.0   ! Marinov 1998
   LOW /2.88E+85  −18.9  109914./
   TROE/0.5  200.  890.   4600./
   H2O/5./  H2/2.0/  CO2/3.0/  CO/2.0/
C2H5OH(+M)=C2H5+OH(+M)                     1.25E+23  −1.54  96005.0   ! Marinov 1998
   LOW /3.252E+85  −18.81  114930./
   TROE/0.5  300.  900.  5000./
   H2O/5./  H2/2.0/  CO2/3.0/  CO/2.0/
C2H5OH(+M)=C2H4+H2O(+M)                    2.79E+13  0.09   66136.0   ! Marinov 1998
   LOW/2.57E+83  −18.85  86452./
   TROE/0.70  350.  800.  3800./
   H2O/5./
C2H5OH(+M)=CH3HCO+H2(+M)                   7.24E+11  0.095  91007.0   ! Marinov 1998
   LOW /4.46e87  −19.42  115586./
   TROE/0.9  900.  1100.  3500./
   H2O/5./
C2H5OH+OH=C2H4OH+H2O                       1.74E+11   0.27    600.0 ! Marinov 1998
C2H5OH+OH=CH3CHOH+H2O                      4.64E+11   0.15      0.0 ! Marinov 1998
C2H5OH+OH=CH3CH2O+H2O                      7.46E+11   0.30   1634.0 ! Marinov 1998
C2H5OH+H=C2H4OH+H2                         1.23E+7    1.8    5098.0 ! Marinov 1998
C2H5OH+H=CH3CHOH+H2                        2.58E+7    1.65   2827.0 ! Marinov 1998
C2H5OH+H=CH3CH2O+H2                        1.50E+7    1.60   3038.0 ! Marinov 1998
C2H5OH+O=C2H4OH+OH                         9.41E+7    1.70   5459.0 ! Marinov 1998
C2H5OH+O=CH3CHOH+OH                        1.88E+7    1.85   1824.0 ! Marinov 1998
C2H5OH+O=CH3CH2O+OH                        1.58E+7    2.00   4448.0 ! Marinov 1998
C2H5OH+CH3=C2H4OH+CH4                      2.19E+2    3.18   9622.0 ! Marinov 1998
C2H5OH+CH3=CH3CHOH+CH4                     7.28E+2    2.99   7948.0 ! Marinov 1998
C2H5OH+CH3=CH3CH2O+CH4                     1.45E+2    2.99   7649.0 ! Marinov 1998
C2H5OH+HO2=CH3CHOH+H2O2                    8.20E+3    2.55  10750.0 ! Marinov 1998
C2H5OH+HO2=C2H4OH+H2O2                     1.23E+4    2.55  15750.0 ! Marinov 1998
C2H5OH+HO2=CH3CH2O+H2O2                    2.50E+12   0.0   24000.0 ! Marinov 1998
CH3CH2O+M=CH3HCO+H+M                       1.16E+35  −5.89  25274.0 ! Marinov 1998
CH3CH2O+M=CH3+CH2O+M                       1.35E+38  −6.96  23800.0 ! Marinov 1998
CH3CH2O+O2=CH3HCO+HO2                      4.00E+10   0.0    1100.0 ! Hartmann 1990
CH3CH2O+CO=C2H5+CO2                        4.68E+2    3.16   5380.0 ! Marinov 1998
CH3CH2O+H=CH3+CH2OH                        3.00E+13   0.0       0.0 ! Marinov 1998
CH3CH2O+H=C2H4+H2O                         3.00E+13   0.0       0.0 ! Marinov 1998
CH3CH2O+OH=CH3HCO+H2O                      1.00E+13   0.0       0.0 ! Marinov 1998
CH3CHOH+O2=CH3HCO+HO2                      4.82E+14   0.0    5017.0 ! Marinov 1998
DUP
CH3CHOH+O2=CH3HCO+HO2                      8.43E+15  −1.2       0.0 ! Marinov 1998
DUP
CH3CHOH+CH3=CH2CHCH3+H2O                   1.00E+13   0.0       0.0 ! Marinov 1998
CH3CHOH+O=CH3HCO+OH                        1.00E+14   0.0       0.0 ! Marinov 1998
CH3CHOH+H=C2H4+H2O                         3.00E+13   0.0       0.0 ! Marinov 1998
CH3CHOH+H=CH3+CH2OH                        3.00E+13   0.0       0.0 ! Marinov 1998
CH3CHOH+HO2=CH3HCO+OH+OH                   4.00E+13   0.0       0.0 ! Marinov 1998
CH3CHOH+OH=CH3HCO+H2O                      5.00E+12   0.0       0.0 ! Marinov 1998
CH3CHOH+M=CH3HCO+H+M                       1.00E+14   0.0   25000.0 ! Marinov 1998
!
C2H5+HO2=CH3CH2O+OH                        3.00E+13  0.0      0.0   ! Tsang 1986
C2H4+OH=C2H4OH                            1.29E+12  0.0    −817.0   ! Atkinson 1986
C2H4OH+O2=HOC2H4O2                         1.00E+12  0.0   −1100.0  ! Marinov 1998
HOC2H4O2=CH2O+CH2O+OH                      6.00E+10  0.0   24500.0  ! Marinov 1998
!
END
```

Appendix B

Properties of Copper Beryllium

Alloy 3 (C17510)
Technical Datasheet

SMiTHS

High Conductivity Copper Beryllium Alloy

Typical Applications

Thermal management, metal and plastic moulding, welding, automotive, marine, chemical processing

Product Description

Alloy 3 is a high conductivity copper beryllium alloy used in applications requiring a combination of high thermal conductivity with moderate strength. Alloy 3, supplied with certified mechanical properties, is fully heat treated and no additional treatment is required. Alloy 3 is nonmagnetic and provides excellent resistance to thermal fatigue.

Corrosion Resistance

Alloy 3's corrosion resistance is similar to pure copper. It resists corrosion in sea water, most organic solutions, non-oxidizing acids, and dilute alkalis. Alloy 3 is not subject to hydrogen embrittlement, and it resists stress corrosion cracking in sulfide and chloride solutions. Alloy 3 is not recommended for use with ammonium hydroxide or strongly oxidizing acids.

Material Specifications

- UNS C17510
- ASTM B441
- RWMA – Class 3
- BS EN 12163

Fabrication

- Machining – very good
- Brazing – good
- Electro-discharge machining – good
- Welding – fair

Availability

Bar, rod, plate, wire, tube, extrusions, forgings

Chemical Composition (weight %)

Weight (%)	Be	Ni	Fe	Cu
Min	0.2	1.4		
Max	0.6	2.2	0.1	Balance

High Temperature Strength

Temperature, °C	200	300	400	450	500
UTS, MPa	760	760	730	680	520

Mechanical Properties

	Alloy 3 AT	Alloy 3 HT
UTS, MPa	680-900	750-970
0.2% PS, MPa	550-690	650-870
Elongation, % in 4D	10-25	5-25
Hardness, HRB	92-100	95-102
Fatigue strength at 10^8 , MPa	240-350	240-350
Elastic modulus, GPa	138	138
Thermal conductivity, W/m ºC	240	240
Electrical conductivity, MS/m	32	32
Thermal expansion, ppm/ºC	18	18
Magnetic permeability	1.000	1.000
Density, g/cm³	8.83	8.83

www.smithmetal.com

Appendix C

Published and submitted journals

Published journal

1. Palakunnummal, M. F., Sahu, P., Ellis, M., and Nazha, M. (July 31, 2020). "Simulation-Aided Development of Prechamber Ignition System for a Lean-Burn Gasoline Direct Injection Motor-Sport Engine." ASME. J. Eng. Gas Turbines Power. August 2020; 142(8): 085001. https://doi.org/10.1115/1.4047767

Accepted for publication with revision

1. M. Fayaz, P. Sahu, M. Ellis and M. Nazha, "A cylinder pressure-based knock detection method for pre-chamber ignition gasoline engine.", SAE Journal of Engines.